MULTISCALE COMPUTATIONAL MODELING OF MULTIPHASE COMPOSITES WITH DAMAGE

A Dissertation

by

FEIFEI CHENG

Submitted to the Office of Graduate and Professional Studies of
Texas A&M University
in partial fulfillment of the requirements for the degree of

DOCTOR OF PHILOSOPHY

Chair of Committee,	J.N. Reddy
Committee Members,	Ibrahim Karaman
	Harry Hogan
	Xin-Lin Gao
Head of Department,	Andreas A. Polycarpou

December 2013

Major Subject: Mechanical Engineering

ABSTRACT

A multiscale computational framework for multiphase composites considering damage is developed in this research.

In micro-scale, micromechanics based homogenization methods are used to estimate effective elastic moduli of graded Ti_2AlC/Al composites (GCMeCs) considering existence of damage (micro-voids). Then, in macro-scale, these properties are implemented in finite element model by using user material subroutine (UMAT) in Abaqus for numerical analysis of plate.

In meso-scale, detailed 3D RVEs are created based on the microstructure of composites. Effective thermal and elastic properties are obtained from the corresponding FE models of 3D RVEs and compared with experimental results and micromechanics based homogenization methods. Two constitutive models are used to model plastic-damage behavior of two IPCs regarding their different material properties of constituent phases: (1) Due to the ductile properties of constituent phases for stainless-steel/bronze IPCs, a widely used porous plasticity constitutive model, Gurson-Tvergaard-Needleman (GTN) model, is adopted to investigate elastoplastic-damage behavior of stainless-steel/bronze IPCs. (2) For porous Ti_2AlC, a continuum damage mechanics (CDM) based plastic-damage coupled constitutive model is used to study damage evolution in porous Ti_2AlC, which can take distinct tensile and compressive inelastic behaviors of Ti_2AlC into consideration. From the simulation results of FE models of 3D RVEs, it is found that:

- Porosity and interfacial layer with low effective thermal conductivity lowers the overall heat flux flowing through NiTi/Ti_3SiC_2 IPC.
- The existence of thermal residual stress within stainless-steel/bronze IPCs leads to plastic deformation, especially in bronze phase, which further results in reduction of apparent moduli subjected to uniaxial tension. Nucleation of the new voids, which occurs at the second-phase particles by decohesion of the particle-matrix interface, has the main contribution to the overall damage.
- For porous Ti_2AlC with aligned ellipsoid-like pores, tensile stress plays a very important role in local damage of porous Ti_2AlC due to the relatively low tensile strength and brittle-like tensile behavior of dense Ti_2AlC. Different than typical porous ceramic, porous Ti_2AlC fails in a quasi-brittle manner even with 30-40 vol. % porosity. The transversely isotropic material system has higher compressive strength in transverse direction than that in longitudinal direction.

DEDICATION

To

My dear grandparents, Huifen Wang, and Fureng Cheng

My beloved husband, Sen Yang

ACKNOWLEDGEMENTS

First, I would like to thank my advisor and committee chair, Professor J.N. Reddy, for his support, guidance and encouragement through my MS and PhD program at Texas A&M University. I admire his passion and dedication to research and teaching, and I sincerely thank him for being the mentor of my lifetime.

Special appreciation is extended to my committee members, Professor Ozden Ochoa, Professor Ibrahim Karaman, Professor Harry Hogan, and Professor Xin-Lin Gao, for their valuable comments and suggestions on this dissertation and their support throughout the course of this research.

I also would like to thank Professor Rashid K. Abu Al-Rub and Dr. Sun-Myung Kim for their generous help started from Continuum Damage Mechanics class, which later leaded to a fruitful collaboration.

Additionally, thanks to my grandparents for their unconditional love and continuous support and to my husband, Sen Yang, your love is the place I find warmth, happiness and strength.

Finally, I would like to gratefully acknowledge the financial support from the Air Force Office of Scientific Research (AFOSR), MURI Program (FA-9550-09-1-0686) for the research reported in this dissertation.

TABLE OF CONTENTS

Page

CHAPTER Page

LIST OF FIGURES

Page

Page

Page

Page

Page

LIST OF TABLES

Page

CHAPTER I

INTRODUCTION AND LITERATURE REVIEW

1.1 Background

Graded Ceramic/Metal Composite (GCMeC) is an innovative design integrating functionally graded ceramics (MAX phases) and metal in one material system, which is used to develop weight efficient aerospace structures for extreme environments with increased strength and durability. MAX phase is a family of ceramics consisting of more than 70 ternary carbides and nitrides (M is an early transition metal; A is an A-group element; and X stands for C and/or N) [1, 2]. The reason to select MAX phases as composed phase of GCMeC, e.g. Ti_2AlC, Ti_3SiC_2, is that they have an unusual combination of both ceramic and metal properties: On one hand, like ceramics they have high temperature and oxidation-resistance [3], high stiffness [4], and low coefficient of thermal expansion [2]. On the other hand, due to their layered atomic nature, the presence of active slip systems, and the formation of heavily deformed lamellar bridges upon damage, MAX phases are relatively soft, readily machinable, thermal shock resistant and damage tolerant [1, 2] like metal. Moreover, they can dissipate mechanical energy during compressive cyclic loading at room temperature and have better creep resistance than most of the high-temperature metallic alloys [5].

Due to the common existence of defects (micro voids, cracks, and debonding) in GCMeCs which results from manufacturing process (e.g., bubbles in melting, incomplete infiltration etc.), and complex inelastic behavior (e.g., plastic-damage

behavior) of GCMeCs, a multiscale computational framework is needed to understand and predict the thermomechanical behavior of GCMeC material system with damage. The damage referred here includes all types of damages, including micro-scale defects and macro-scale damages, such as voids and cracks that formed under certain load condition.

In micro-scale, micromechanics based homogenization methods can be used to obtain basic mechanical properties of multiphase composites considering defects, such as elastic moduli and coefficient of thermal expansion (CTE). However, the geometry representation of these methods is highly simplified and cannot efficiently reflect the microstructure of the given composite material systems. Therefore in meso-scale, representative volume element (RVE) method is adopted to create detailed model for multiphase composites based on their microstructures, especially for the interpenetrating phase composite (IPC) case when each constituent phase is interconnected in 3D space. In macro-scale, with the graded compositions of the constituent phases, GCMeC can be seen as functionally graded material (FGM). Furthermore, the mechanical properties obtained from micro- and meso-scale micromechanics based homogenization methods and RVE method can be implemented in macro-scale finite element model for structural analysis. A short introduction on functionally graded materials (FGMs) and interpenetrating phase composites (IPCs) is given below:

Functionally graded materials (FGMs) were first developed in the mid-80s, and were used in thermal protection components in the aerospace and other industrial applications[6]. Unlike traditional laminate composites or composites with uniformly

distributed reinforcement phase(s), functionally graded materials are a new kind of engineered materials which has non-uniform distribution of reinforcement phase(s) varied in one or more directions spatially in microscopic scale. By using different sizes and shapes of the reinforcement phase(s), adjusting the gradient variation, and interchanging the characters of reinforcement and matrix phases, functionally graded materials could have continuous varied thermal and mechanical properties in macroscopic scale. This new concept in material science and mechanics of materials allows one to integrate the advances of different materials as well as structural consideration in a system design. Functionally graded materials have been widely used in aerospace and industrial applications which usually involving extreme work conditions. The concept of tailoring microstructural transition of different phases to optimize the temperature, deformation and stress distributions has also been used to enhance thermal fatigue resistance and life of ceramic thermal barrier coatings. Other benefits can be realized from the use of functionally graded architectures include fracture toughness enhancement in ceramic matrix composites through tailored interfaces and mismatch reduction in laminate composites by smoothing out the gradient transition among dissimilar layers. More other applications of functionally graded materials mentioned in [6] include solar energy conversion devices, dental implants and naturally occurring biological FGMs.

Interpenetrating phase composites (IPCs) which are multi-phase composites with co-continuous phase structures can be seen as a part of the skeletal transition zone in the functionally graded materials. In two-phase IPCs, each constituent phase completely

interpenetrates through the composite microstructure in all three dimensions and contributes its own properties in a very independent manner to the overall properties of the composite, while the two phases are topologically interconnected and mutually reinforced in the three dimensions. IPCs have been experimentally shown to enhance elastic properties, as compared with discontinuously reinforced phase structures [7-9]. Different than the traditional composite material that usually have a continuous phase(matrix) with one or more discrete reinforcement phases, such as fibers, whiskers or particles, the continuity of each phase kept in the IPCs make them a truly multifunctional and highly durable material. Examples of the processing techniques used to produce IPCs include directed metal oxidation, spontaneous infiltration, squeeze casting, gas pressure assisted infiltration, self-propagating high-temperature synthesis (SHS), three-dimensional printing process and spark plasma sintering (SPS) [10-22]. Another material system studied here, porous MAX phase, can also be seen as IPC if porosity is treated as a constituent phase. It has drawn author's attention due to their light weight, open-cell foam structure and application as preforms of multi-phase IPC using infiltration fabrication technique [23]. Therefore in this dissertation, regarding scale and geometry, the thermomechanical behavior of following four composite material systems has been studied:

- GCMeCs (macro-scale): Functionally graded Ti_2AlC/Al rectangular plate.
- IPCs (meso-scale): NiTi/Ti_3SiC_2 IPC, stainless-steel/bronze IPCs and porous Ti_2AlC.

Literatures on these topics of interest in this dissertation are reviewed and summarized below.

1.2 Literature review

1.2.1 Micromechanics based homogenization methods

Functionally graded material (FGM) can be treated as a material system microscopically contains a particle–matrix zone with dispersed particles filled in a continuous matrix, followed by a skeletal transition zone, then by another particle–matrix zone with interchanged phases of particle and matrix [24]. As mentioned before, the skeletal transition zone is also can be seen as interpenetrating phase composites (IPCs), which will be discussed later.

Efforts at predicting the effective elastic moduli over the entire composition range for FGMs had limited success. The micromechanics based homogenization methods that have been used to estimate the elastic moduli of such composites can be grouped into two categories. In the first category, the composite structure is not treated as being fixed: Hashin and Shtrikman (H-S bounds) [25] considered a random discontinuous sphere inclusion assembly, Torquato et al. [26] used the effective medium approximation (EMA), researchers [27, 28] considered a random contacting elliptical inclusion assembly, and the contiguity approach used by Fan et al.[29] considers a random distribution of discontinuous inclusions. In the second category, the composite structure is fixed and is usually modeled by a repeating geometry: the rule-of-mixture iso-stress and iso-strain approximations consider an alternating layer of each phase assembly [30], Ravichandran [31] and Paul [32] considered a discontinuous unit-cell assembly, while Tuchinskii considers a co-continuous unit-cell assembly [33].

Comparing to the models of predicting effective elastic constant of composites, models for predicting the coefficient of thermal expansion (CTE) are limited. The simplest model to estimate the CTE of two-phase materials is the rule of mixtures (ROM). Kerner [34] and Schapery [35] proposed models for particle-reinforced composites. Also the H-S bounds for elastic constants were used in the equations for coefficient of thermal expansion, then the bounds for CTE are established in [36]. For finite element model considering micro damage, Bruck [37] modified ROM model and Schapery model to obtain the effective CTE of the damaged particle-reinforced composites.

Micromechanics methods have also been used to analyze linear thermoelastic responses of functionally graded materials. Aboudi et al. [6, 38] and Pindera et al. [39] presented higher order micromechanical models for analyzing steady linear heat conduction and thermo-elastic deformations of functionally graded materials. Higher order functions of the field quantities were defined for each constituent. Closed form solutions of stress and deformation fields in the functionally graded beams and plates obtained from the higher order theory were comparable to the ones calculated using finite element method. Mori-Tanaka method and self-consistent micromechanical models have been used to analyze thermoelastic responses of FGMs, e.g., Reiter et al. [40], Reddy and Cheng [41], and Vel and Batra [42]. Gasik [43] derived a micromechanical model for analyzing FGMs with arbitrary distributions of the constituents. The FGMs microstructures were idealized by piecewise homogeneous materials (sub cells) having cubic inclusions. Each sub cell corresponded to fixed

volume content. The calculated effective elastic constant and coefficient of thermal expansion were compared with the ones obtained using Mori–Tanaka, Voigt, and Kerner's models. Ueda and Gasik [44] and Ueda [45] have extended the Gasik [43] micro model to analyze transient heat conduction and thermal stresses in FGMs having elastic and inelastic constituents. Parametric studies on the effects of material gradations on the overall stress and deformation fields were performed. In [24, 46], Yin et al. formulated effective linear coefficient of thermal expansion and effective elastic material constants, i.e., Young's moduli and Poisson's ratio, of FGMs using micromechanical models. The particle interactions were considered in obtaining the effective material properties. The properties of the constituents were assumed independent on temperature fields (linear behaviors). The calculated effective material properties were verified with experimental data. It was shown that particle interactions needed to be considered when the volume contents of the particles were relatively high.

1.2.2 Thermal conductivity of IPC

Micromechanics methods have been used to predict the effective thermal properties of composites [47]. For example, Benveniste and Miloh [48] predicted the effective conductivity of a composite media where temperature discontinuity at constituent interfaces reveals thermal boundary resistance. Böhm and Nogales [49] used a Mori-Tanaka scheme to predict the effective thermal conductivity of spherical particle reinforced composites with interfacial resistance and prescribed particle size distributions. Dunn and Taya [50] developed an analytical model to study the effective

thermal conductivity of multiphase composites reinforced with coated fillers considering the influence of thermal resistance at the filler-matrix interface. All the studies mentioned are based on composites with one phase as matrix and a secondary phase as reinforcement. The NiTi/Ti_3SiC_2 composite, however, is an interpenetrating phase composite (IPC), and the presence of pores and reaction interfaces in this composite makes it an even more complicated, four-component (i.e. Ti_3SiC_2, NiTi, pore, and interface) system. No computational work has been done on the effective thermal conductivity of IPC with such a complex microstructural characteristics.

1.2.3 Mechanical response of IPC

A large amount of work has been done on characterization and modeling of IPCs focusing on elastic effective properties of the composites. Poniznik in [51] gave a review on estimating effective elastic properties of IPCs. For analytical approximation, an approach based on Voigt and Reuss models were developed by Tuchinskii [33], Zahl *et al.* [52], Ravichandran [53, 54], and Feng *et al.* [55], among others. Tuchinskii [33] proposed a unit cell method designed to calculate bounds for effective elastic constants of a bimetallic composite. The unit cell was considered with an interpenetrating phase in the shapes of a 3D cross section. According to different ways of dividing the unit cell into sub-layers, different results were obtained based on the iso-stress and iso-strain assumptions that lead to bounds for effective elastic properties. Later in Ravichandran's study [53, 54], simplified unit-cell models of the microstructure was used to predict the deformation and creep behavior of interpenetrating phase composites. Simple iso-stress

and iso-strain models of deformation of bimaterials have been employed for this purpose. Feng [55] developed a model for calculating the effective elastic properties of anisotropic multiphase composites, containing both interpenetrating phases and disconnected inclusions using the Mori-Tanaka method, the iso-stress, and iso-strain assumptions. Another approach is presented in the work of Schmauder *et al.* [56] and Torquto [57], where the influence of microstructure of the phases on the effective elastic properties of composites was addressed.

Following these analytical approximations, numerical methods, such as the finite element method, were used for calculation of effective elastic macroscopic properties from microstructural data. Feng *et al.* [55] simulated the elastic behavior of a co-continuous stainless-steel/bronze composite. Mishnaevsky [58] represented the irregular microstructure of a composite by a number of prescribed or randomly generated square (2D) and cubic (3D) cells. Poniznik [51] used the randomly generated voxels structure FE model to simulate a real Al_2O_3-Cu microstructure, which is acquired from the computer tomography images, compared the results with analytical models such as the unit cell method, Tuchinskii bounds and Hashin-Shtrikman bounds [25].

Inelastic behavior of IPCs, such as plastic or viscoplastic behavior has also been studied by some researchers. Feng *et al.* [59] extended their model to characterize the elastoplastic behavior of co-continuous stainless-steel/bronze composites, then compared the analytical model with the FE analysis results. In Kouzeli and Dunand's work [7], a self-consistent approach was used to model the composites consisting of a thermo-elastoplastic aluminum matrix with 34 and 37 vol.% sub-micron Al_2O_3 particles in

compression for two reinforcement architectures: interconnected and discontinuous. The classical self-consistent and the three-phase self-consistent models were used for the interconnected and discontinuous architectures, respectively. They found that at small strains the interconnected reinforcement becomes increasingly more effective at strengthening the composites at elevated temperatures.

1.2.4 Porous plasticity

The above studies on effective elastic and inelastic properties of IPCs were conducted mainly based on changing the material constants and volume fraction of each phase. However, other factors like geometrical topology of the phases, thermal residual stress due to processing, and damage such as debonding at interface of phases, micro-voids and micro-cracks may also affect the effective properties of the composites. For example, Wegner and Gibson [21] conducted experimental and modeling investigations on the mechanical and thermal expansion properties of stainless-steel/bronze composites, and they found from the results of nonlinear FE analyses that the existence of thermal residual stress and porosity contribute to a reduction in effective elastic moduli of these composites. However, the damage effect was ignored in the FE analysis even though the composites failed at very small strains compared to their constituent materials. Therefore, it is also very important to understand the link between damage and the mechanical properties of IPCs, which requests an understanding on the damage mechanisms, how the damage influence the effective properties, as well as how damage couples with other mechanical behavior.

One of the most widely used plasticity-damage models to describe ductile rupture of composite materials is the Gurson-Tvergaard-Needleman model, which was first developed by Gurson [60] for a problem with spherical void growing in a rigid-perfectly plastic matrix and later modified by Tvergaard and Needleman [61, 62] to completely model void growth, nucleation and coalescence in ductile rupture process of porous materials. For better ductile fracture models dealing with various material systems, there have been some extensions to Gurson model. For example, Nahshon and Hutchinson in [63] modified Gurson-Tvergaard-Needleman model to account for shear-dominated fracture with low triaxiality. The issues with void coalescent in failure criterion were improved by some researchers in [64-69]. More accurate hardening descriptions of matrix material were proposed in [70, 71] considering kinematic hardening, and in [72] with improved strain hardening exponents. Extended Gurson-type rate-dependent porous plastic models were developed in [73-76]. For the effects of void shape and size, the work in [77-79] extended Gurson-type model to account for ellipsoidal void shape, referring as Gologanu–Leblond–Devaux model, and later in [64, 67, 80-84] plastic anisotropy resulting from non-spherical void shape, aspect ratio and orientation were studied. The effect of void size was studied in [85, 86].

As a result, Gurson-type of models were widely used in modeling ductile rupture of various material systems: examples like metallic alloys [73, 75, 76, 86-94], polymers [95-97] and Particle reinforced Metal Matrix composites [98, 99].

1.2.5 Continuum damage mechanics based plasticity-damage model

Recently, porous MAX phases have been studied due to their light weight, open-cell foam structure, tailorable thermo-mechanical properties [100-103], and application as preforms of multi-phase composites [23]. All of these studies focused on design, manufacture and properties of the porous MAX phases. Systematic numerical study of porous MAX phases is needed to optimize the microstructure since the porous microstructure leads to stress and strain concentration near pores which will result in strength and damage tolerance reduction.

The crystalline defects in Ti_2AlC are basal plane dislocations, which are large in amount, multiply and are mobile even low temperature (as low as 77K). Therefore, the ductility of Ti_2AlC is in between of typical ceramic and metal. The formation of kink bands (KB) under compressive loading plays a central role in deformation of Ti_2AlC, which also results in the distinct tensile and compressive behaviors (i.e. Ti_2AlC is more brittle in tension than in compression at room temperature) [104]. Therefore, a plastic-damage constitutive module that can capture the distinct tensile and compressive behavior of a quasi-brittle material system should be used.

Coupled plasticity and damage constitutive models are usually combinations of isotropic hardening and either isotropic or anisotropic damage. Cicekli et al. in [105] gave a review of these constitutive models. In general, they can be divided into two categories: One category, the stress-based plasticity is formulated in the effective (undamaged) configuration, e.g. [106-109]. The second category, the stress-based plasticity is formulated in the nominal (damaged) configuration and the nominal stress is

defined as the macro-scale stress work on both effective and nominal configuration, e.g. [110-115].

In this study, a coupled plasticity-damage constitutive model belongs to the first category mentioned above which was formulated by Cicekli et al. [105] and modified by Abu Al-Rub and Kim [116] is used. In this constitutive model, the Lubliner yield criterion [114] expressed in the effective (undamaged) configuration is adopted to predict the plastic behavior of porous Ti_2AlC. Furthermore, the non-associative plasticity flow rule based on the Drucker–Prager potential and power law damage evolution functions with two distinct damage evolution surfaces: tensile and compressive damage surfaces are included in this constitutive model.

1.3 Research objectives

The main objective of this dissertation is to estimate effective thermomechanical properties and investigate the plastic-damage behavior of multi-phase composite material systems with damage. This contains twofold steps: one is to understand the influence of damage on the strength of composite materials, and the other one is to develop a framework for interpreting measurements of damage evolution. Therefore, in details the objectives are:

- **Objective I: Estimation of effective elastic moduli of multiphase composites using micromechanics based homogenization methods.**

Micromechanics based homogenization methods, such as Mori-Tanaka method, unit cell method, and Hashin-Shtrikman bounds etc., are used to estimate the effective elastic moduli of multiphase composites with various phase compositions.

- **Objective II: Development of 3D RVEs based on microstructures of the multiphase composites.**

  To make up for the deficiencies of homogenization methods for their highly simplified geometry and certain assumptions made in derivation (such as dilute assumption for Mori-Tanaka method), detailed 3D RVEs are developed based on the microstructures of the given multiphase composites.

- **Objective III: Estimation of effective thermomechanical properties of multiphase composites using 3D RVE s and FE method.**

  To validate the 3D RVEs created, effective thermomechanical properties of composite material systems are obtained from the corresponding 3D RVEs using finite element method and compared with those obtained micromechanics based homogenization methods and experimental results.

- **Objective IV: Modeling of plastic-damage behavior of composite material systems using 3D RVEs and proper constitutive models.**

  A porous plasticity constitutive model for ductile rupture of stainless-steel/bronze IPCs and a plastic-damage constitutive model for porous Ti_2AlC accounting for different tensile and compressive behaviors of dense Ti_2AlC are used in this study to investigate the plastic-damage behaviors for the corresponding material systems.

1.4 Outline of the dissertation

The dissertation consists of 6 Chapters and is organized as follows:

- **Chapter I** presents the background and objectives of this research and a detailed literature review on the topics of interests is given.
- **Chapter II** estimates the effective elastic moduli of two-phase functionally graded material with pre-existing damage using micromechanics based methods. Then these properties are implemented in finite element model to study the mechanical response of a graded Ti_2AlC/Al rectangular plate.
- **Chapter III** develops 3D RVEs of stainless-steel/bronze interpenetrating phase composites based on their microstructure, predicts the effective elastic and elastoplastic properties of the undamaged given IPCs. Then these effective properties are used in Gurson-Tvergaard-Needleman (GTN) constitutive model to study the elastoplastic behavior and damage evolution of the IPCs considering micro-damage, such as micro-voids and debonding at the interface of phases.
- **Chapter IV** creates 3D RVEs of NiTi/Ti_3SiC_2 composite consists of four phases and estimates the effective temperature-dependent thermal conductivity of the composite considering the effects of existence of porosity within Ti_3SiC_2 phase and interfacial layer forming between Ti_3SiC_2 phase and NiTi phase.
- **Chapter V** builds two groups of 3D RVEs of porous Ti_2AlC regarding the shape of pores and investigates the effects of porosity volume fraction, pore size and shape on overall elastic, plastic-damage behavior of porous Ti_2AlC. A coupled plasticity-damage constitutive model developed by Cicekli et al.[105] and modified by Abu

Al-Rub and Kim [116] is adopted to simulate the plastic-damage behavior of porous Ti_2AlC.

- **Chapter VI** summarizes the research works in this dissertation and draws some conclusions from the numerical results.

CHAPTER II

MECHANICAL RESPONSE OF FUNCTIONALLY GRADED RECTANGULAR PLATE WITH PRE EXISTING MICRO-DAMAGE

2.1 Estimation of effective mechanical properties

A micromechanics based unit cell method [59] is used in obtaining the effective elastic moduli along the graded direction for isotropic case. The unit cell geometry in this method [59] for a macroscopically isotropic, two-phase interpenetrating phase composite is shown in Figure 1.

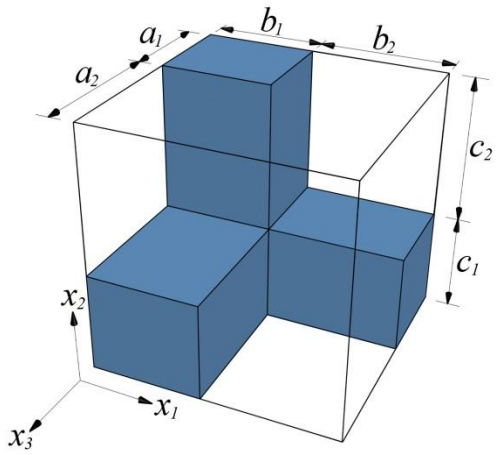

Figure 1: Unit cell method for two-phase interpenetrating phase composites.

The effective elastic constants are obtained by decomposing the unit cell into parallel and series sub-cells based on a combination of iso-stress and iso-strain

assumptions. For an isotropic composite it is assumed that all directions of decomposition are equal and after averaging over the whole composite volume the differences between the results of decomposition in different directions will vanish. Assuming in Figure 1 a_1=b_1=c_1, and define a non-dimensional quantity $a = a_1/(a_1 + a_2)$, then the effective Young's modulus of the two-phase IPC can be expressed as [59]:

$$E_c = a^2 E_r + (1-a)^2 E_m + \frac{2a(1-a)E_m E_r}{aE_m + (1-a)E_r} \tag{2.1}$$

where the subscripts "*r*" and "*m*" refer to the reinforcement extending in three dimensions and the matrix, respectively. The same model is used for computing the effective shear modulus,

$$G_c = a^2 G_r + (1-a)^2 G_m + \frac{2a(1-a)G_m G_r}{aG_m + (1-a)G_r} \tag{2.2}$$

Similarly, for a three-phase interpenetrating phase composite, define another non-dimensional quantity $b = a_1' \Big/ \left(a_1' + a_2'\right)$ with $a_1' = b_1' = c_1'$ for the third phase, the effective Young's modulus and shear modulus can be written as:

$$\begin{aligned} E_c = {} & a^2 E_1 + b^2 E_2 + (1-a-b)^2 E_m + \frac{2a(1-a-b)E_m E_1}{aE_m + (1-a)E_1} + \\ & \frac{2b(1-a-b)E_m E_2}{bE_m + (1-b)E_2} + \frac{2abE_1 E_2 E_m}{aE_m E_2 + bE_m E_1 + (1-a-b)E_1 E_2} \end{aligned} \tag{2.3}$$

$$\begin{aligned} G_c = {} & a^2 G_1 + b^2 G_2 + (1-a-b)^2 G_m + \frac{2a(1-a-b)G_m G_1}{aG_m + (1-a)G_1} + \\ & \frac{2b(1-a-b)G_m G_2}{bG_m + (1-b)G_2} + \frac{2abG_1 G_2 G_m}{aG_m G_2 + bG_m G_1 + (1-a-b)G_1 G_2} \end{aligned} \tag{2.4}$$

where the subscripts "1" and "2" refer to the two reinforcement phases extending in three dimensions.

As an example, the effective elastic moduli of Ti_2AlC/Al composite with varied volume fraction of Ti_2AlC are plotted in Figure 2. The material properties of the two constituent phases are listed in Table 1.

Table 1: Material constants of constituent phases for Ti_2AlC/Al composite.

Material	Young's modulus E (GPa)	Poisson's ratio ν
Al	70	0.346
Ti_2AlC	278	0.17

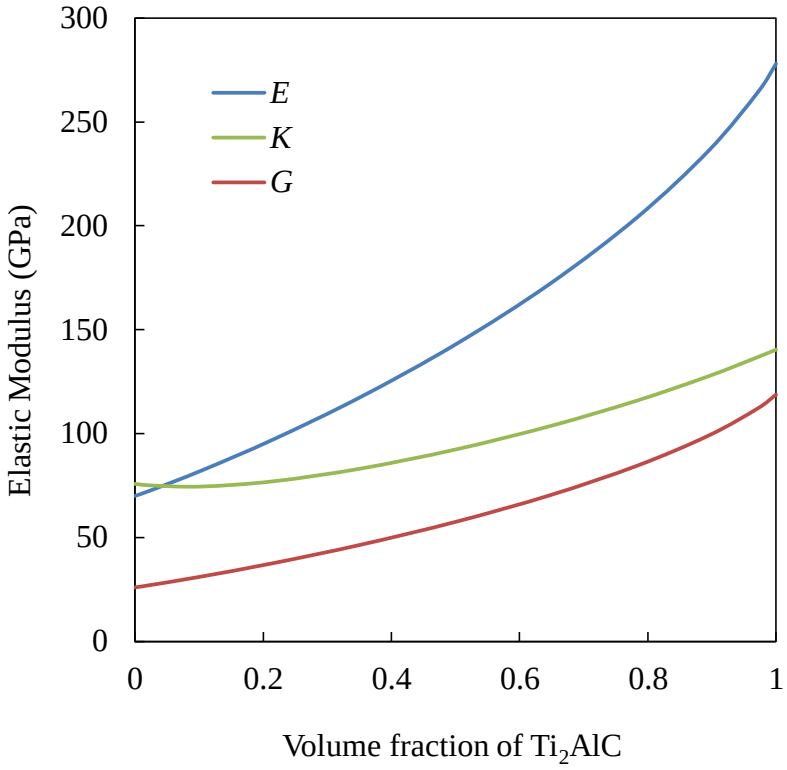

Figure 2: Effective elastic moduli of Ti_2AlC/Al composite with varied volume fraction of Ti_2AlC obtained from unit cell method.

Comparisons of effective Young's modulus as a function of volume fraction of Ti_2AlC calculated using the Voigt, Reuss, Mori-Tanaka methods and unit cell method for Ti_2AlC/Al composites are plotted in Figure 3. It can be seen that there is only one curve for unit cell method which lies between two curves for the Mori-Tanaka method. This is because the shape of the blue part and shape of the transparent part in the cube shown in Figure 1 are similar, and therefore the formulations of E_c and G_c are symmetric regarding the two phases in Eq. (2.1) and Eq. (2.2). In other words, not like other classic

micromechanics based homogenization methods, the results will be the same for treating either one of the two phases as reinforcement for unit cell method.

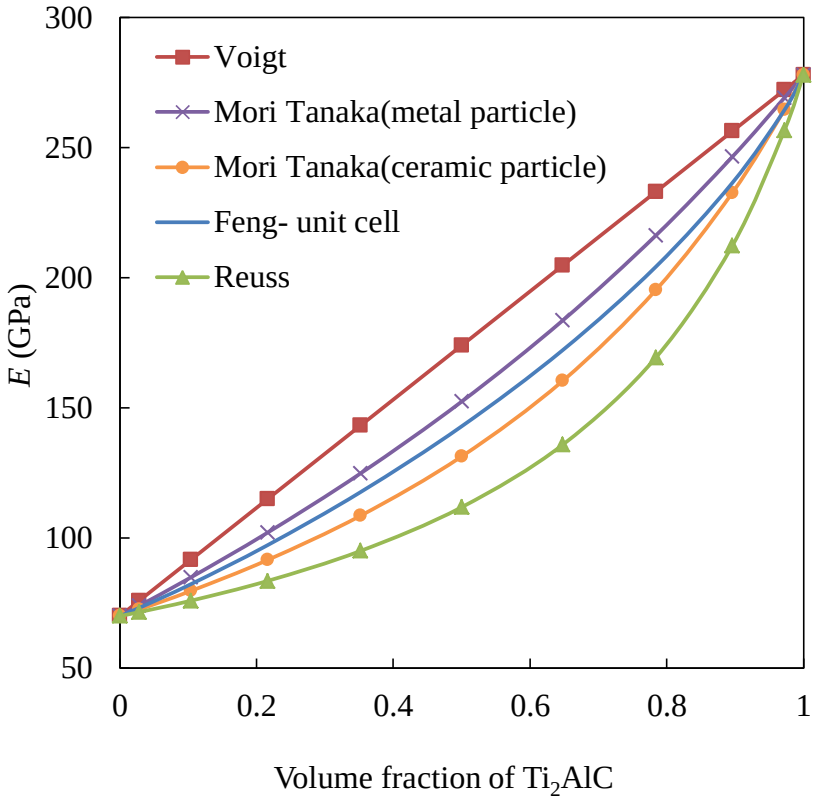

Figure 3: Effective Young's moduli vs. volume fraction of Ti_2AlC for Ti_2AlC/Al composites.

Unit cell method also has the capability of including inclusion type of phases by utilizing the Mori-Tanaka method with iso-stress, iso-strain assumptions. Here we represent the two-phase interpenetrating phase composites with micro-damage by

considering the above two-phase model as a hybrid matrix (or averaged media), and introduce the micro damage (micro voids and micro cracks) into the model by using spherical voids as the third phase. The latter are randomly distributed in interpenetrating two-phase hybrid matrix.

For voids, consider the limiting case of $G_1 / G_0 \to 0, K_1 / K_0 \to 0$, where "1" refer to voids, and "0" refer to two-phase hybrid matrix, then the Mori-Tanaka method [117] reduces to

$$K = K_0 - \frac{f_d K_0 \left(3K_0 + 4G_0\right)}{3K_0 + 4G_0 - 3\left(1 - f_d\right) K_0} \tag{2.5}$$

$$G = G_0 - \frac{5 f_d G_0 \left(3K_0 + 4G_0\right)}{5\left(3K_0 + 4G_0\right) - 6\left(1 - f_d\right)\left(K_0 + 2G_0\right)} \tag{2.6}$$

where f_d is the volume fraction of voids, K_0 and G_0 are the bulk and shear modulus of hybrid matrix which can be obtained from unit cell method of interpenetrating two-phase composites from Eq. (2.1) and Eq. (2.2).

Figure 4 includes the plots of effective Young's modulus as a function of void volume fraction for different compositions of two phases within the hybrid matrix. The letter "r" here refers the volume fraction of Al among the total volume fraction of Ti_2AlC/Al hybrid matrix. Using this method, the effective elastic moduli of GCMeC with micro-voids can be obtained and further used in structural level analysis, such as mechanical response to bending for plate.

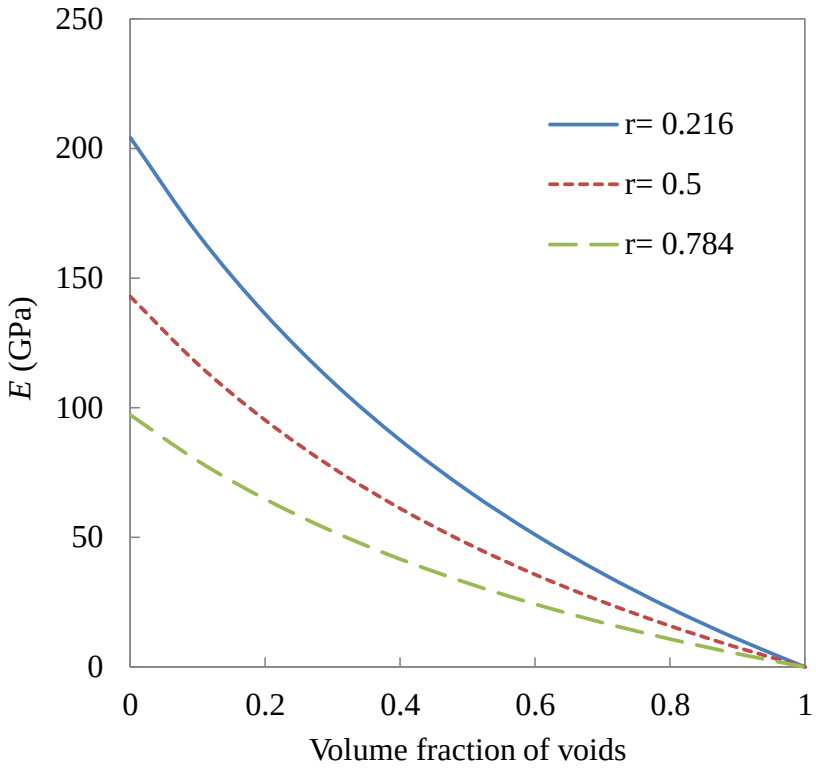

Figure 4: Effective Young's modulus vs. volume fraction of voids.

2.2 Finite element modeling of graded Ti_2AlC/Al rectangular plate

Commercial package Abaqus is used for finite element modeling and analysis. User material subroutine UMAT corresponding to aforementioned unit cell method is developed and implemented in nonlinear finite element analysis of 3D GCMeC rectangular plate.

As a numerical example, a rectangular GCMeC plate made of Al and Ti_2AlC is studied. The material properties for the two constituent phases are listed in Table 1. The dimension ratios of the plate are a/b =1 and a/h =10. Here in this section, "a" and "b" refer as in-plane edge lengths and h is the thickness. Simply supported boundary

conditions in Eq. (2.7) are applied. Uniformly distributed load of intensity q_0 is applied on the pure Ti_2AlC surface ($z = h/2$).

$$\text{Simply Support BCs}: \begin{cases} v = w = 0, & \text{at } x = 0, a \\ u = w = 0, & \text{at } y = 0, a \end{cases} \tag{2.7}$$

The geometry of graded Ti_2AlC/Al plate and corresponding mesh are shown in the Figure 5. There are 16000 elements in the mesh, and C3D20R element (20-node quadratic brick, reduced integration element) is used as element type. Also, geometry nonlinearity is taken into account in the finite element analyses.

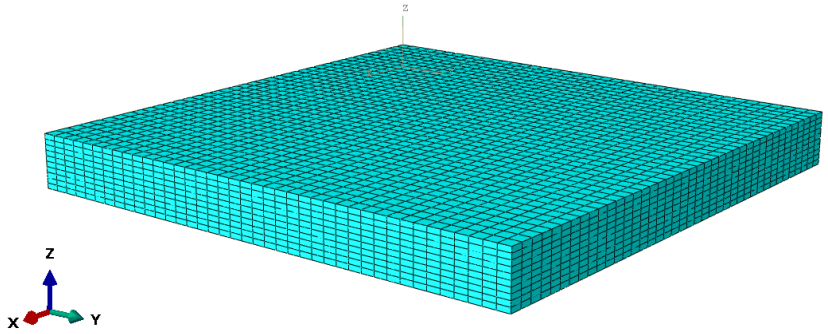

Figure 5: Finite element mesh of 3D graded Ti_2AlC/Al plate generated in Abaqus.

A linear through-thickness variation of the volume fractions of the two constituent phases is assumed here, i.e.

$$f_{ceramic}=\left(\frac{z}{h}+\frac{1}{2}\right)^{n},\ f_{metal}=1-\left(\frac{z}{h}+\frac{1}{2}\right)^{n},$$
$$\text{when } n=1 \Rightarrow f_{ceramic}=\frac{z}{h}+\frac{1}{2} \tag{2.8}$$

By using unit cell method aforementioned, effective material properties for whole composition range of the two phases along thickness direction of the graded Ti_2AlC/Al plate can be obtained. Figure 6 to Figure 8 show the comparisons of the effective elastic properties along plate thickness direction for various void volume fractions obtained from unit cell method.

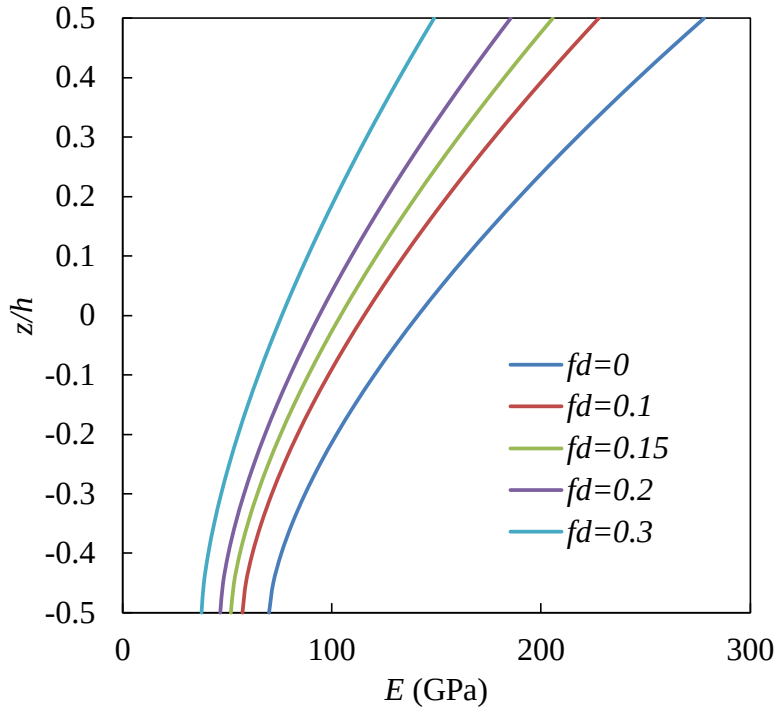

Figure 6: Effective Young's modulus along thickness direction of graded Ti_2AlC/Al plate for various void volume fractions obtain from unit cell method.

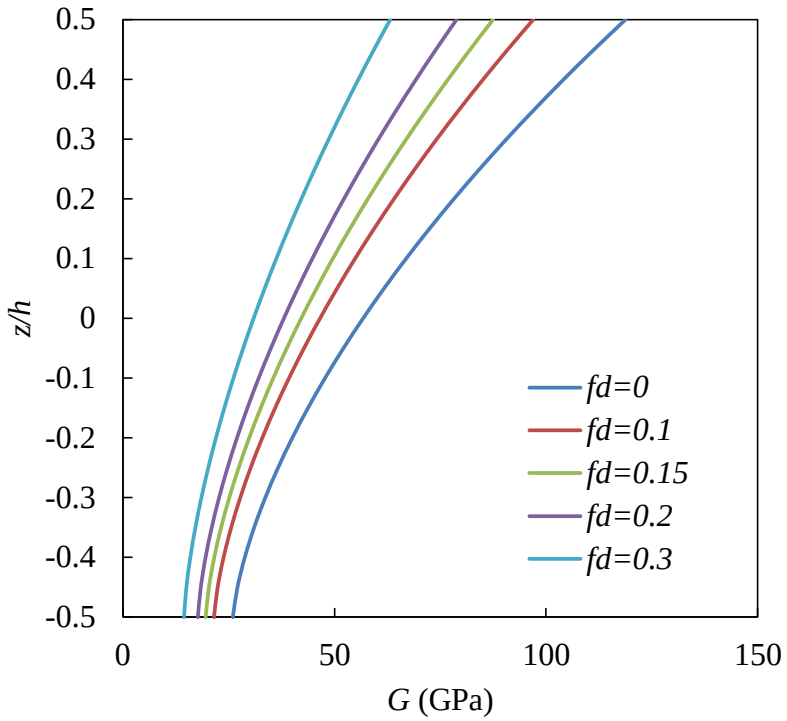

Figure 7: Effective shear modulus along thickness direction of graded Ti_2AlC/Al plate for various void volume fractions obtain from unit cell method.

As expected, the degradations of these properties with increased void volume fraction can be observed. Also, it can be seen that the Young's modulus and shear modulus have similar variation trend through thickness direction in Figure 6 and Figure 7. The bulk modulus varies more nonlinearly close to the pure Al surface, shown in Figure 8, due to the fact that the bulk modulus of Al is larger than its Young's modulus while for Ti_2AlC the former is smaller than the latter.

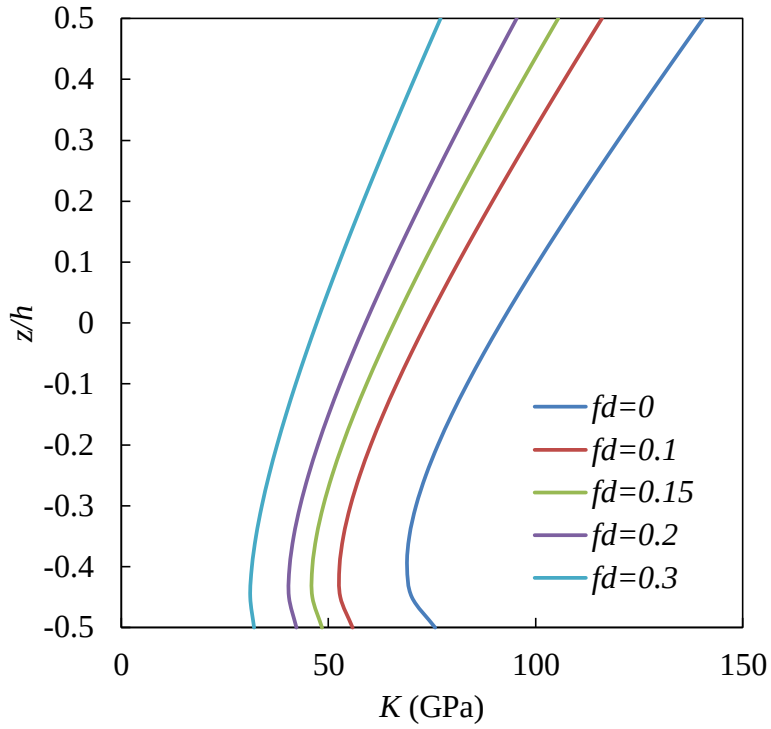

Figure 8: Effective bulk modulus along thickness direction of graded Ti_2AlC/Al plate for various void volume fractions obtain from unit cell method.

The FE results are presented in terms of non-dimensional stress and displacements. The non-dimensional parameters used here are: deflection along mid-plane, w_0/h; axial displacement, $\bar{u} = u/h$; axial stress, $\bar{\sigma}_{xx} = \sigma_{xx}/q_0$; transverse shear stress $\bar{\sigma}_{yz} = \sigma_{yz}/q_0$.

Under mechanical loading, finite element results of non-dimensional deflection w_0/h along mid-plane at $x=a/2$ with different void volume fractions for graded Ti_2AlC/Al plate are shown in Figure 9. As expected, the deflection of plate along mid-plane increases as the void volume fraction increases, i.e., stiffness degrades.

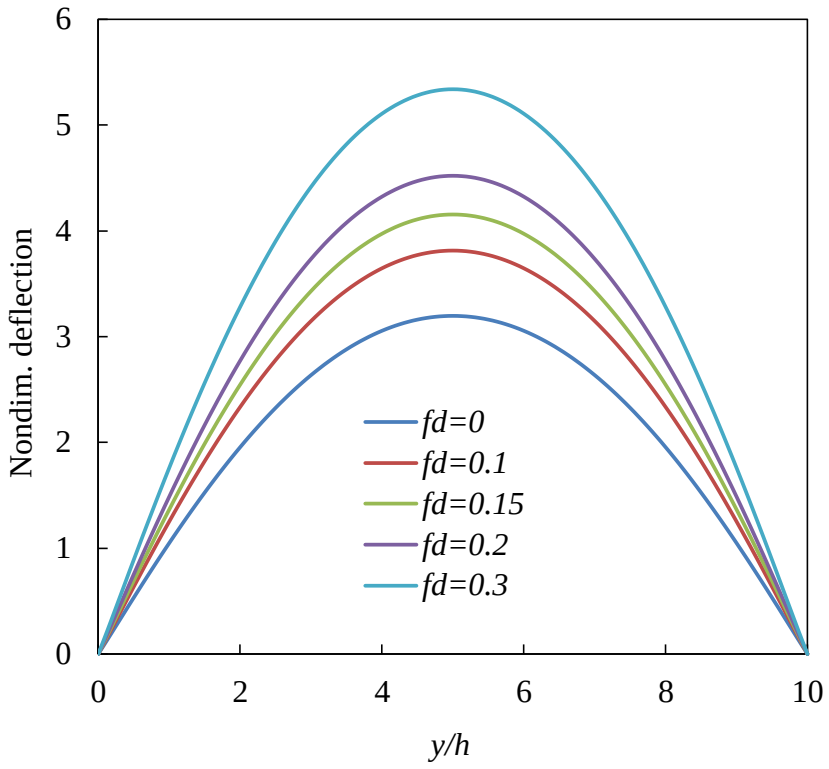

Figure 9: Non-dimensional deflection w_0/h along mid-plane at $x=a/2$ for different void volume fractions.

Figure 10 and Figure 11 give the through thickness distributions of displacements for various void volume fractions. In general, the absolute value of non-dimensional axial displacement u is larger in the part close to the top surface (Ti_2AlC side) than that near the bottom surface (Al side) of the plate, see in Figure 10. In Figure 11, the nonlinear distribution of deflection in thickness direction implies that the inextensible assumption made by most 2D plate theories is not valid in this case. Also, as volume fraction increases, both axial displacement and deflection increase (in absolute value).

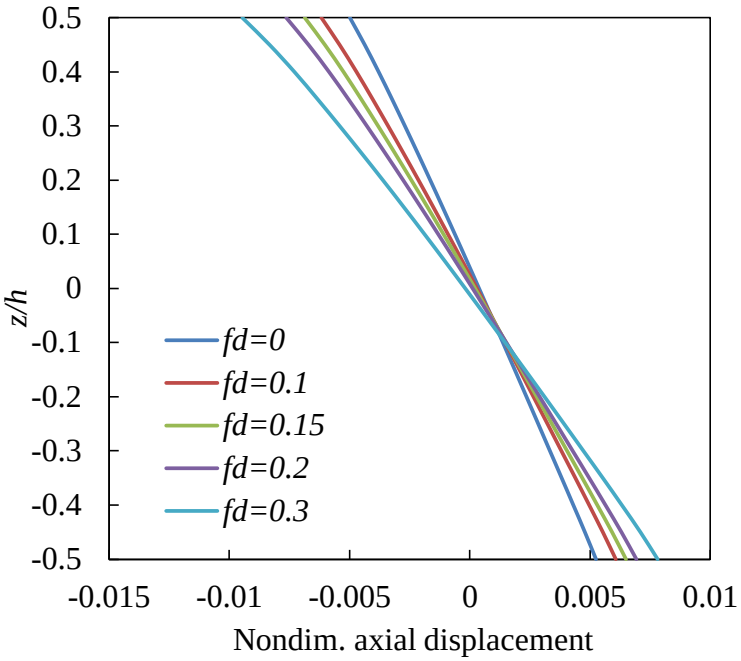

Figure 10: Through-thickness distributions of non-dimensional axial displacement *u*/*h* for different void volume fractions.

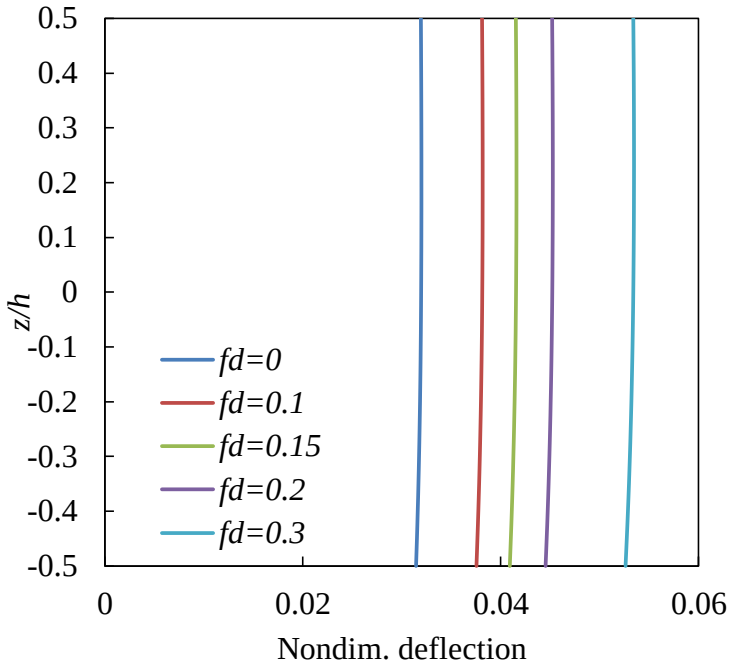

Figure 11: Through-thickness distributions of non-dimensional deflection *w*/*h* for different void volume fractions.

Figure 12 shows the comparison of FE results of through thickness distribution of axial stress for graded Ti_2AlC/Al plate and a laminate shell with 10 layers piled up with elastic properties of each layer calculated from unit cell method at the mid-point of graded Ti_2AlC/Al plate. It shows that the FE results for these two cases agree well.

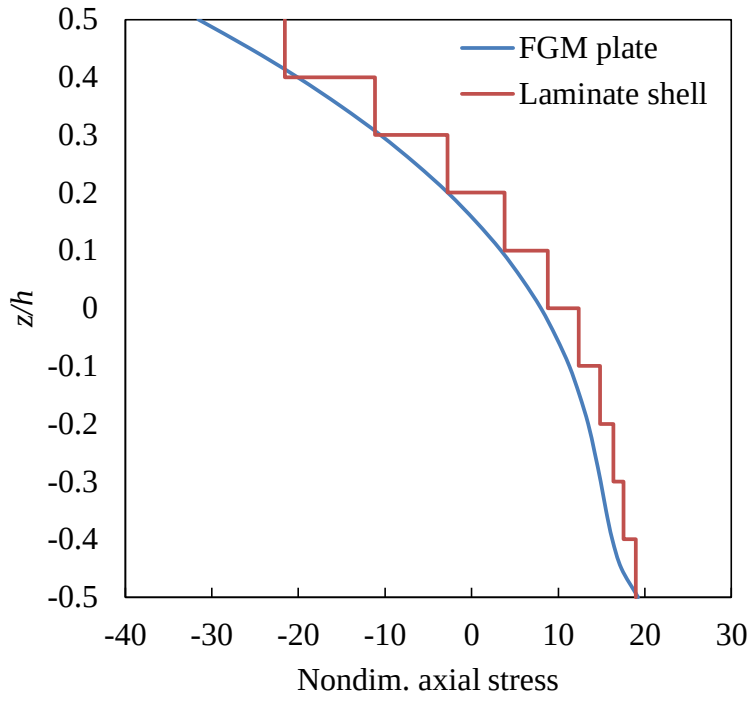

Figure 12: Comparison of through-thickness distributions of non-dimensional axial stress $\bar{\sigma}_{xx}$ of the graded Ti_2AlC/Al plate and laminate shell for various f_d values.

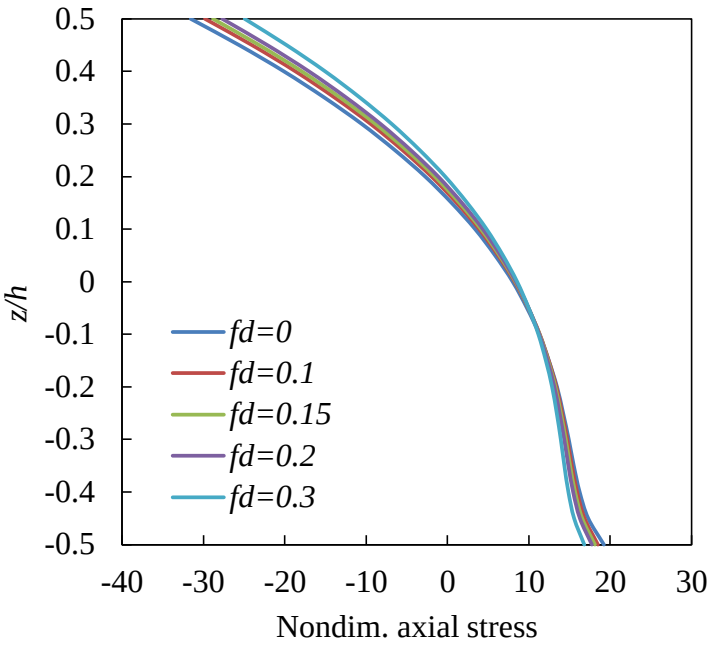

Figure 13: Through-thickness distributions of non-dimensional axial stress $\bar{\sigma}_{xx}$ (at $x=a/2$, $y=a/2$) of the graded Ti_2AlC/Al plate for various f_d values.

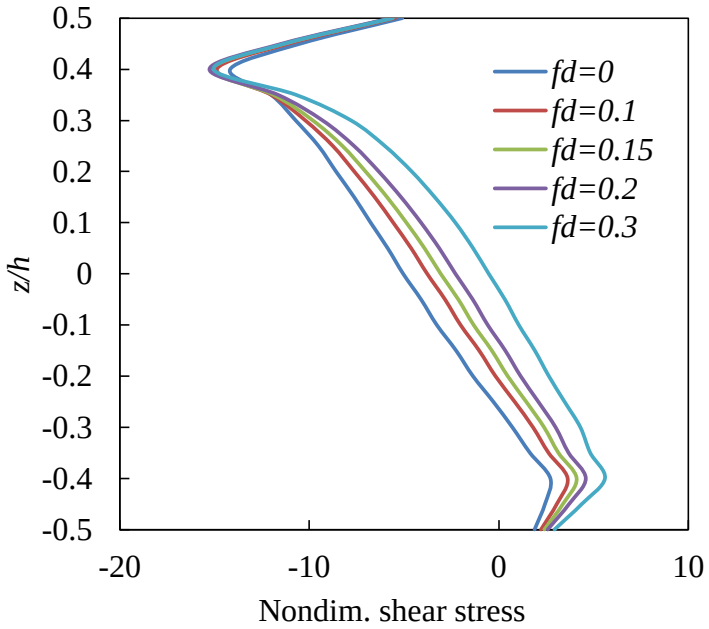

Figure 14: Through-thickness distributions of non-dimensional transvers shear stress $\bar{\sigma}_{yz}$ (at $x=a/2$, $y=0$) of the graded Ti_2AlC/Al plate for various f_d values.

Figure 13 and Figure 14 plot the through thickness distributions of axial and transverse stresses for various void volume fractions. It can be seen in Figure 13 that the through thickness distributions of axial stress become slightly smaller with rising void volume fraction. The location with zero axial stress through thickness direction under bending is not at the mid-point, but at around 0.2-0.3*h* in Ti_2AlC rich side, and this location moves upward as void volume fraction increases. On the other hand, the transverse shear stress altered significantly in the middle and lower part of plate in thickness direction for different void volume fractions.

It is noteworthy that although it is convenient to get effective elastic moduli of multiphase composites using micromechanics based homogenization methods, the phase geometry description in these methods are highly simplified and followed with certain assumptions (e.g., dilute solution assumption in some classic micromechanics based homogenization methods). Therefore, a more detailed meso-scale model based on real microstructure of multiphase composite is needed, especially for modeling of nonlinear behavior of multiphase composite, such as plasticity, damage and plasticity-damage coupled problem. To meet this need, representative volume element (RVE) concept is adopted in modeling multiphase composites and investigation of their thermomechanical behavior in the following chapters.

CHAPTER III

COMPUTATIONAL MODELING OF ELASTOPLASTIC BEHAVIOR OF STAINLESS-STEEL/BRONZE INTERPENETRATING PHASE COMPOSITES WITH DAMAGE EVOLUTION

In this chapter, an elastoplastic finite element model for stainless-steel/bronze interpenetrating phase composites (IPCs) with damage evolution is developed. Detailed 3D representative volume elements (RVE) and corresponding finite element models are generated based on the microstructure of the stainless-steel/bronze IPCs to study their mechanical and thermal expansion properties. A mixed boundary condition for uniaxial loading is implemented in the finite element models. The predicted effective elastic moduli are compared with those obtained from unit cell method and the Hashin-Shtrikman bounds. The effective elastoplastic properties obtained from finite element models of 3D RVEs with thermal residual stresses are then used as fully dense matrix material in the Gurson-Tvergaard-Needleman (GTN) constitutive model to investigate the influence of voids on the elastoplastic and evolutionary damage behavior of composites under uniaxial tension. Numerical results are compared with experimental data, and the effect of the damage evolution on plastic flow of the composites is discussed. The numerical results obtained from finite element models have very good correlation with the experimental results and provide useful insights on how thermal residual stresses and voids nucleation affect the mechanical properties of the stainless-steel/bronze IPCs.

3.1 Elastoplastic behavior of stainless-steel/bronze IPC with micro-damage — Gurson-Tvergaard-Needleman model

For a ductile media containing a dilute concentration of voids, Gurson in [60] proposed a yield condition as a function of the void volume fraction *f*. This yield condition was later modified by Tvergaard [61] to the form

$$\Phi = \left[\frac{q}{\sigma_y\left(\bar{\varepsilon}_m^{pl}\right)}\right]^2 + 2q_1 f \cosh\left[-q_2 \frac{3p}{2\sigma_y\left(\bar{\varepsilon}_m^{pl}\right)}\right] - \left(1+q_3 f^2\right) = 0 \tag{3.1}$$

where q is the von Mises stress,

$$q = \sqrt{\frac{3}{2}\mathbf{S}:\mathbf{S}}, \quad \mathbf{S} = p\mathbf{I} + \boldsymbol{\sigma}, \quad p = -\frac{1}{3}\boldsymbol{\sigma}:\mathbf{I}, \quad \bar{\varepsilon}_m^{pl} = \int_0^t \sqrt{\frac{2}{3}\dot{\varepsilon}_m^{pl}:\dot{\varepsilon}_m^{pl}}\,\mathrm{d}t \tag{3.2}$$

σ_y is the yield stress of the fully dense matrix material as a function of $\bar{\varepsilon}_m^{pl}$, the equivalent plastic strain in the matrix $\bar{\varepsilon}_m^{pl}$, and $\mathbf{I}$ is the second-order identity tensor; q_1, q_2, and q_3 are material parameters: q_1 affects the yielding by modifying the void volume fraction *f*; q_2 can be seen as a corrective factor for the hydrostatic component *p*; and q_3 is related by q_1 by $q_3 = q_1^2$.

The presence of pressure in the yield condition results in non-deviatoric plastic strains. Plastic flow is assumed to be normal to the yield surface:

$$\dot{\boldsymbol{\varepsilon}}^{pl} = \dot{\lambda}\frac{\partial\Phi}{\partial\boldsymbol{\sigma}} \tag{3.3}$$

where $\dot{\lambda}$ is the plastic consistency parameter. The plastic hardening of the fully dense matrix material is described through $\sigma_y\left(\bar{\varepsilon}_m^{pl}\right)$. The evolution of the equivalent plastic

strain in the matrix material is obtained from the following equivalent rate of plastic work expression:

$$(1-f)\sigma_y \dot{\bar{\varepsilon}}_m^{pl} = \boldsymbol{\sigma} : \dot{\boldsymbol{\varepsilon}}^{pl} \tag{3.4}$$

The total change in void volume fraction f can be expressed as

$$\dot{f} = \dot{f}_{\mathrm{g}} + \dot{f}_{\mathrm{n}} \tag{3.5}$$

where $\dot{f}_g$ is the void volume fraction change due to growth of existing voids and $\dot{f}_n$ is the void volume fraction change due to nucleation of new voids. Coalescence of voids is neglected in this study due to the lack of supporting experimental data. Growth of the existing voids is based on the law of conservation of mass and the assumption that the matrix material is plastically incompressible,

$$\dot{f}_g = (1-f)\dot{\boldsymbol{\varepsilon}}^{pl} : \mathbf{I} \tag{3.6}$$

Nucleation of the new voids occurs mainly at the second-phase particles, by decohesion of the particle-matrix interface or by particle fracture [118]. Different kinds of nucleation criteria have been formulated within this general phenomenological framework, [60, 62], which can be described by the simple two parameter relation

$$\dot{f}_n = A\dot{\bar{\varepsilon}}_m^{pl} + \frac{1}{3}B(\boldsymbol{\sigma} : \mathbf{I}) \tag{3.7}$$

where A gives the dependence of the void nucleation rate on the matrix effective plastic strain increment and B gives the dependence on the rate of increase of hydrostatic stress. For nucleation of voids only controlled by the plastic strain, the parameters are specified by [62]

$$A = \frac{f_N}{s_N \sqrt{2\pi}} \exp\left[-\frac{1}{2}\left(\frac{\bar{\varepsilon}_m^{pl} - \varepsilon_N}{s_N} \right)^2 \right], \quad B = 0 \tag{3.8}$$

where ε_N and s_N are the mean value and standard deviation for the normal distribution of the nucleation strain, and f_N is the volume fraction of the void nucleating particles. If void nucleation is neglected, then for zero or negative stress triaxiality the GTN model predicts no increase in damage.

3.2 3D RVEs and finite element modeling

The stainless-steel/bronze interpenetrating phase composites were made by infiltrating bronze in sintered stainless-steel powder skeletons to produce a nearly fully dense stainless-steel/bronze IPCs. The sintered stainless-steel skeleton was produced using spherical stainless-steel powders using three-dimensional printing technique [21]. There are about 1% of voids located within the bronze phase of the produced 60% and 80% IPCs. Their existence is mainly the result of incomplete infiltration or the presence of bubbles in the bronze melt [21]. In order to investigate the mechanical behavior of the stainless-steel/bronze composites, two 3D RVEs for 60% and 80% IPCs, are generated based on the micrographs of IPCs in [21] (note that 60% and 80% refer to the volume fractions of the stainless-steel phase) using the commercial software AutoCAD and Abaqus, as shown in Figure 15. The cross-sectional images of the 3D RVEs for 60% IPC and 80% IPC are shown in Figure 16.

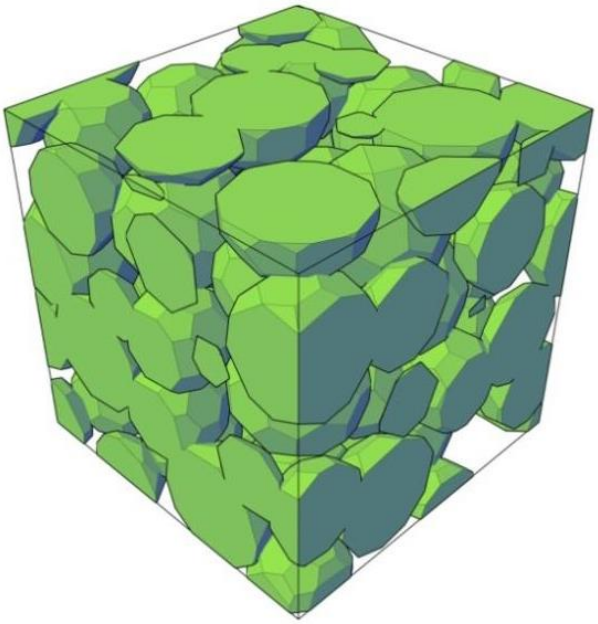

(a)

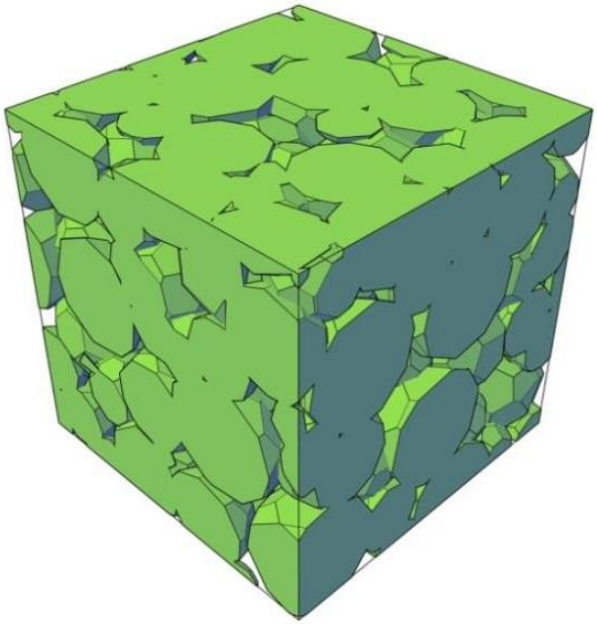

(b)

Figure 15: 3D RVEs: (a) 60% IPC and (b) 80% IPC.

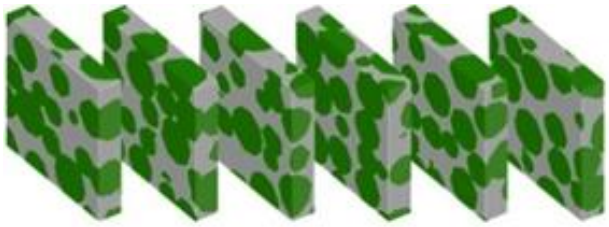

(a)

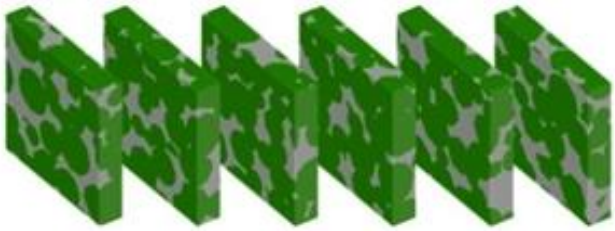

(b)

Figure 16: Cross-sectional images of the 3D RVEs: (a) 60% IPC and (b) 80% IPC.

3.2.1 Simulated microstructure

In modeling the stainless-steel/bronze IPCs, simplified geometries of the stainless-steel and bronze phases have been used to generate the microstructure of IPCs [9, 21, 59]. However, it should be mentioned that such three-dimensional representations, such as 3D trusses and spherical shape particles, do not accurately reflect the shape of the phases. In fact, the irregularity of the phase shape is intensified as the phase volume fraction increases as shown in the micrographs of the 60% and 80% IPCs in [21]. Moreover, it has been found in [119] that the RVE of particulate composites with spherical shape particles tends to show higher strength than the ones with irregular shape particles. This is attributed to the increased level of stress concentration at the regions

with geometric singularity for the irregular shape particles, which is actually more close to the stress state of the real microstructure of the composites. Therefore in this study, instead of spherical phases, truncated icosahedron (i.e., soccer ball shape) is adopted to represent the shape of stainless-steel phase in order to reflect the irregularity of the outer surface of the interconnected particle phase more realistically. Another advantage of using truncated icosahedron shape particles is that it can tremendously reduce the number of elements in the finite element mesh. The reason is that when we use perfect spherical shape, there exist many tiny segments of curved surfaces due to the connectivity of the particles. It leads to much denser mesh as compared to the truncated icosahedron shape with only flat surfaces that are easier to mesh.

The dimensions of the two 3D RVEs for 60% and 80% IPCs are taken to be 150μm × 150μm × 150μm, and three different sized stainless-steel particles are used in the 3D RVEs. As it is difficult to describe the size of a truncated icosahedron, the radiuses of the corresponding circumscribed spheres of the truncated icosahedrons are used to represent the size of the particle. They are 25μm, 20μm, and 15μm, respectively, and the gradation of the corresponding particles is assumed to be approximately 2:2:1. There are 96 randomly distributed interconnected stainless-steel particles in the RVE of 60% IPC and 171 in the RVE of 80% IPC.

In order to achieve desired volume fraction of particles, the connectivity of neighboring particles is also controlled. As illustrated in Figure 17 schematically, the relation between adjoining particles can be categorized into three states: separation, in contact, and interpenetration states. Although all these three states may exist in the real

microstructure of the IPCs at the same time, the in contact state, see in Figure 17 (b), is not considered in our model for simplicity. Since for this state, additional contact properties need to be defined, which is unknown. Also, numerical singularity may arise at the sharp tip of the bronze matrix region which is close to the contact point between particles. Hence, only separation and interpenetration states, i.e. Figure 17 (a) and (c), are considered in the modeling, which is achieved by controlling the range of the distance between centers of particles.

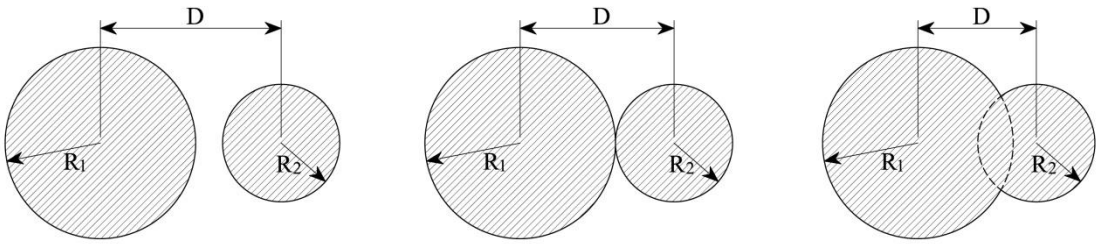

(a) (b) (c)

Figure 17: Schematic representation of the relation between adjoining particles: (a) separation state ($D > R_1 + R_2$), (b) contact state ($D = R_1 + R_2$), and (c) interpenetration state ($D < R_1 + R_2$).

In the 3D RVEs, it is assumed that the IPCs consisted of only two phases that are perfectly bonded at the interface. Although other phases exist in the IPCs due to diffusion during the manufacturing process, such as the second tin-rich sub phase and the diffused iron in the bronze, the volume fraction of these phases is negligible. Therefore, for simplicity, they are not taken into account in the 3D RVEs, neither is

porosity considered in the 3D RVEs for the reasons that the volume fraction of the voids is very small (1.0%-1.5%). Except for damage evolution, initial porosity has relatively small influence on the mechanical properties of the IPCs. When it comes to the study of damage, the Gurson-Tvergaard-Needleman constitutive model is adopted, which has the capability to include initial porosity in an effective media, without the need to model the voids explicitly in the 3D RVEs.

3.2.2 FE mesh and boundary conditions

In order to determine the approximate global element size for the given FE models of 3D RVEs, mesh sensitivity study is carried out. The approximate edge lengths of elements used here are 10μm, 8μm, 6μm, and 5μm, and the corresponding meshes are generated automatically using the commercial software Abaqus. Due to the complex microstructure of the 3D RVEs, C3D10 elements (ten-node quadratic tetrahedral element) are used because they are geometrically versatile and very convenient to mesh complex shapes. Examples of FE models of RVEs with 10μm and 6μm as approximate element edge lengths for 60 % and 80 % IPCs are illustrated in Figure 18. The relation between the element edge length versus total element number for the given IPCs is shown in Figure 19. It can be seen that as the approximate global element size decreases as the total element number increases exponentially. Very large amounts of computer memory and processor time are required when the number of element is above 150,000. Further, it is noteworthy that the total number of elements of the finite element mesh for 80% IPC is much greater than that of 60% IPC for the same approximate global element size.

This is because, geometrically, the 3D RVE of 80% IPC has much more small edges resulting from the interpenetration of the stainless-steel phase.

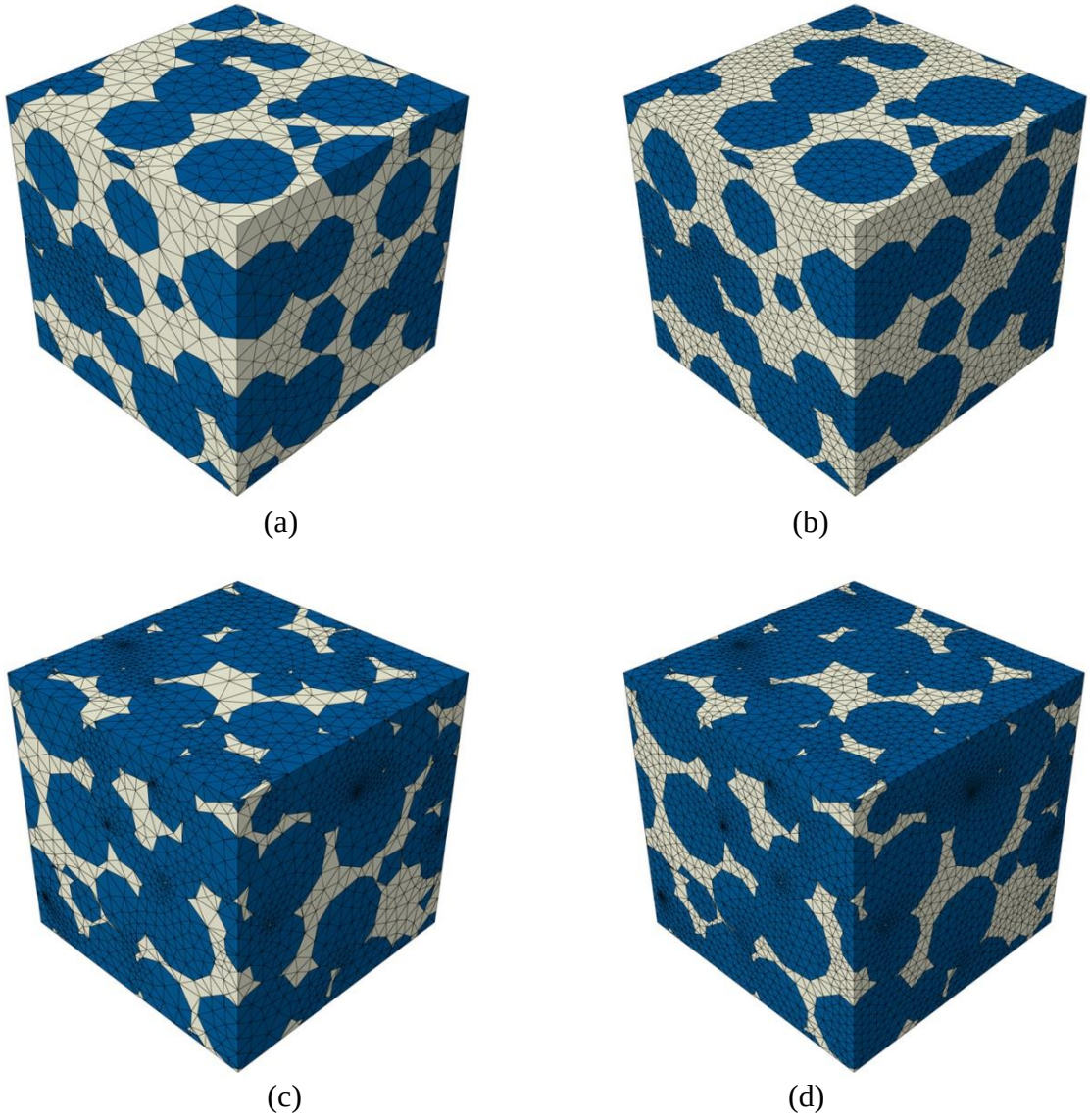

Figure 18: Examples of FE models used in mesh sensitivity study: (a) mesh for 60% IPC with element edge length= 10μm, (b) mesh for 60% IPC with element edge length= 6μm, (c) mesh for 80% IPC with element edge length=10μm, and (d) mesh for 80% IPC with element edge length=6μm.

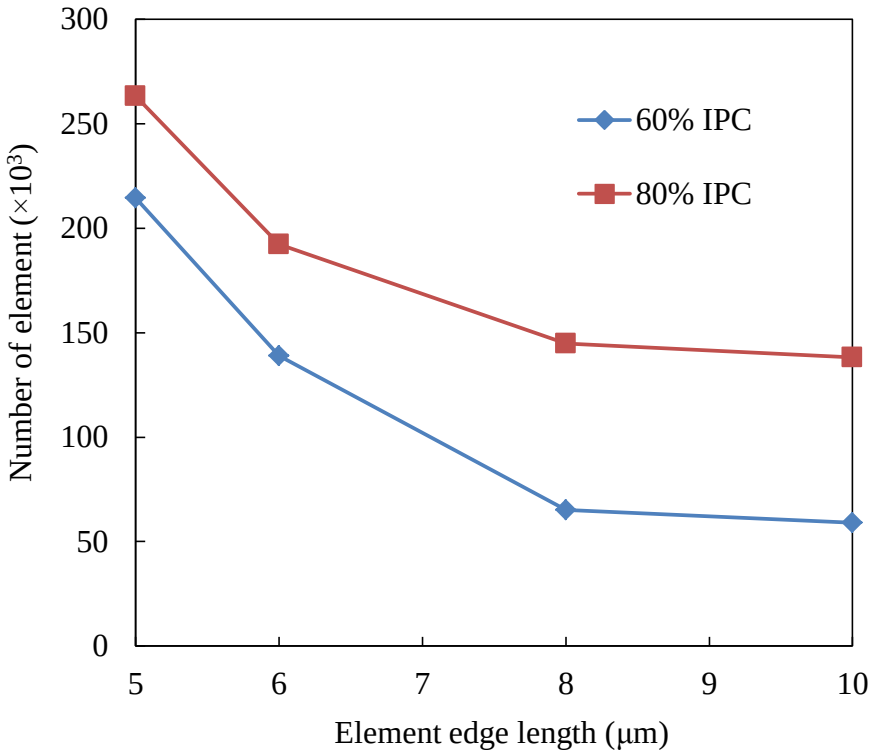

Figure 19: Total element number versus element edge length.

Nonlinear FE analyses of elastoplastic behavior of the given IPCs are carried out to study the mesh sensitivity of the FE models created. Isotropic hardening and von Mises yield criterion are used in these analyses. For simplicity, simply supported boundary conditions are applied. The results for 60% and 80% IPCs are shown in Figure 20 and Figure 21, respectively. It can be seen that for FE model of 60% IPC, the initial elastic response is independent of the mesh density, while the plastic response is mesh density-dependent. For example, in Figure 20, at strain around 0.13, when the element edge length decreases from 8μm to 6μm, the difference between the stress levels for the

two mesh densities is around 4.5%. It is found that this discrepancy reduces to 1.9% when the element edge length is reduced from 6μm to 5μm. In contrast, the effect of mesh density on the elastoplastic response of the FE model is not significant for the 80% IPC. As can be seen from Figure 21, the difference between the results obtained from FE models with element edge lengths 10μm, 8μm, 6μm and 5μm are all under 2%. Even this small difference is due to the fact that local plasticity theory, such as von Mises plasticity theory, is mesh-sensitive. As compared to 60% IPC, 80% IPC has larger volume fraction of stainless-steel phase, which has much higher yield strength than bronze phase. In other words, more parts of 60% IPC yield locally than 80% IPC under the given strain level. Therefore, the former is more mesh sensitive than the latter. Taking accuracy and computational efficiency into consideration, 6μm is selected as an approximate global element edge length for FE models of both 60% and 80% IPCs in the subsequent numerical studies. There are 138,709 elements and 182,917 elements in the corresponding FE models of 60% and 80% IPCs, respectively.

For a composite with periodic microstructure, periodic boundary conditions (PBCs) should be applied in order to make an RVE represent a volume of the material embedded within a much larger volume. In the PBCs, one should constrain the relationship between each pair of nodes on the matching meshes of opposite faces of the RVE. However, the RVEs used in this study are created by cutting parts of a simulated microstructure with random distributed phases based on actual microstructure of a heterogeneous material, and they do not exhibit geometry periodicity. Therefore, instead of PBC, a mixed boundary condition designed for such RVEs [120] are imposed in this

study: uniform displacements are imposed on the faces perpendicular to the loading direction. To simulate an interior domain compatible with the surrounding material, the faces parallel to the loading direction remain straight and parallel during deformation (i.e., no shear).

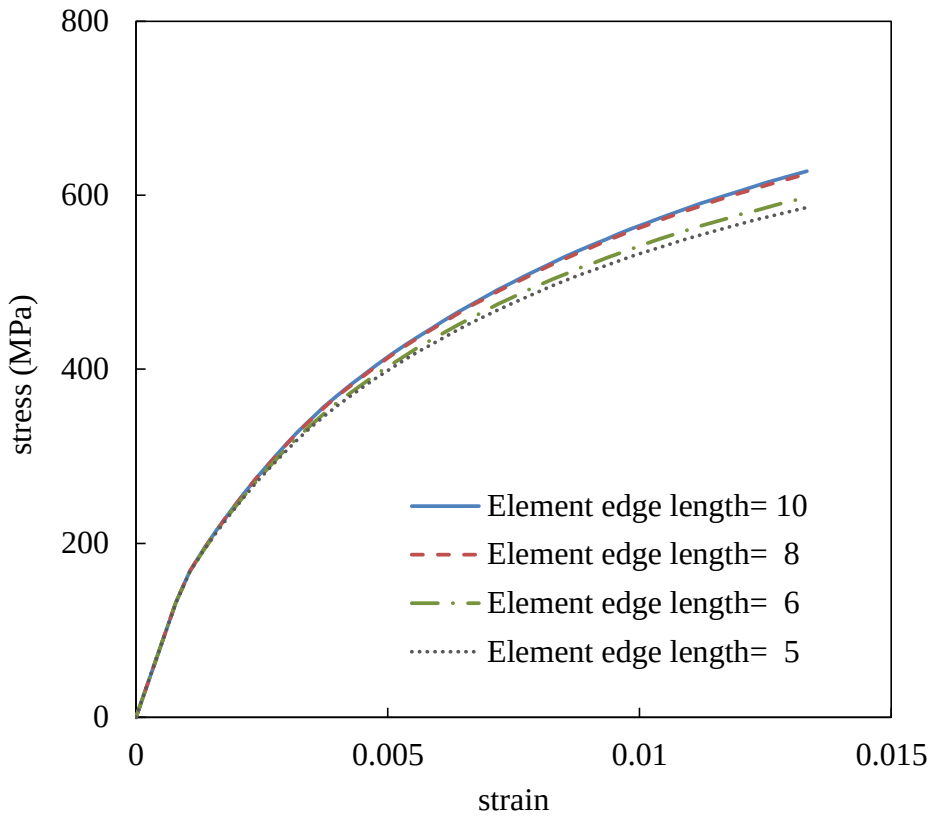

Figure 20: Tensile behavior of 60% IPCs with various mesh density.

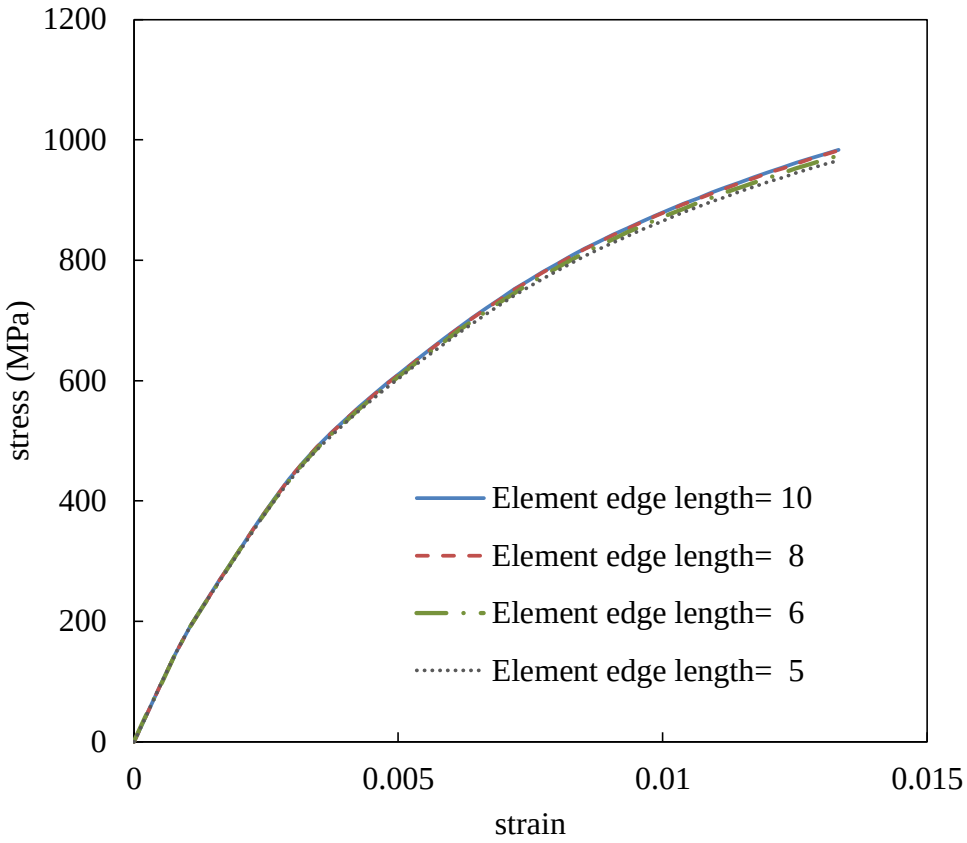

Figure 21: Tensile behavior of 80% IPCs with various mesh density.

3.3 Numerical simulation and results

In the FE analysis, interpenetrating phase composites made of stainless-steel and bronze is studied. Such composites had been produced using sintered stainless-steel powder skeletons infiltrated with bronze by three-dimensional printing [21]. Two interpenetrating phase composites with 60% and 80% volume fractions of stainless-steel

were made and studied, which are referred to as the 60% IPC and 80% IPC, respectively. The material properties of the two phases are listed in Table 2 [59].

Table 2: Material constants of the constituent phase in 420 stainless-steel/ 150P bronze IPC.

Material	Young's modulus E (GPa)	Poisson's ratio	Shear modulus G (GPa)	Initial yield stress σ^s (MPa)
420 stainless	210.0	0.30	81.40	1432.62
150P bronze	110.0	0.33	41.35	135.96

3.3.1 Effective elastic properties

Hashin-Shtrikman bounds are the most well-known effective elastic moduli bounds that are derived from variational principles and formulated in terms of the polarization stress. They give meaningful bounds on isotropic and transversely isotropic effective elastic moduli to all homogeneous composites without specifying phase geometry. Also, the aforementioned micromechanics based unit cell method, which is particularly designed for interpenetrating phase composites, is used here to predict the effective elastic moduli of the given IPCs [59]. The geometry of the unit cell for a macroscopically isotropic, two-phase interpenetrating phase composite has been shown in Figure 1.

The effective elastic constants are obtained by decomposing the unit cell into parallel and series sub-cells based on a combination of iso-stress and iso-strain assumptions. As mentioned in Chapter II, assuming $a_1=b_1=c_1$, $a_2=b_2=c_2$ in Figure 1, and defining a non-dimensional quantity $a = a_1/(a_1 + a_2)$, the expression of the effective Young's modulus and shear modulus of the two-phase IPC are expressed in Eq. (2.1) and Eq. (2.2).

For the IPCs that consist of stainless-steel and bronze, comparisons of the effective Young's modulus as a function of stainless-steel volume fraction obtained from Hashin-Shtrikman bounds and unit cell method are shown in Figure 22. It can be seen that the Hashin-Shtrikman bounds are very narrow due to the relatively small contrast between the moduli of the two phases. The curve of the unit cell method lies in between of the Hashin-Shtrikman upper and lower bounds and is more close to the Hashin-Shtrikman lower bound. Under simple elastic conditions, unit cell method as well as the Hashin-Shtrikman bounds is sufficient to predict the effective modulus for such a two-phase composite. However, the measured effective Young's modulus of the given IPCs is a little bit lower than the predictions of these two micromechanics based methods (e.g. approximately 3.6% and 5.4% lower than the predictions of unit cell method for 60% IPC and 80% IPC, respectively), see Figure 22. The main reason is the presence of voids in bronze phase, especially for 80% IPC.

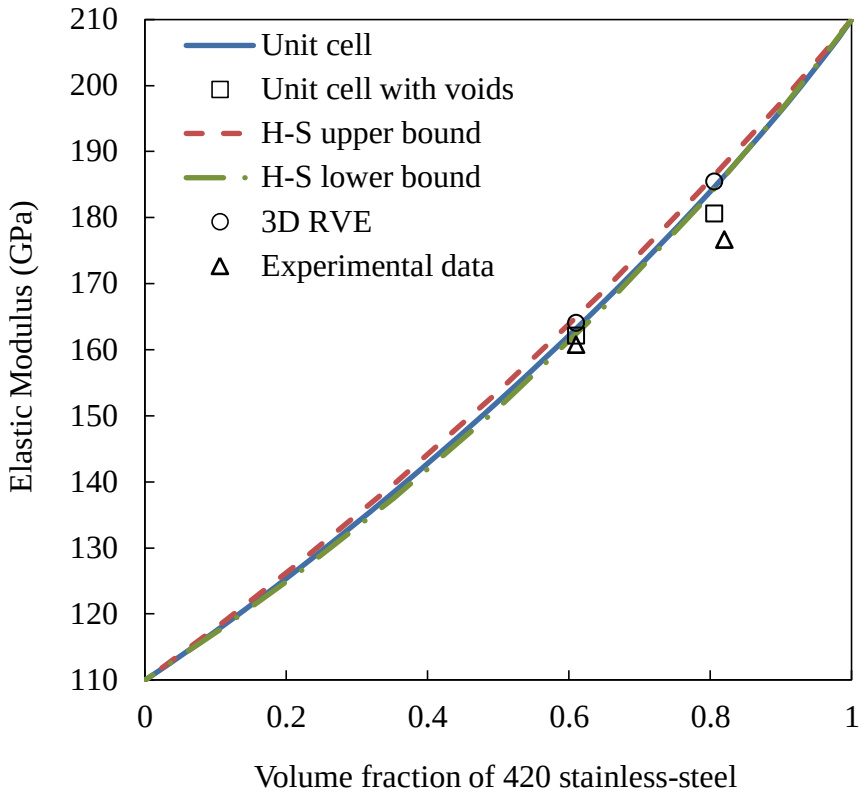

Figure 22: Effective moduli vs. volume fraction of stainless-steel, for stainless-steel/bronze IPC.

The unit cell method mentioned above also has the capability to account for the inclusion shapes of phases by utilizing Mori-Tanaka method with iso-stress and iso-strain assumptions [59]. Using the unit cell method in which voids are introduced as a third phase in the original two-phase IPCs, we can predict the effective Young's modulus of the composites considering porosity. In Figure 22, it is shown that by considering voids, the difference of effective Young's modulus between predictions and measurements is reduced to 1.8% and 2.3% for 60% IPC and 80% IPC, respectively; this

is in an acceptable range. Therefore, we can conclude that voids located within bronze phase and along interface slightly affect the effective Young's modulus.

Other possible explanations for the reduction in the initial modulus are: (1) the resultant plastic deformation in the IPCs induced by thermal residual stresses due to cooling process. Since the Young's modulus is obtained by the tensile test, the initial response of the composite is affected by the state of the initial stress, especially the resultant plastic deformation in bronze; (2) even at very small strain level, there might be some damage evolution during the tensile test. Of course, this effect can be totally neglected if non-destructive test technique is used in measuring the effective Young's modulus of the composites. However, due to the fact that the strain level at which effective Young's modulus was measured in the test is not known, and the results from unit cell method considering porosity are reasonable when compared with the experimental measurements, the effects of thermal residual stress and damage evolution on the effective elastic moduli will not be addressed using the 3D RVE and corresponding FE model in this study.

Next, the effective elastic moduli of 60% and 80% IPCs are obtained from FE models of 3D RVEs using linear elastic material properties. Uniaxial tension and simple shear tests are simulated using the FE models of 3D RVEs with load in the x_1-, x_2-, and x_3- directions. The effective Young's moduli, Poisson's ratios and shear moduli of 60% and 80% IPCs obtained are presented in Table 3. It is found that loading direction has slight influence on the FE predicted effective elastic moduli for the given 3D RVEs, and the effective elastic moduli follow the relation $G=E/2(1+\nu)$ which is valid for linear

isotropic elastic material. Therefore, the corresponding IPC systems achieve approximate isotropy, and further we can conclude that the 3D RVEs created for 60% and 80% IPCs are statistically homogeneous and can represent the local continuum properties of the IPCs.

Table 3: Prediction of effective elastic moduli of 60% IPC and 80% IPC obtained from FE models of 3D RVEs.

	Young's modulus, E (GPa)			Poisson's ratio, ν			Shear modulus G (GPa)		
	E_{11}	E_{22}	E_{33}	ν_{12}	ν_{23}	ν_{31}	G_{12}	G_{23}	G_{31}
60% IPC	164.85	165.10	165.11	0.31	0.31	0.31	63.11	63.23	62.90
80% IPC	185.46	185.32	185.49	0.30	0.30	0.30	71.18	71.24	71.22

Comparisons of the effective Young's modulus obtained from FE models of 3D RVEs with Hashin-Shtrikman bounds and unit cell method are presented in Figure 22. Here, the average values of E_{11}, E_{22}, and E_{33} are taken as the FE predicted effective Young's modulus for the given 3D RVEs of 60% and 80% IPCs. It is shown that the predicted effective Young's moduli obtained from the FE models of 3D RVEs of 60% and 80% IPCs with elastic constituent material properties lie within the Hashin-Shtrikman bounds, and they are very close to the corresponding predictions of the unit

cell method. This good agreement with micromechanics based models can be seen as the verification of the FE models of 3D RVEs developed in this study.

3.3.2 Thermal residual stress

In the IPCs, the mismatch between the coefficients of thermal expansion for the two constituent materials leads to the development of thermal residual stress during the manufacturing process. It is mentioned in [21] that the specimen will go through final heat-treatment which involves fast furnace cooling from 940 ℃ to the room temperature. Since 832 ℃ is the solidus temperature of the bronze and it is assumed that stresses did not develop in the composite above the solidus temperature. Therefore, 832 ℃ is selected as the initial stress-free temperature. In turn, material properties such as elastic moduli, ultimate strain, coefficient of thermal expansion (CTE) as well as stress-strain relation, are also temperature dependent.

In order to investigate the effects of the thermal residual stress on the mechanical behavior of IPCs, the cooling process is simulated: the temperature is dropped from 832 ℃ to 20 ℃ uniformly throughout the entire model with increments of 20 ℃. Isotropic hardening and von Mises yield criterion are adopted in these nonlinear FE analyses while a mixed boundary condition is applied. The measured temperature dependent stress-strain curves of stainless-steel and bronze used in the nonlinear FE analyses are shown in Figure 23, while variation of Young's moduli with temperature is listed in Table 4 [21].

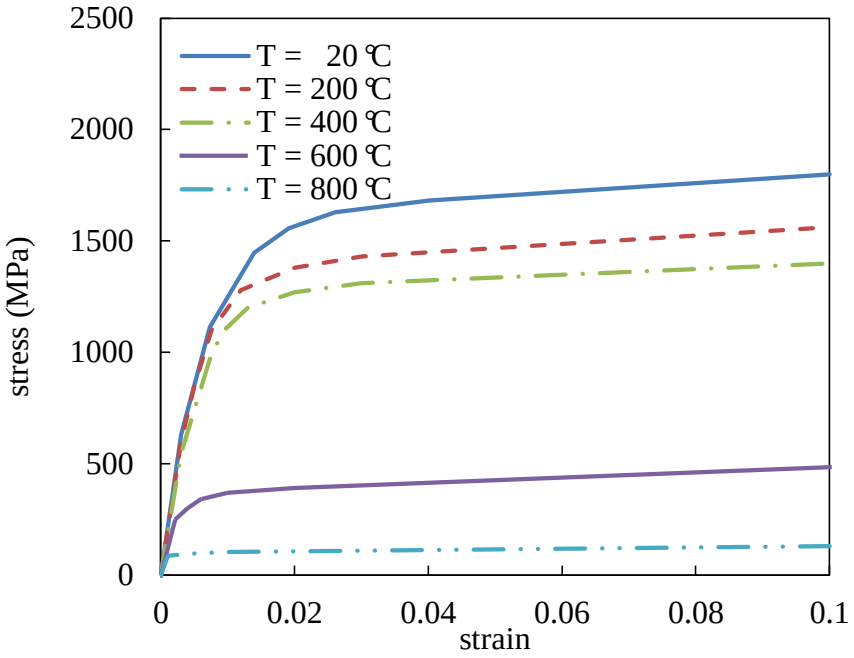

(a)

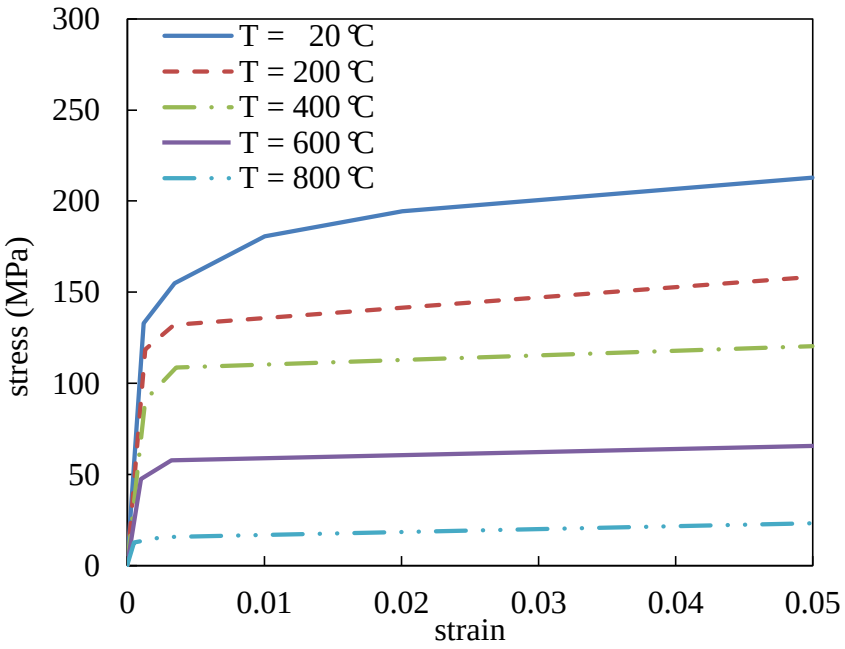

(b)

Figure 23: Tensile behavior at elevated temperatures for (a) stainless-steel, (b) bronze [21].

Table 4: Young's modulus of constituent phases of IPCs at elevated temperature.

Temperature (℃)	Young's modulus (GPa)	
	420 stainless	150P bronze
20	210	110
200	200	91
400	182	70
600	116	48
800	84	27

Figure 24 and Figure 25 show the numerical results of thermal residual stress component distributions within the bronze phase and stainless-steel phase of 60% IPC and 80% IPC, respectively. As an example, the distributions of x_3-direction axial stress component in bronze and stainless-steel of 60% IPC are plotted in Figure 24(a) and Figure 24(b), respectively. As expected, relatively high stress distributes are observed along the interface of the two phases. Although the magnitude of the maximum compressive stress in the bronze matrix is much greater than the maximum tensile stress due to the interaction of two phases at the interface regions, the axial stress component of the thermal residual stress is mainly tensile in the bronze phase and compressive in stainless-steel phase under contraction. This phenomenon can be seen even more clearly for the 80% IPC in Figure 25. Therefore, if the IPCs then subjected to uniaxial tensile loading, the stainless-steel is actually unloading from a compressive state while the bronze is being even more stretched.

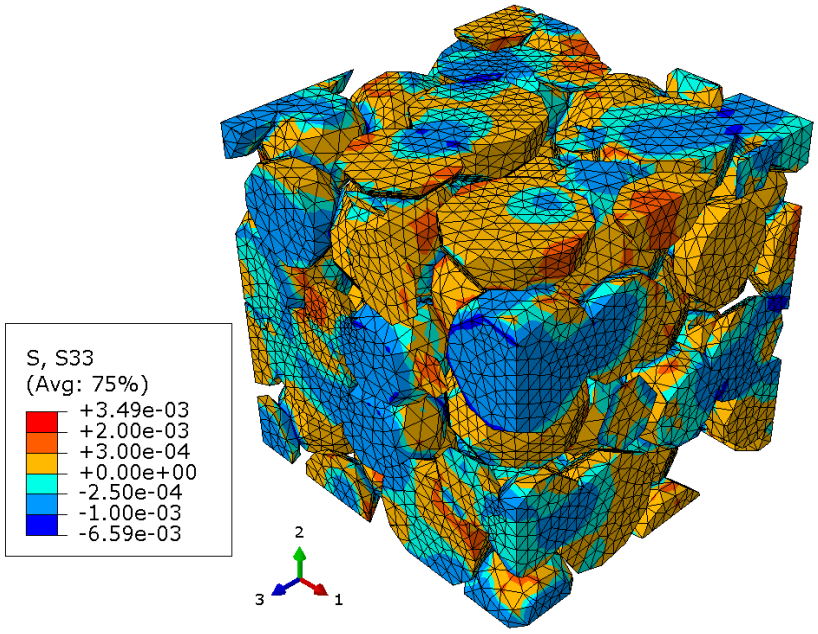

(a)

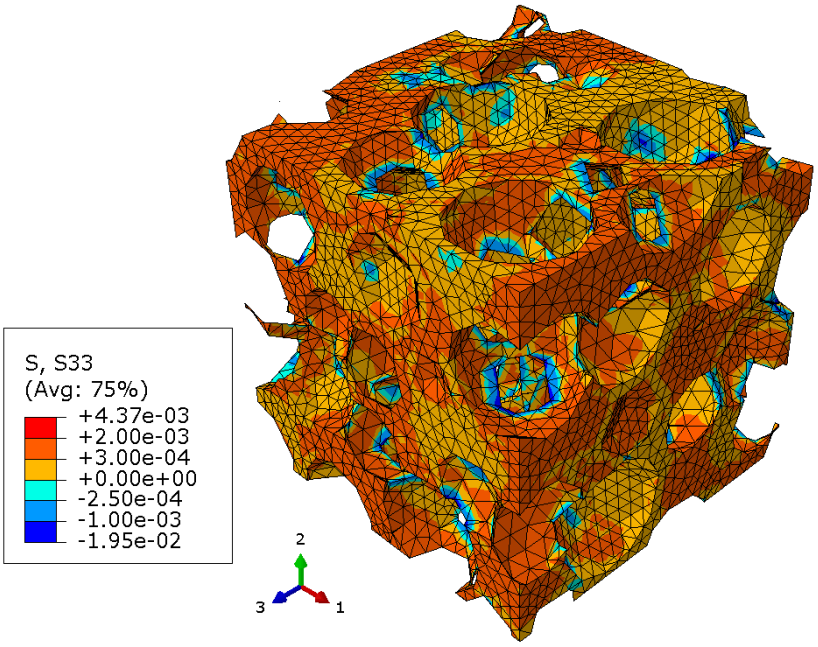

(b)

Figure 24: Axial stress distribution of 60% IPC (stress unit: 10^6MPa): (a) stainless-steel phase and (b) bronze phase.

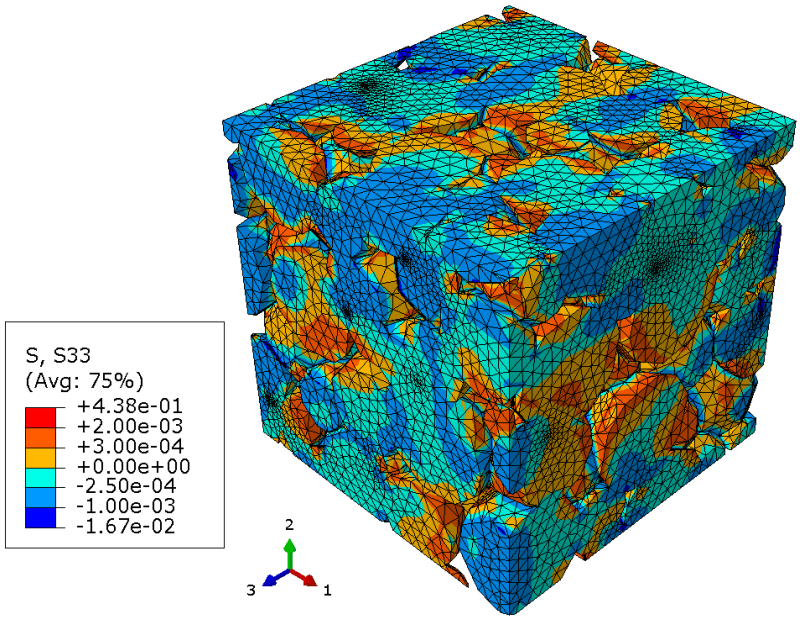

(a)

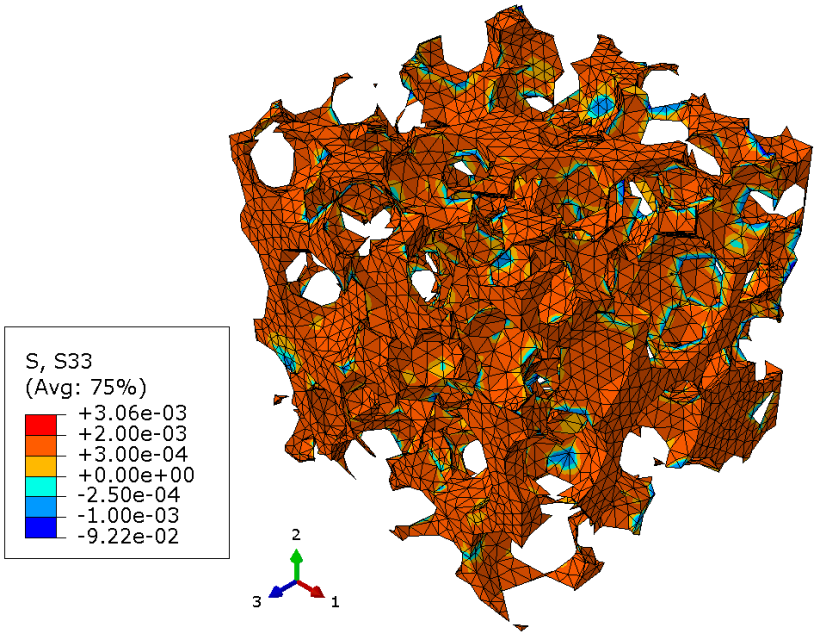

(b)

Figure 25: Axial stress distribution of 80% IPC (stress unit: 10^6MPa): (a) stainless-steel phase and (b) bronze phase.

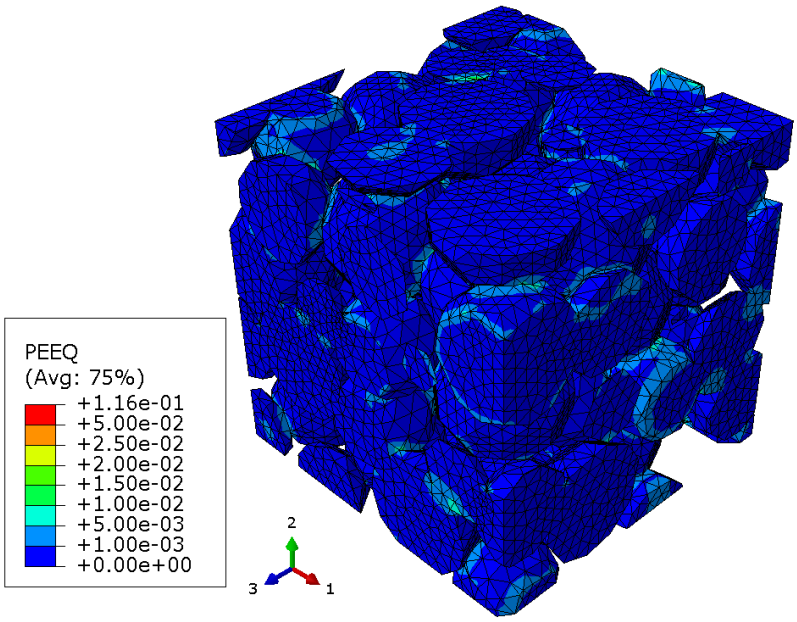

(a)

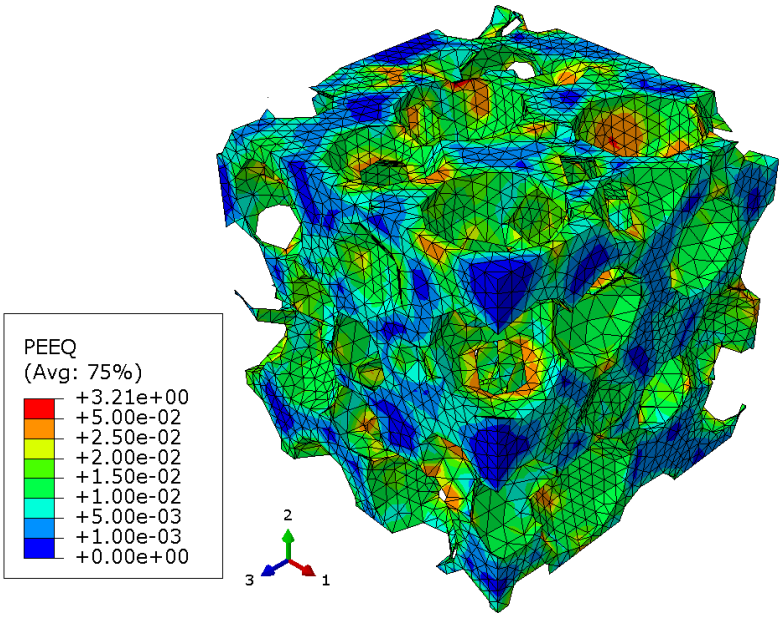

(b)

Figure 26: Equivalent plastic strain distribution of 60% IPC: (a) stainless-steel phase and (b) bronze phase.

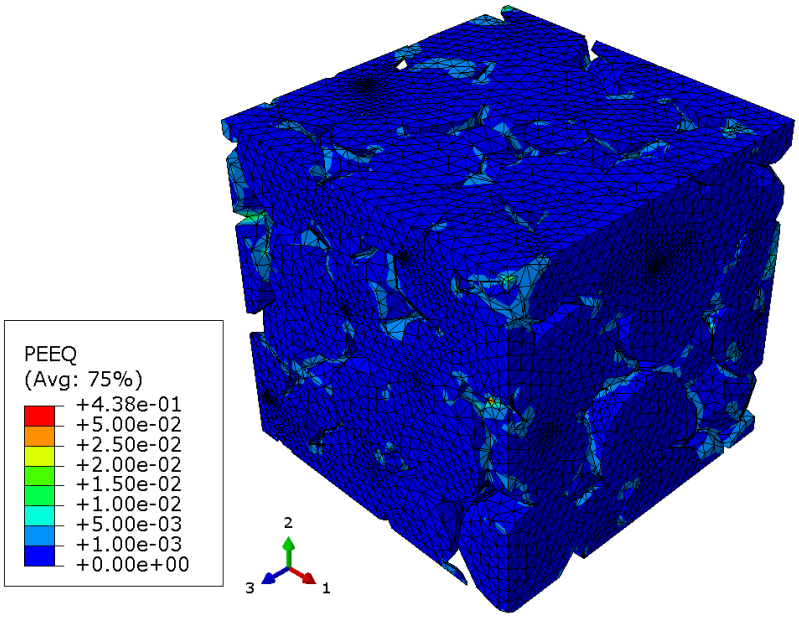

(a)

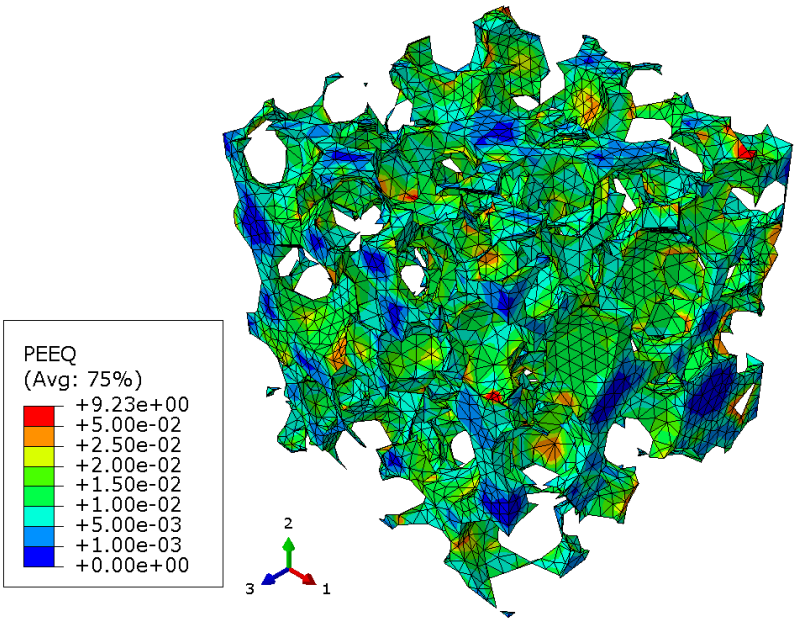

(b)

Figure 27: Equivalent plastic strain distribution of 80% IPC: (a) stainless-steel phase and (b) bronze phase.

The equivalent plastic strain distributions in stainless-steel phase and bronze phase for 60% and 80% IPCs are plotted in Figure 26 and Figure 27, respectively. Comparing the equivalent plastic strain within the stainless-steel phase and bronze phase of 60% and 80% IPCs, it can be observed that for both IPCs, considerable part of the bronze phase yields while most part of stainless-steel remains in the elastic range at the end of the cooling process.

3.3.3 Thermal expansion

The effective temperature dependent coefficients of thermal expansion (CTE) of the 60% and 80% IPCs are obtained from the FE models of 3D RVEs. The thermal residual stress is considered as the initial stress condition and the temperature is increased from 20 ℃ to 800 ℃ with 20 ℃ increment. At a given temperature, averaged dilation strains in the x_1-, x_2-, and x_3-directions are used to calculate the instantaneous CTE.

The measured temperature dependent CTE curves for the 60% and 80% IPCs as well as for the bronze and stainless-steel phases are shown in Figure 28. The sharp bends at two ends of the measured curves are caused by lagged temperature measurement on a single point of the specimen surface in the experiment. The roughness of the curves is due to the roughness of the constituent CTEs calculated from the measured values at a given temperature.

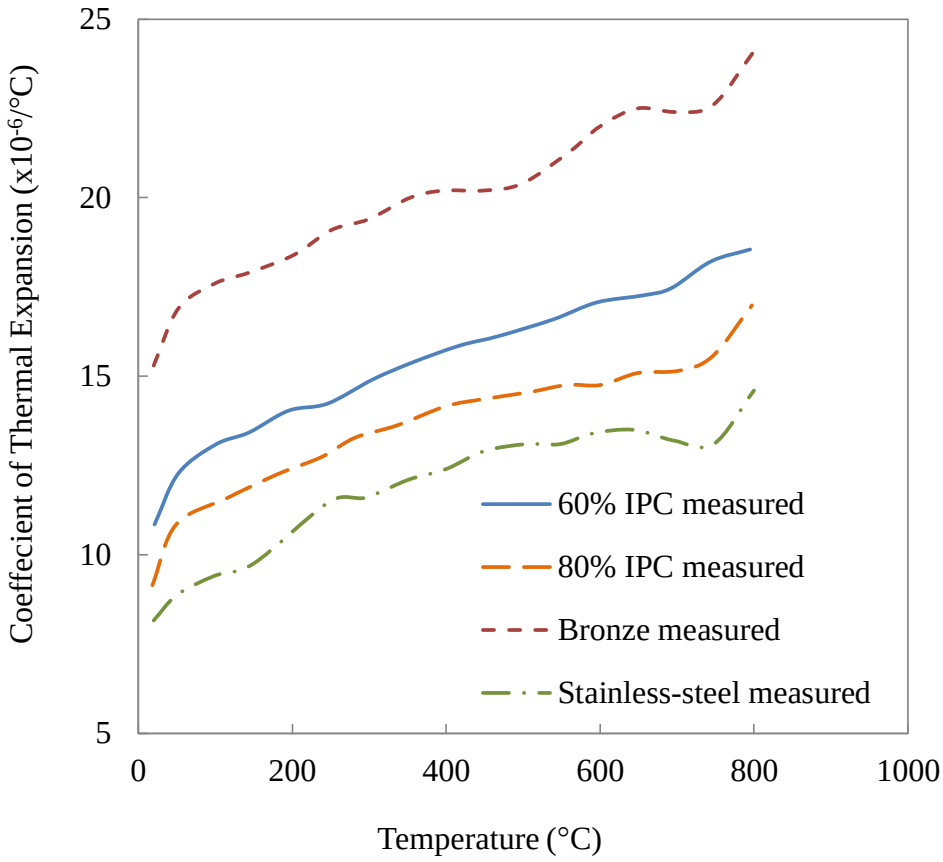

Figure 28: Measured CTE vs. temperature for stainless-steel/bronze IPCs and constituent phases [21].

Figure 29 and Figure 30 show the comparisons of the temperature dependent effective CTE among FE predictions, measured results and theoretical models for 60% and 80% IPCs, respectively. The theoretical models used in this study are based on the rule of mixtures, Turner model, and Kerner-Schapery bounds. Turner model is derived for reinforced plastics and assumes a uniform hydrostatic stress state throughout the composite. It typically provides lower bound for most of the experimental data [121].

Kerner-Schapery bounds on the other hand give meaningful bounds for an elastic composite. Since the theoretical calculations and FE analyses are obtained using the measured CTEs of the constituent phases, see Figure 28, they also have the similar features, such as sharp ends and roughness as those of measured curves.

For the theoretical predictions, it is shown in Figure 29 and Figure 30 that the rule of mixtures gives the highest CTE prediction, which is also the most close prediction comparing with the measurements, whereas the Turner model [122] gives the lowest one, and the Kerner-Schapery bounds [35] fell in between of these two. It is found that the thermal residual stress only has small influence on the CTEs of the given IPCs. The CTEs for the case considering initial thermal residual stress are lowered by an average of 0.7% and 1.3% over the 20-800 ℃ temperature range for 60% and 80% IPCs respectively, as compared to those without an initial residual stress. Therefore, for clarity, the FE analysis results shown in Figure 29 and Figure 30 are for the cases considering initial thermal residual stress only.

It is shown in Figure 29 that the curve of FE predictions is lower than the measured one and mostly close to the Kerner-Schapery lower bound for 60% IPC. The FE analysis results of 80% IPC are relatively closer to the experimental data and in general lies in between the Kerner-Schapery bounds. This can be understood by the fact that the Kerner-Schapery bounds are for elastic composites, and upon reheating from room temperature the FE models of 3D RVEs are unloaded from their initial residual stress state, and are therefore eventually in a relatively elastic state. Same reason that the cases neglecting initial thermal residual stress have higher CTE values. The expansion of

the constituent phases would be relatively unconstrained if the composite is under a plastic state. The discrepancy between the FE-predicted CTEs and the measured values can be attributed to experimental uncertainty. According to [21], experimental error, the presence of the second tin-rich sub phase in the bronze, the presence of diffused iron in the bronze, and slight differences between the bronze alloys tested and present as an infiltrant in the composite can be the sources of uncertainty and they are not considered in any of the models discussed here.

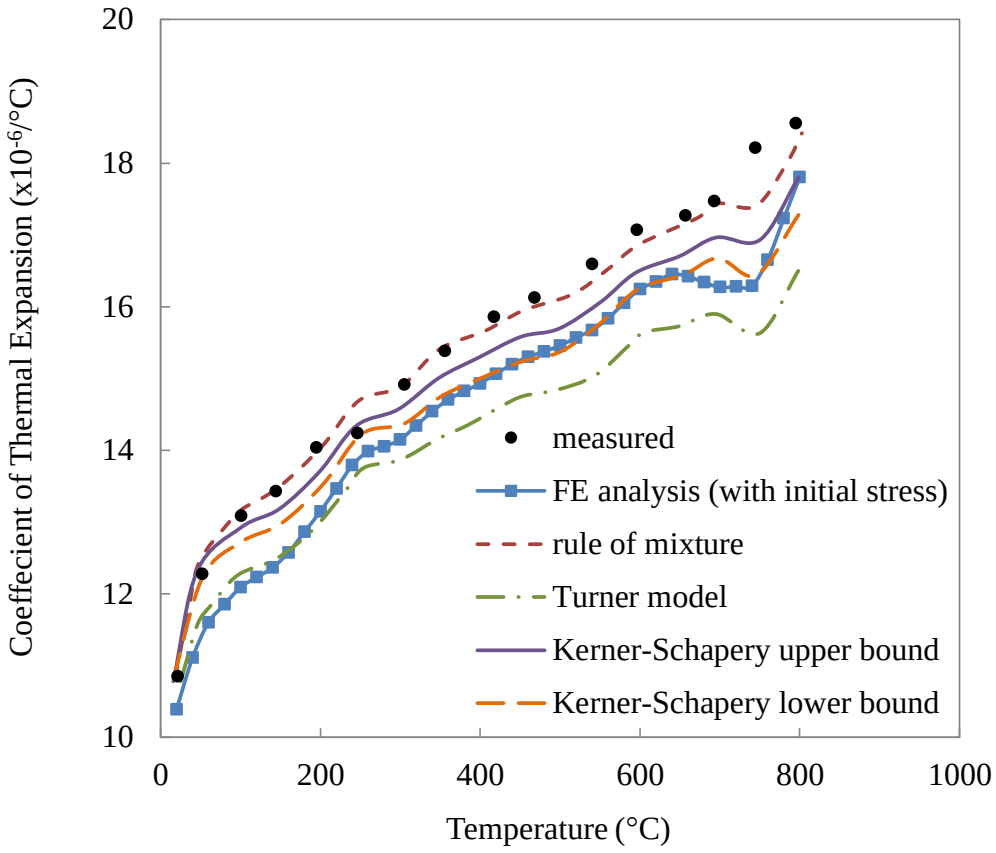

Figure 29: Instantaneous coefficient of thermal expansion vs. temperature for 60% IPC.

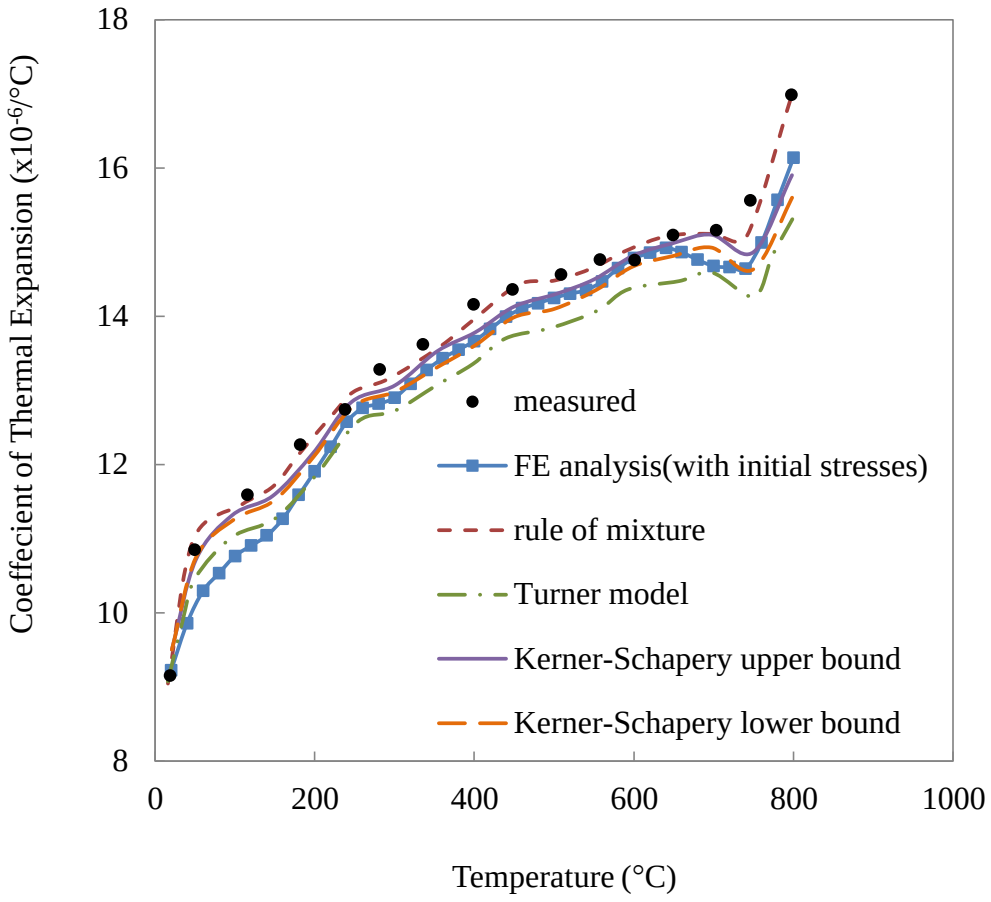

Figure 30: Instantaneous coefficient of thermal expansion vs. temperature for 80% IPC.

3.3.4 Damage evolution

One microstructural feature of the IPCs is the presence of voids within the bronze phase, especially for 80% IPC [21]. Some of these voids are located along the phase interfaces. Although these voids have no effect on thermal expansion properties of the IPCs, they exert great influence on the damage evolution of IPCs. Since both stainless-steel and bronze phases are ductile metals and void growth and nucleation at the phase

interface on the microstructural scale is assumed to be the failure mechanism for the composite, the Gurson-Tvergaard-Needleman (GTN) constitutive model is adopted here to study the damage evolution in the given IPCs.

As mentioned before, $\sigma_y\left(\bar{\varepsilon}_m^{pl}\right)$ used in the yield condition, Eq. (3.1), in the GTN model is the yield stress of the fully dense matrix material. For the given IPCs, the fully dense matrix material should be state as "fully dense hybrid matrix material," since it refers to undamaged stainless-steel/bronze IPCs. In other words, we need to obtain $\sigma_y\left(\bar{\varepsilon}_m^{pl}\right)$ from undamaged IPCs. These data then can be incorporated in the GTN model to study the damage effect due to voids. Therefore, in this study, a two-step procedure is used to study the damage evolution of IPCs:

(1) Elastoplastic FE analyses of undamaged IPCs using the FE models of 3D RVEs are conducted under uniaxial tension to obtain the effective stress-strain curves of undamaged IPCs. The von Mises plasticity theory and isotropic hardening are adopted for these analyses. Again, the temperature dependent material properties used are from [21], and are given in Figure 23, Figure 28 and Table 4. Then the relation between σ_y and $\bar{\varepsilon}_m^{pl}$ are extracted from the obtained stress-strain curves. Also, thermal residual stress due to the cooling process which is obtained from the undamaged IPCs can be incorporated as the initial stress condition.

(2) σ_y values as function of $\bar{\varepsilon}_m^{pl}$ obtained from the undamaged IPC FE models of 3D RVEs are used as the fully dense hybrid matrix material properties in the GTN constitutive model to study the elastoplastic behavior and damage evolution of the IPCs

with voids under uniaxial tension. For evaluation, a single 3D element representing the effective media of the IPCs is tested for uniaxial tension.

Regarding the material parameters of GTN constitutive model: The value of the initial volume fraction of voids f_{ini} for 60% and 80% IPC used here are those from [21]. Since the microstructures of the 60% and 80% IPCs are different, q_1 and q_2 are taken different values for these two IPCs. The ranges of q_1 and q_2 are referred to those from [123]. Also, different values of the mean strain for nucleation ε_N in Eq. (3.8) are used because of the big difference in failure strain between the 60% and 80% IPCs. Since 80% IPC has larger volume fraction of steel phase with weak bonding between the phases and fails at a much smaller strain than 60% IPC, it is assumed that f_N of 80% IPC is greater than that of 60% IPC. The values of the GTN model parameters that are used to adjust the numerical calculation to fit the measured effective strain-stress curves of 60% and 80% IPCs from [21] are listed in Table 5.

Table 5: Material parameters for the Gurson-Tvergaard-Needleman constitutive model.

Material	q_1	q_2	f_{ini}	ε_N	s_N	f_N
60% IPC	1.50	1.00	1.0%	0.015	0.05	0.2
80% IPC	2.00	1.25	1.5%	0.005	0.05	0.7

Tensile stress-strain curves are obtained from the FE models of 3D RVEs for the cases without damage and with/without initial thermal residual stress, as well as from single element evaluation of GTN model for the case considering both initial thermal residual stress and damage evolution. Their comparisons with experimental data from [21] are plotted in Figure 31 and Figure 32 for 60% and 80% IPCs, respectively.

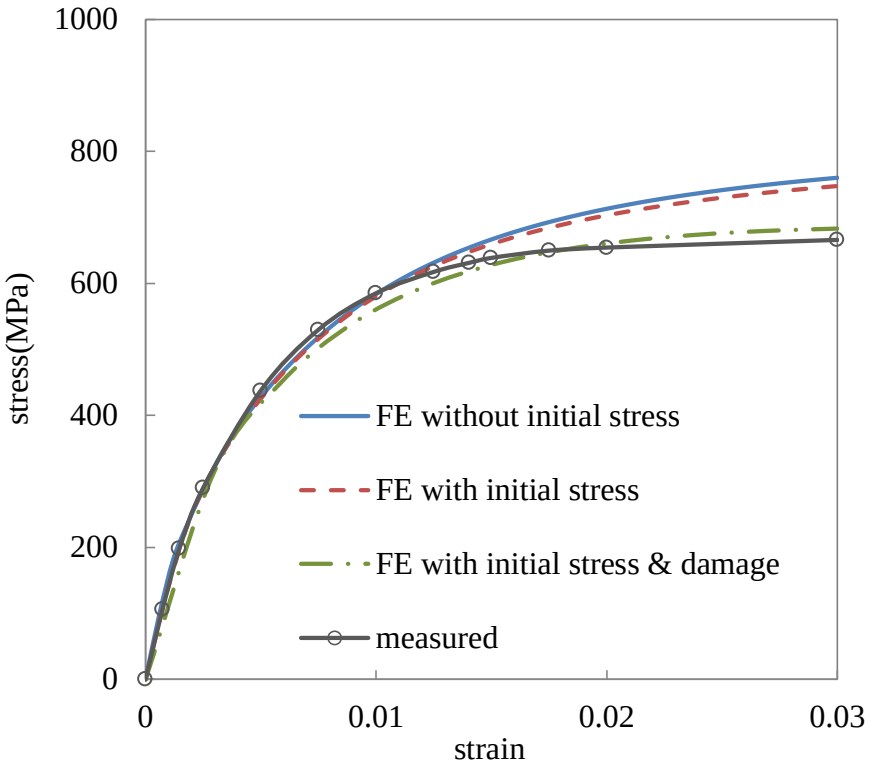

Figure 31: Tensile behavior of 3D RVE FE model of 60% IPC.

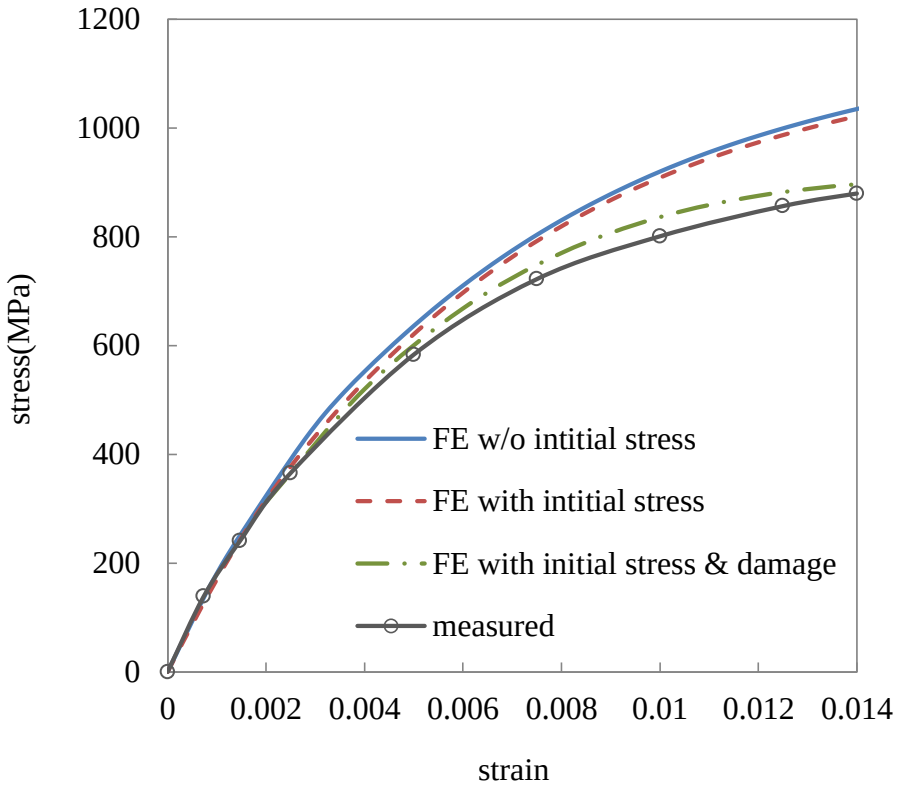

Figure 32: Tensile behavior of 3D RVE FE model of 80% IPC.

For 60% IPC under uniaxial tension, by comparing the stress-strain curves of FE analysis results without considering initial thermal residual stress nor damage with the experimental results, it can be noticed that the FE analysis result has stress values 14% higher than those of experimental results at failure stain around 3%, as seen in Figure 31. Further, by considering initial thermal residual stress, the reduction of average modulus in the bronze leads to a reduction of the modulus of the 60% IPC as a whole, and the stress value at failure strain is now 12.6% higher than the experimental measurement.

It is shown in Figure 32 that the stress-strain curves for those different cases of FE analysis results for the 80% IPC, in general, have similar trend to the 60% IPC. Without considering initial thermal residual stress, the FE analysis result shows 17.6% higher stress than the experimental data at failure strain 1.4%, while with initial thermal residual stress, the resultant stress of the FE analysis is 15.7% higher than the experimental results at failure strain. Therefore, it can be concluded that initial thermal residual stress only has slight influence on the elastoplastic behavior of the undamaged IPCs. Also, the initial thermal residual stress cannot explain an important fact that the given interpenetrating phase composites fail at much lower tensile strain than either of the constituent material ultimate strains. Moreover, even though the 80% IPC has more volume fraction of the stronger phase (stainless-steel), it fails at only half of the tensile strain that 60% IPC can sustain. The failure mechanism of the IPC is forming on the microstructure scale, rather than on the specimen scale [21]. Therefore, GTN constitutive model is adopted to include damage effect of the voids located within bronze and at the interface of the two phases.

It is shown in Figure 31 and Figure 32 that by considering damage evolution, the numerical results of GTN constitutive model can be very close to the experimental results than the other two cases without damage evolution. For 60% IPC, the stress obtained from GTN model is 2.6% higher than the experimental results at 3% strain, while the numerical results has nearly the same stress value at the failure stain as the experimental data for 80% IPC.

The predicted results of total void volume fraction and its components void growth and nucleation volume fractions versus the total strain for the simulated 60% IPC and 80% IPC are plotted in Figure 33 and Figure 34, respectively. As listed in Table 5, the initial void volume fractions, f_{ini}, for 60% and 80% IPCs are 1% and 1.5%, respectively. Further, it is shown that void growth only contributes very small part (around 2%) to the overall change of void volume fraction for both 60% and 80% IPCs. In contrast, void nucleation plays a more important role in the damage evolution. As mentioned before, void nucleation occurs mainly at the second-phase particles by decohesion of the matrix-particle interface or by fracture of the particles. For the given IPCs, since the particle phase is made of stainless-steel which is very ductile and much stiffer than the bronze matrix, it can be predicted that the newly nucleated voids are mainly caused by decohesion of the particle-matrix interfaces. Also, it is noticed that 80% IPC fails at a much smaller strain level than 60% IPC. One of the reasons is that more void volume fraction is concentrated within the bronze matrix in 80% IPC (7.5% in bronze voids, and 1.5% in total) compared to that of 60% IPC (0.25% in bronze voids, and 1% in total). A more important reason for this phenomenon is that the 80% IPC has much greater volume fraction of stainless-steel phase which leads to the decohesion of considerable part of the weak particle-matrix interface bonding.

In Figure 33 and Figure 34, it is shown that 60% IPC fails when the total void volume fraction is around 5%, while that value for 80% IPC is about 6%. Upon damage initiation, the composites start to lose the load carrying capability rapidly, which accompanies with void coalescence. GTN constitutive model can model void

coalescence use porous failure criterion. However, there is no information in the literature regarding initiation of cracking or any experimental coalescence results for the given interpenetrating phase composites except for experimental nominal stress-nominal strain curves. Therefore, final material failure by void coalescence is not addressed in this study. Moreover, the above mentioned total void volume fraction 5% and 6% at failure for 60% and 80% IPCs, respectively, are only approximations at which the IPCs start to lose the capacity to carry more load.

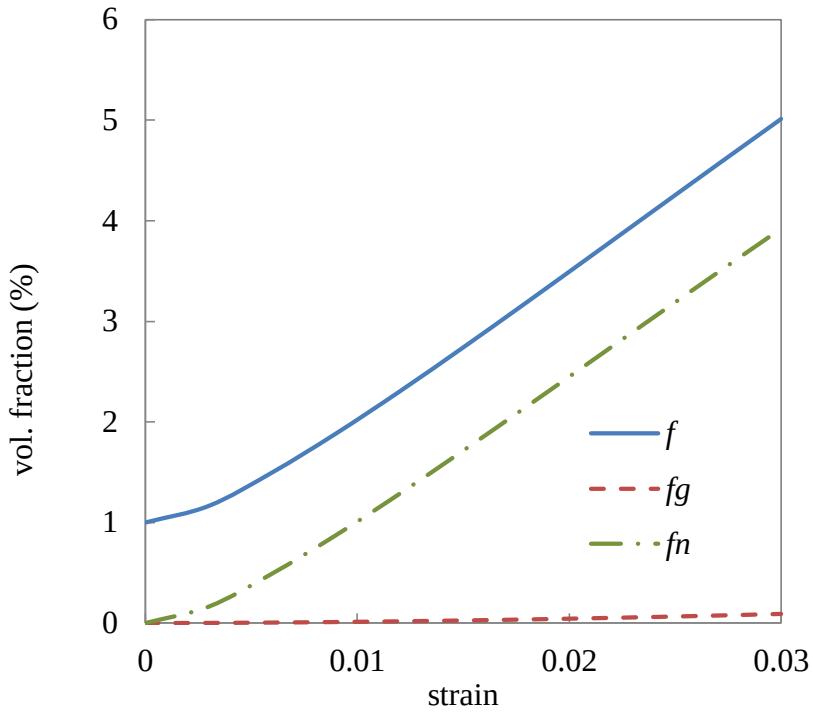

Figure 33: Void growth and nucleation vs. strain for 3D RVE FE model of 60% IPC.

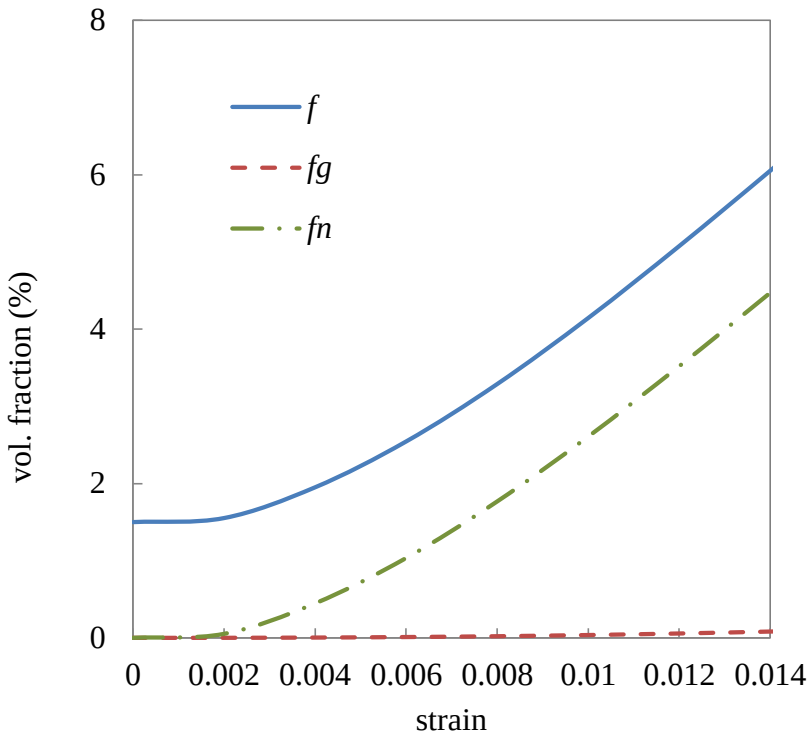

Figure 34: Void growth and nucleation vs. strain for 3D RVE FE model of 80% IPC.

CHAPTER IV

COMPUTATIONAL MODELING OF TEMPERATURE-DEPENDENT THERMAL PROPERTIES OF A SHAPE MEMORY ALLOY (SMA)/MAX PHASE INTERPENETRATING PHASE COMPOSITES WITH POROSITY

In this study, micromechanics based RVE method and finite element method is adopted to predict the effective thermal conductivity of NiTi/Ti_3SiC_2 interpenetrating phase composite fabricated using spark plasma sintering (SPS) technique. The phase composition of the composite is from experimental data: 16.3 vol. % pores located in Ti_3SiC_2 phase and about 1/1 volume ratio for Ti_3SiC_2 phase and NiTi phase. Besides porosity, the presence of the reaction interfacial layer between Ti_3SiC_2 phase and NiTi phase in the composite [124] is considered. Two 3D RVEs, i.e. one considering only porosity and the other taking both porosity and interface into account, are created to investigate the influence of interfaces on effective thermal conductivity.

4.1 Microstructural characteristics of the NiTi/Ti_3SiC_2 composite

Porosity with volume fraction of -16 % was observed in the Ti_3SiC_2 phase due to incomplete sintering at 960 ^oC which is well below the sintering temperature of Ti_3SiC_2 but close to the melting temperature of NiTi [124]. Therefore, porosity is located within Ti_3SiC_2 phase, while NiTi and the two-phase interface are pore-free. A lot of these pores are interconnected according to the morphology observations. In order to realistically reflect the microstructure of the NiTi/Ti_3SiC_2 composite, pores located within Ti_3SiC_2

phase are explicitly included in the 3D RVEs in spite the difficulties in creating such complex geometries and generating mesh in the corresponding FE models later. In the following numerical analysis, the pores are assumed to be occupied by air.

Interfacial layer between Ti_3SiC_2 phase and NiTi phase is another feature of the microstructure of the NiTi/Ti_3SiC_2 composite. The thickness of the interfacial layer is in the scale of one micron, and thus 1μm is assumed as the thickness of all interfacial layers throughout the composite in this study [124]. Electron backscatter diffraction (EBSD) was used to identify the phase composition in the interfacial layer, and $NiTi_2$, TiC and Ti_5Si_3 were found as the main phases [124]. Since it is very difficult to accurately measure the volume fraction of these phases, the overall effective thermal conductivity of the interfacial layer is assumed to vary linearly with temperature. Also, these new phases in the interfacial layer are assumed to be perfectly bounded with the adjoining Ti_3SiC_2 and NiTi phases. In fact, heat scattering at constituent interfaces due to the differences in vibration properties of dissimilar materials is known as interfacial thermal resistance (or Kapitza resistance) [125]. The interfacial layer plays an important role in heat transport in the NiTi/Ti_3SiC_2 interpenetrating phase composite because of the complex new phase boundaries formed in interfacial layer. Therefore, the influence of interfacial layer, besides porosity, on the effective thermal conductivity of the NiTi/Ti_3SiC_2 composite is investigated.

4.2 3D representative volume element (RVE)

Two 3D RVEs are generated based on the micrographs of NiTi/Ti_3SiC_2 composites [22] using the technique developed in the previous chapter, i.e. configurations A and B as shown in Figure 35.

Configuration A considers only porosity in addition to the two constitutive phases, whereas configuration B contains both porosity and interfaces, as shown in Figure 35 (a) and (b), respectively. The generation of 3D RVE for configuration A consists of two steps: (i) NiTi particles are randomly placed inside a cubic and rest part of the cubic is the Ti_3SiC_2 matrix phase. (ii) The pores are randomly located within Ti_3SiC_2 matrix phase. The connectivity of the NiTi particles and pores in step (i) and (ii) is controlled by adjusting the range of distance among their centroids. Meanwhile, the desired volume fraction of these two phases can be achieved by varying the number of particles/pores. For configuration B, a third step is needed to create interfacial layer: (iii) Interfacial layer is carved out of one or both of NiTi phase and Ti_3SiC_2 matrix phase along the surface contour, while the volume fraction of the interface phase is controlled by adjusting the thickness of this layer. The dimensions of both 3D RVEs are 200μm × 200μm × 200μm, which is found to be the size that can include enough volume fractions of randomly distributed interconnected NiTi as well as interconnected pores, and be statistically homogeneous to represent local continuum properties of the given composite.

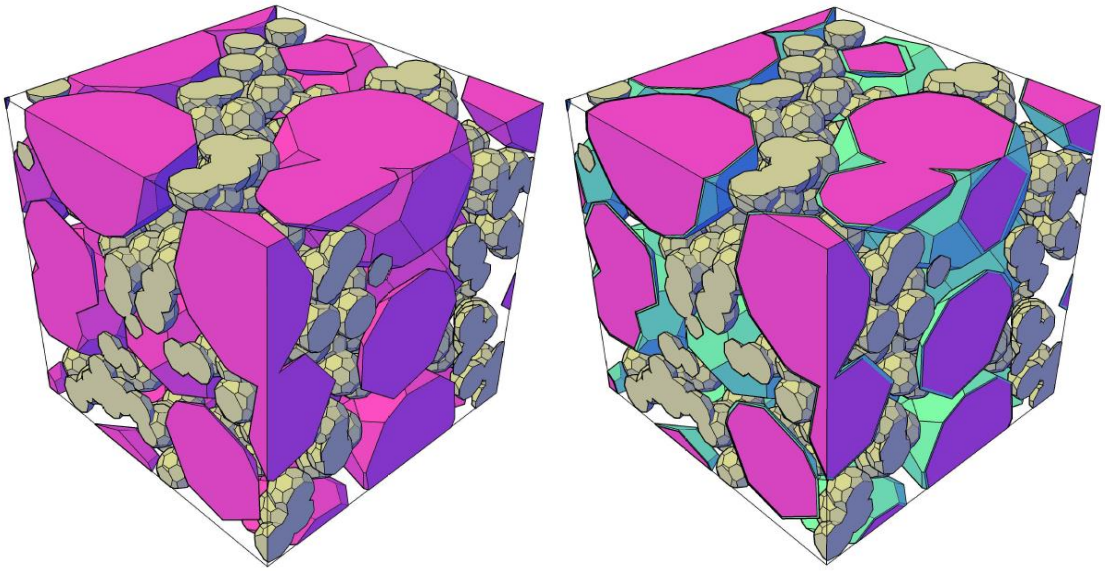

(a) (b)

Figure 35: 3D RVEs of the NiTi/Ti_3SiC_2 composite: (a) in configuration A, grey represents pore, pink NiTi, and transparent Ti_3SiC_2; (b) in configuration B, grey represents pore, pink NiTi, transparent Ti_3SiC_2, and cyan interface.

Simplified geometries, such as limited number of spherical shape particles and three-dimensional crosses, have been used to represent the microstructure of IPCs [9, 21, 59]. However, the three-dimensional crosses cannot reflect the shape of the particle with the fact that the actual cross section of the NiTi particles in the composite is not perfect circle in 2-D. Therefore, again, truncated icosahedron (soccer ball shape) instead of a sphere is adopted to represent the shape of NiTi particles in order to reflect the irregularity of the outer surface of the interconnected particle phase. Another advantage of using truncated icosahedron shape particles is that it can greatly reduce the element number in the mesh of corresponding FE model. Since it is difficult to describe the size

of a truncated icosahedron, the radiuses of the corresponding circumscribed spheres of the truncated icosahedron are used to represent the size of the NiTi particle and voids. And two different sizes for NiTi particles and one size for voids are used in creating 3D RVEs. The sizes of NiTi particles are 50μm and 40μm in radius, whereas the radius of the pores is 12μm. Each 3D RVE consists of around 33 NiTi particles and 268 pores.

It is assumed that the all the consistent phases in the NiTi/Ti_3SiC_2 composite are perfectly bonded. Table 6 lists the volume fractions of each phase that are calculated from the two configurations of 3D RVEs.

Table 6: Volume fractions of four components, namely Ti3SiC2, NiTi, pore, and interface, in the NiTi/Ti3SiC2 composites.

Component	Volume fraction, %	
	Configuration A	Configuration B
Ti_3SiC_2	40.5	40.5
NiTi	43.2	40.5
Pore	16.3	16.3
Interface	N/A	2.7

4.3 Finite element models

Due to the complex geometry of the 3D RVEs, they are represented with DC3D10 element mesh (diffusive ten-node quadratic tetrahedral element) in the commercial software Abaqus which are geometrically versatile and are very convenient

to automatically mesh a complex shape. The FE meshes for the two 3D RVE configurations are shown in Figure 36. The FE model for the configuration A contains 633,718 elements, whereas the one for the configuration B contains 452,552 elements. For boundary conditions, temperature gradient of -1 K/μm is applied along x-, y-, and z-directions to obtain the effective thermal conductivity in the corresponding directions.

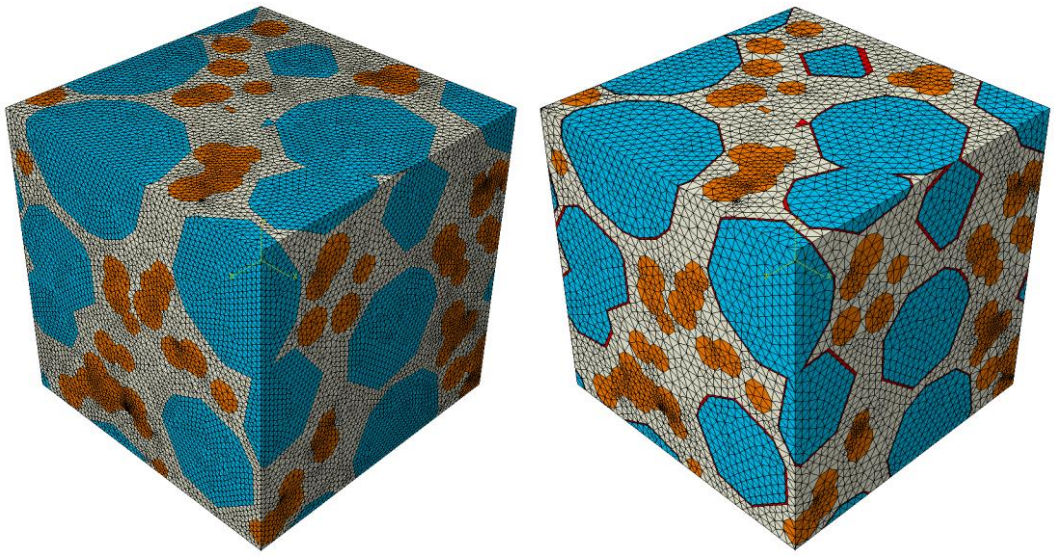

(a) (b)

Figure 36: FE meshes on 3D RVEs of two configurations: (a) in configuration A, orange represents pore, blue NiTi, and white Ti3SiC2; (b) in configuration B, orange represents pore, blue NiTi, and white Ti3SiC2, and red interface.

A steady state heat transfer problem is solved to obtain the effective thermal conductivity of the composite. For one dimension form, the Fourier's Law is simplified to

$$q_x = -k_x \frac{dT}{dx} \tag{4.1}$$

Therefore, the effective heat conductivity of the composite can be derived using the following equation

$$k_x = -q_x \Big/ \frac{\Delta T}{\Delta x} \tag{4.2}$$

For both configurations A and B, the experimental results of temperature dependent thermal conductivities for Ti_3SiC_2 and NiTi shown in Figure 37 [22] are used as input data in the FE modeling. The thermal conductivity in the 340-400 K temperature range is not considered due to the M→A reverse transformation of NiTi. As for configuration B, with the reaction interfaces treated as one phase, the thermal conductivity of this phase is assumed as a certain value to fit with the experimental results of the composite in Figure 37. Therefore, we neglect this part in the "thermal conductivity versus temperature" curve.

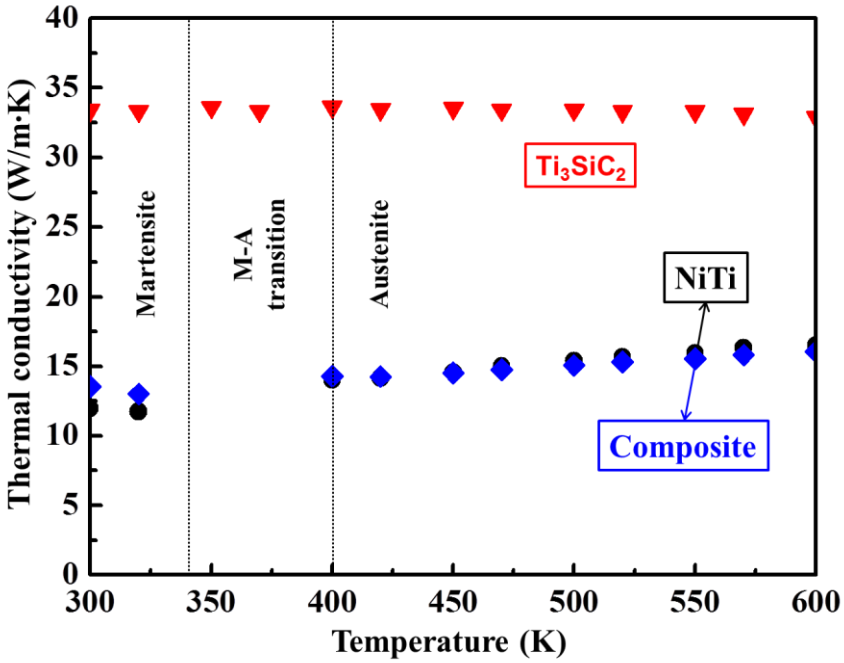

Figure 37: Temperature dependencies of thermal conductivity upon heating in 300-600 K temperature range for the NiTi/Ti_3SiC_2 composite, and monolithic NiTi and Ti_3SiC_2 [22].

4.4 Thermal conductivity: comparison between numerical results and experimental data

The obtained effective thermal conductivities in different directions for the two configurations, i.e. configuration A considering only porosity and configuration B considering both the porosity and the interfaces, are listed in Table 7. It is shown that for configuration A, the maximum difference among k_x, k_y, and k_z for various temperatures is 1.08%, while the corresponding value for configuration B is 0.9%. It suggests that for both configurations, the effective thermal conductivities are approximately isotropic, i.e. thermal conductivity being independent of temperature gradient direction. In other words,

for the steady state heat transfer problem, the corresponding two 3D RVEs achieve approximate isotropy, and furthermore they are statistically homogeneous and can represent the local continuum properties of the $NiTi/Ti_3SiC_2$ composite.

Table 7: FE results of temperature-dependent thermal conductivity along different temperature-gradient directions, i.e. *x*, *y*, and *z*.

Temperature (K)	Thermal conductivity (W/m·K)							
	Configuration A				Configuration B			
	k_x	k_y	k_z	Standard deviation	k_x	k_y	k_z	Standard deviation
300	16.17	16.11	16.26	0.08	13.83	13.84	13.93	0.06
320	16.03	15.97	16.12	0.08	13.96	13.97	14.06	0.06
450	17.46	17.37	17.54	0.09	15.69	15.66	15.78	0.06
500	17.8	17.71	17.89	0.09	16.12	16.08	16.21	0.07
550	18.04	17.93	18.12	0.10	16.44	16.39	16.53	0.07
600	18.15	18.04	18.23	0.10	16.63	16.58	16.72	0.07

Figure 38 shows the comparison between simulation with experimental results for the two configurations, where the simulation results are the average of k_x, k_y, and k_z. For configuration A, the simulation overestimates the effective thermal conductivity by 9.2-19.1% as compared to the measured data. The discrepancy between the measured data and the modeling predictions indicates that the presence of interfacial layer, besides porosity, may play an important role in heat transport. However, it is not easy to include

the interfacial layer into the model due to limited information on the volume fractions of the new phases in the interfacial area, as well as the interfacial thermal conductance across the multiple phase boundaries. One way to gain insight of the effect of this layer is to solve an inverse problem: matching the modeling data with measured data assuming the interfaces as one phase with a certain thermal conductivity value.

For the FE model of configuration B, parameter study on the effective thermal conductivity of interfacial layer is conducted to fit numerical results with experimental data in a reasonable range. In result, the effective thermal conductivity is assumed to vary linearly from 0.4-1.6 W/m·K with temperature increasing from 300 to 620K, which is about one order of magnitude lower than that of the pure Ti_3SiC_2 and pure NiTi. Figure 38 shows a good agreement between the measured data and the FE results [22]. The difference between these two sets of data is from 2.5-8.9 %, which is much lower than the corresponding value in the case where only porosity is considered.

Another observation from numerical results for both configurations is that the discrepancy between FE results and experimental results becomes smaller and smaller as the temperature moves further away from the M→A phase transformation temperature range. For example, in Figure 38, the difference is about 8.2% at temperature, 450 K, close to phase transformation temperature, and then this difference drops to 2.5% and 3.8% at 300K and 600 K, respectively. There are two possible explanations for this phenomenal: (1) the measured data close to the M→A phase transformation temperature range is not as accurate as those with temperature away from it, due to the latent heat generated during M→A phase transformation; (2) instead of linear variation of the

overall effective thermal conductivity of interfacial layer with temperature, other assumption such as power law might be used.

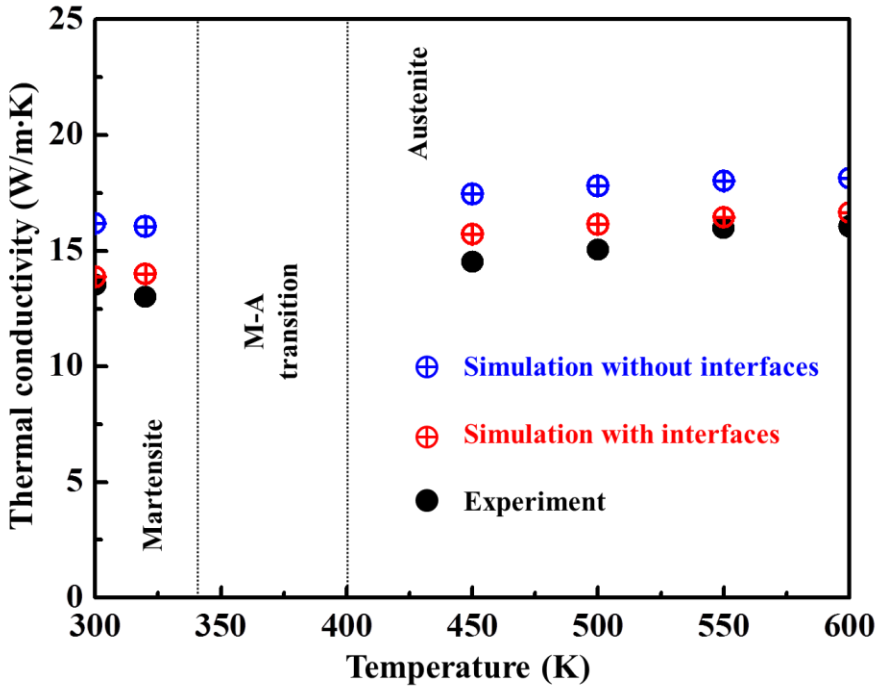

Figure 38: Temperature-dependent thermal conductivity of the NiTi/Ti_3SiC_2 composite: comparison between experiment and simulation results. Simulations results based on both configuration A and B are shown [22].

4.5 Heat flux: numerical results

Figure 39 shows typical examples of heat flux distribution in each phase of the these two different configurations when temperature is around 600 K and temaperatue gradient is applied in the *y*-direction. According to the length scale used in this sudy, the unit of heat flux used here is 10^{-6} W/μm^2.

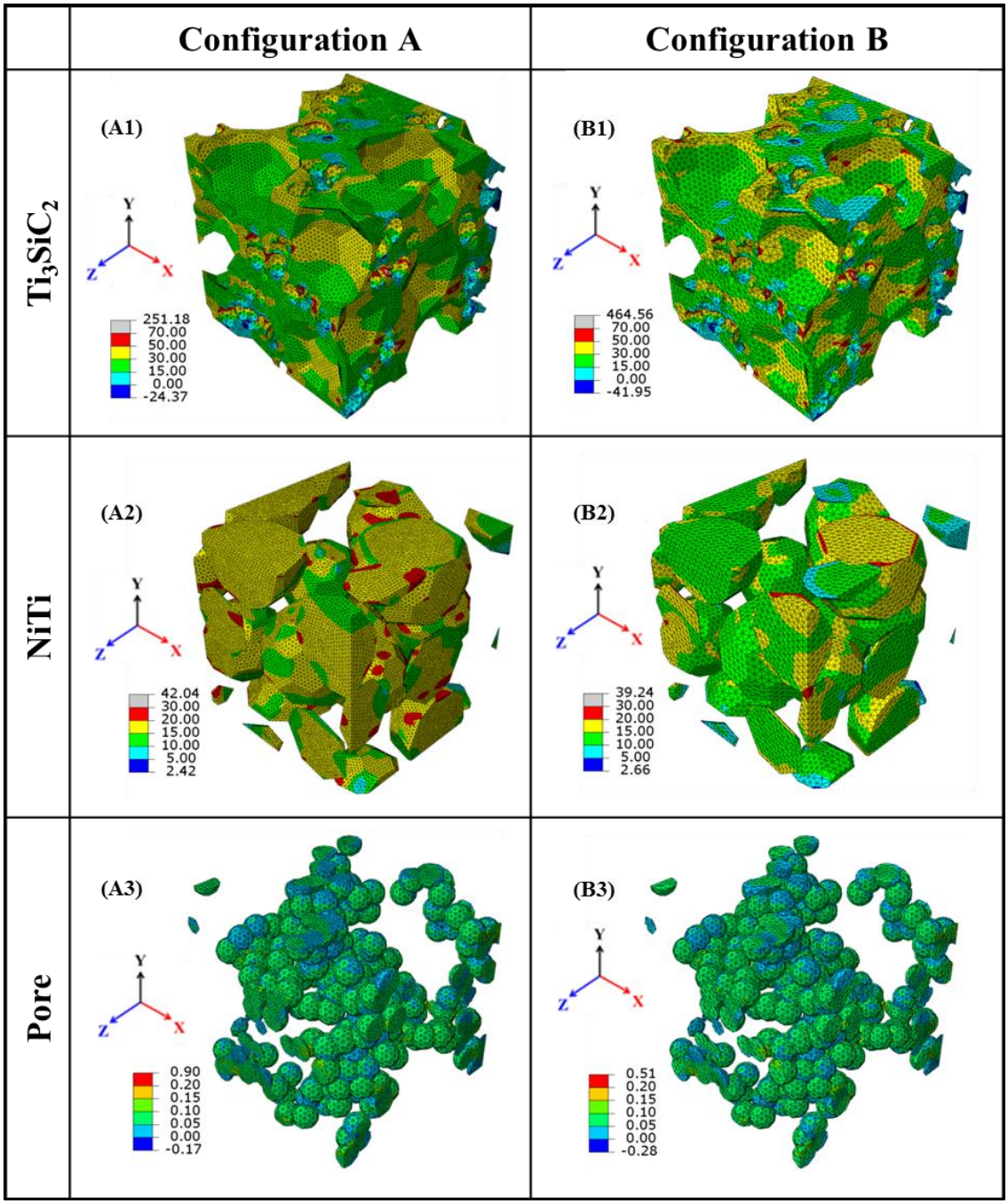

Figure 39: Simulated heat flux (unit: 10^{-6} W/μm^2) along *y* direction for four components, namely Ti_3SiC_2, NiTi, pore, and interface, in the NiTi/Ti_3SiC_2 composite under two different configurations: A and B.

	Configuration A	Configuration B
Interface	N/A	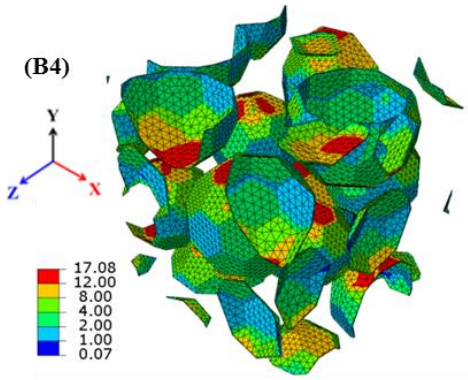

Figure 39: Continued.

For configuration A in which only porosity is considered, it is shown in Figure 39(A1) that Ti_3SiC_2 has the highest level of heat flux in the composite. The main part of Ti_3SiC_2 phase has heat flux values in the range of 30-50 (10^{-6} W/μm^2). Some parts of Ti_3SiC_2 phase adjacent to NiTi phase have lower heat flux values in the range of 15-30 (10^{-6} W/μm^2). Also, there are some small heat-concentration areas which are located at the immediate vicinity of pores in Ti_3SiC_2 phase. This can be understood by the fact that when heat flows from Ti_3SiC_2 phase to pores which are occupied by air, which has a dramatically lower thermal conductivity, heat will accumulate locally in those areas and form some "hot spots". In Figure 39(A2), it can be seen that heat flux distributed relatively uniform in NiTi phase, with the values in the range of 15-20 (10^{-6} W/μm^2). Pores have the lowest level of heat flux 0-0.15 (10^{-6} W/μm^2), as shown in Figure 39 (A3).

To see the influence of the interfacial layer upon heat flow in the composite, the distributions of heat flux along temperature gradient direction in each phase of configuration B considering both porosity and interfacial layer are plotted in Figure 39

(B1)-(B4). Heat flux distribution in Ti_3SiC_2 phase is very similar to that of the configuration A, as seen in Figure 39(A1) and 6(B1), but some slight differences for the two configurations can be observed. One is that the part with the heat flux value 30-50 (10^{-6} W/μm^2) shrinked slightly as compared to Figure 39(A1). Another difference is location of "hot spot". They not only locate in the areas adjacent to pores, but also some areas adjacent to the interfacial layer. This follows that the effective thermal conductivity of the interfacial layer is much lower than that of pure Ti_3SiC_2. The heat flux values of NiTi phase in configuration B is lower than that of configuration A and mainly in the range of 10-15 (10^{-6} W/μm^2) due to the heat scattering at the surrounding phase boundaries, as shown in Figure 39(B2). As expected, the interface has low heat flux value, mostly in the range of 1-10 (10^{-6} W/μm^2), as shown Figure 39(B4). Once again, the pores have the lowest heat flux value in the composite, the value and distribution, as shown in Figure 39(B3), are similar to that of configuration A. An overall comparison between these two configurations indicates that the heat scattering at the interfacial layer results in an overall reduction of heat flow within the composite, especially in NiTi phase.

Another advantage of the FE model is that we can explore the heat path in the NiTi/Ti_3SiC_2 interpenetrating phase composite by plotting the iso-surface of the heat flux along temperature gradient direction in the composite, which cannot be measured or observed in the experiments. First, the wireframe of mesh is plotted to show the geometry of the interested phases. Then 3D iso-surfaces of different level heat flux are drawn in the mesh wireframe to show the heat path in each phase, see in Figure 40.

The iso-surfaces of heat flux in Ti_3SiC_2 phase for the two configurations are very similar, as shown in Figure 40 (A1) and (B1). The iso-surfaces (yellow color) with heat flux value around 30×10^{-6} W/μm^2 has broad distributions within Ti_3SiC_2 phase. Their connected parts can be seen as the "heat path" where heat can transfer efficiently. Also we can see the distribution of "hot spots" more clearly in the 3D wireframe mesh.

Figure 40 (A2) and (B2) also show the plots of iso-surfaces of heat flux in NiTi for the two configurations. Although the locations with high heat flux level in NiTi for the two configurations are alike, there is apparently a drop in heat flux value for the configuration B considering interfacial layer as compared to configuration A.

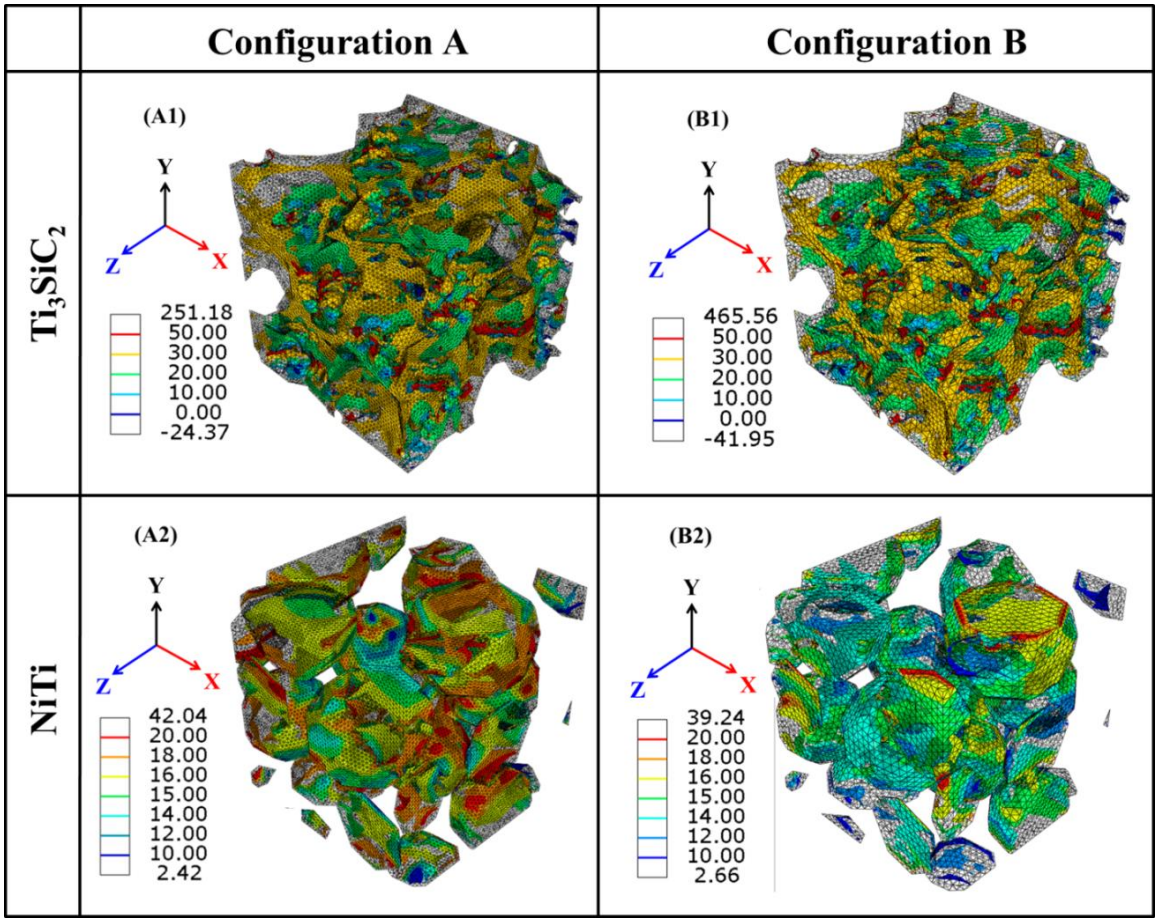

Figure 40: Iso-surface of the heat flux (unit: 10^{-6} W/μm^2) along *y* direction for Ti_3SiC_2 and NiTi in the NiTi/Ti_3SiC_2 composite under two different configurations: A and B.

CHAPTER V

COMPUTATIONAL MODELING OF PLASTIC-DAMAGE BEHAVIOR OF POROUS MAX PHASE

In this chapter, the mechanical properties of porous Ti_2AlC which is one of the materials from MAX phase with controlled porosity and pore size is studied. Micromechanics based representative element volume (RVE) method and finite element (FE) method is adopted in modeling porous Ti_2AlC. Effective elastic moduli and compressive strength are obtained from FE analyses. A plasticity-damage coupled constitutive model which considers different tensile and compressive mechanical behavior is used in modeling the inelastic behavior of porous Ti_2AlC. Numerical results show that volume fraction, size and shape of pores have influence on elastic moduli and compressive strength of the material.

5.1 Constitutive model

The crystalline defects in Ti_2AlC are basal plane dislocations, which are large in amount, multiply and are mobile even low temperature (as low as 77K). Therefore, the ductility of Ti_2AlC is in between of typical ceramic and metal. The formation of kink bands (KB) under loading plays a central role in deformation of Ti_2AlC, which also results in the distinct tensile and compressive behaviors (i.e. Ti_2AlC is more brittle in tension than in compression at room temperature) [104]. Therefore, a plastic-damage

constitutive module that can to capture the distinct tensile and compressive behavior of a quasi-brittle material system should be used.

In this study, a coupled plasticity-damage constitutive model formulated by Cicekli et al. [105] and modified by Abu Al-Rub and Kim [116] is used in this study. In this constitutive model, the Lubliner yield criterion [114] expressed in the effective (undamaged) configuration is adopted to predict the plastic behavior of porous Ti_2AlC. Furthermore, the non-associative plasticity flow rule based on the Drucker–Prager potential and power law damage evolution functions with two distinct damage evolution surfaces: tensile and compressive damage surfaces are included in this constitutive model.

5.1.1 Isotropic damage model

The definition of the damage density φ based on the effective (undamaged) area first proposed by Kachanov [126] is adopted here. In the nominal (damaged) configuration, all types of damages results from loading, such as voids, cracks and debonding, etc. are included and the damage density φ is defined by the ratio of the total damaged area to overall cross-section area:

$$\varphi = \frac{A - \bar{A}}{A} = \frac{A^D}{A} \tag{5.1}$$

The value of φ ranges from 0 to 1. Material is considered as undamaged when φ equals to 0 and fully damaged when φ equals to 1.

For the isotropic damage (i.e. scalar damage variable), the relation between the stresses in damaged and undamaged configurations, namely nominal Cauchy stress tensor σ_{ij} and the corresponding effective stress tensor $\bar{\sigma}_{ij}$ is nonlinear argued by Cicekli et al. [105]. Here, the effective stress means the average micro-level stress acting in the undamaged (intact) material under uniaxial loading, i.e. force divided by the undamaged part of the area, while the nominal stress means the macro-level stress and is defined as the force divided by the total area. In order to predict the nonlinear dependence of degradation of the damaged stiffness on damage density, a nonlinear relationship between the nominal and the effective stress tensor is assumed,

$$\sigma_{ij} = \left(1-\varphi\right)^2 \bar{\sigma}_{ij} \tag{5.2}$$

For simplicity and ease in the numerical implementation, strain equivalence hypothesis [127] is adopted in this study to derive the transformation relations between the damaged and the hypothetical undamaged states of the material. The total strain tensor ε_{ij} is set equal to the corresponding effective strain tensor $\bar{\varepsilon}_{ij}$ (i.e., $\varepsilon_{ij} = \bar{\varepsilon}_{ij}$), which can be decomposed into elastic strain $\varepsilon_{ij}^e \left(= \bar{\varepsilon}_{ij}^e\right)$ part and plastic strain $\varepsilon_{ij}^p \left(= \bar{\varepsilon}_{ij}^p\right)$ part, such that:

$$\varepsilon_{ij} = \varepsilon_{ij}^e + \varepsilon_{ij}^p = \bar{\varepsilon}_{ij}^e + \bar{\varepsilon}_{ij}^p = \bar{\varepsilon}_{ij} \tag{5.3}$$

The plastic strain in the above equation incorporates all types of irreversible deformations whether they are due to the formation of KB, delamination within grains, or shear-band formation, etc.

Following generalized Hooke's law,

$$\sigma_{ij} = E_{ijkl}\varepsilon^{e}_{kl}, \quad \bar{\sigma}_{ij} = \bar{E}_{ijkl}\varepsilon^{e}_{kl} \tag{5.4}$$

The elasticity tensor for isotropic linear-elastic material in effective configuration can be expressed as,

$$\bar{E}_{ijkl} = 2\bar{G}\delta_{ik}\delta_{jl} + \left(\bar{K} - \frac{2}{3}\bar{G}\right)\delta_{ij}\delta_{kl} \tag{5.5}$$

where $\bar{G} = \bar{E}/2(1+\bar{\nu})$ and $\bar{K} = \bar{E}/3(1-2\bar{\nu})$ are the effective shear and bulk moduli, respectively, with $\bar{E}$ being the effective Young's modulus and $\bar{\nu}$ is the effective Poisson's ratio which are obtained from the stress-strain diagram in effective configuration.

By applying the strain equivalence hypothesis, the relation between E_{ijkl} and $\bar{E}_{ijkl}$ can be expressed by:

$$E_{ijkl} = (1-\varphi)^{2}\,\bar{E}_{ijkl} \tag{5.6}$$

Due to the existence of KB and IKB in Ti_2AlC under compression, the tensile and compressive behaviors are different. Therefore, in order to model the damage behavior of porous Ti_2AlC induced by tension and compression, the Cauchy stress tensor (in the nominal and effective configurations) should be decomposed into positive and negative parts using the spectral decomposition technique [128-130]. The nominal stress tensor σ_{ij} and the effective stress tensor $\bar{\sigma}_{ij}$ can be decomposed as follows:

$$\sigma_{ij} = \sigma^{+}_{ij} + \sigma^{-}_{ij}, \quad \bar{\sigma}_{ij} = \bar{\sigma}^{+}_{ij} + \bar{\sigma}^{-}_{ij} \tag{5.7}$$

where, the superscripts "+" and "-" designate tensile and compressive entities, respectively. σ_{ij}^{+} and $\bar{\sigma}_{ij}^{+}$ are the tensile parts whereas σ_{ij}^{-} and $\bar{\sigma}_{ij}^{-}$ are the compressive parts of the stress tensors in nominal and effective configurations, respectively.

To relate the effective tensile and compressive stress tensors $\bar{\sigma}_{ij}^{+}$ and $\bar{\sigma}_{ij}^{-}$ to $\bar{\sigma}_{ij}$, fourth-order tensile and compressive projection tensors P_{ijkl}^{+} and P_{ijkl}^{-} are used:

$$\bar{\sigma}_{kl}^{+} = P_{klpq}^{+}\bar{\sigma}_{pq}, \quad \bar{\sigma}_{kl}^{-} = P_{klpq}^{-}\bar{\sigma}_{pq} \tag{5.8}$$

The tensile and compressive projection tensors are defined as follows:

$$P_{ijpq}^{+} = \sum_{k=1}^{3} H\left(\hat{\bar{\sigma}}^{(k)}\right) n_i^{(k)} n_j^{(k)} n_p^{(k)} n_q^{(k)}, \quad P_{ijpq}^{-} = I_{ijpq} - P_{ijpq}^{+} \tag{5.9}$$

where $H\left(\hat{\bar{\sigma}}^{(k)}\right)$ denotes the Heaviside step function computed at *k*th principal stress $\hat{\bar{\sigma}}^{(k)}$ of $\bar{\sigma}_{ij}$ and $n_i^{(k)}$ is the *k*th corresponding unit principal directions. In the subsequent development, the superimposed hat designates a principal value.

Substituting tensile parts and compressive parts of the nominal and effective stress tensors of Eq. (5.7) into the expression in Eq. (5.2), we have:

$$\sigma_{ij}^{+} = \left(1-\varphi^{+}\right)^{2} \bar{\sigma}_{ij}^{+}, \quad \sigma_{ij}^{-} = \left(1-\varphi^{-}\right)^{2} \bar{\sigma}_{ij}^{-} \tag{5.10}$$

where the validity of Eq. (5.2) for both tension and compression is assumed independently, φ^{+} and φ^{-} are the tensile and compressive damage densities, respectively. And therefore, the relation between σ_{ij} and $\bar{\sigma}_{ij}^{-}$ in terms of φ^{+} and φ^{-} can be written in the form:

$$\sigma_{ij} = \left(1-\varphi^{+}\right)^{2} \bar{\sigma}_{ij}^{+} + \left(1-\varphi^{-}\right)^{2} \bar{\sigma}_{ij}^{-} \tag{5.11}$$

and further,

$$\sigma_{ij} = \left[\left(1-\varphi^{+}\right)^{2} P^{+}_{ijkl} + \left(1-\varphi^{-}\right)^{2} P^{-}_{ijkl} \right] \bar{\sigma}_{kl} = M_{ijkl} \bar{\sigma}_{kl} \tag{5.12}$$

where M_{ijkl} is the fourth-order damage-effect tensor. Substitute Eq. (5.4) into Eq. (5.12), the relation of damaged elastic tensor and the corresponding undamaged elastic tensor under strain equivalence hypothesis is given as:

$$E_{ijkl} = M_{ijmn} \bar{E}_{mnkl} \tag{5.13}$$

5.1.2 Plasticity yield surface

The Lubliner yield condition which takes both tension and compression plasticity into consideration is used. Since the stress state in the effective (undamaged) configuration is the one which drives the plastic flow, the Lubliner yield criterion is expressed in the effective configuration as follows:

$$f = \sqrt{3\bar{J}_2} + \alpha \bar{I}_1 + \beta\left(\varepsilon^{+}_{eq}, \varepsilon^{-}_{eq}\right) H\left(\hat{\bar{\sigma}}_{\max}\right) \hat{\bar{\sigma}}_{\max} - \left(1-\alpha\right) c^{-}\left(\varepsilon^{-}_{eq}\right) \le 0 \tag{5.14}$$

where $\bar{J}_2 = \bar{S}_{ij}\bar{S}_{ij}/2$ is the second-invariant of the effective deviatoric stress tensor $\bar{S}_{ij} = \bar{\sigma}_{ij} - \bar{\sigma}_{kk}\delta_{ij}/3$, $\bar{I}_1 = \bar{\sigma}_{kk}$ is the first-invariant of the effective Cauchy stress tensor $\bar{\sigma}_{ij}$, $\hat{\bar{\sigma}}_{\max}$ is the maximum principal effective stress, $H\left(\hat{\bar{\sigma}}_{\max}\right)$ is the Heaviside step function ($H=1$ for $\hat{\bar{\sigma}}_{\max} > 0$ and $H=0$ for $\hat{\bar{\sigma}}_{\max} < 0$), and the parameters α and β are dimensionless material constants which are defined as:

$$\alpha = \frac{\left(f_{b0}/f_0^{-}\right)-1}{2\left(f_{b0}/f_0^{-}\right)-1}, \quad \beta = \left(1-\alpha\right)\frac{c^{-}\left(\varepsilon^{-}_{eq}\right)}{c^{+}\left(\varepsilon^{+}_{eq}\right)} - \left(1+\alpha\right) \tag{5.15}$$

where f_{b0} and f_0^- are the initial equi-biaxial and uniaxial compressive yield strengths, respectively. Empirical values for f_{b0} / f_0^- lie between 1.10 and 1.16; yielding values for α are between 0.08 and 0.12. The internal plastic state variables $\varepsilon_{eq}^+ = \int_0^t \dot{\varepsilon}_{eq}^+ dt$ and $\varepsilon_{eq}^- = \int_0^t \dot{\varepsilon}_{eq}^- dt$ are the equivalent plastic strains in tension and compression, respectively, with their rates being defined as:

$$\dot{\varepsilon}_{eq}^+ = r\left(\hat{\bar{\sigma}}_{ij}\right)\hat{\dot{\varepsilon}}_{\max}^p, \quad \dot{\varepsilon}_{eq}^- = -\left(1 - r\left(\hat{\bar{\sigma}}_{ij}\right)\right)\hat{\dot{\varepsilon}}_{\min}^p \tag{5.16}$$

where $\hat{\dot{\varepsilon}}_{\max}^p$ and $\hat{\dot{\varepsilon}}_{\min}^p$ are the maximum and minimum principal values of the plastic strain rate $\dot{\varepsilon}_{ij}^p$, such that $\hat{\dot{\varepsilon}}_1^p > \hat{\dot{\varepsilon}}_2^p > \hat{\dot{\varepsilon}}_3^p$ with $\hat{\dot{\varepsilon}}_{\max}^p = \hat{\dot{\varepsilon}}_1^p$ and $\hat{\dot{\varepsilon}}_{\min}^p = \hat{\dot{\varepsilon}}_3^p$. $r\left(\hat{\bar{\sigma}}_{ij}\right)$ is a dimensionless weighting factor which accounts for the dependence of tension or compression on the values of the principal stresses and is defined as:

$$r\left(\hat{\bar{\sigma}}_{ij}\right) = \frac{\sum_{k=1}^{3}\left\langle \hat{\bar{\sigma}}_k \right\rangle}{\sum_{k=1}^{3}\left|\hat{\bar{\sigma}}_k\right|} \tag{5.17}$$

where $\langle\ \rangle$ is the Macaulay brackets presented as $\langle x \rangle = \left(|x| + x\right)/2$. Moreover, if the loading is pure uniaxial tension $\hat{\bar{\sigma}} \geq 0$, then $r\left(\hat{\bar{\sigma}}_{ij}\right) = 1$, and if the loading is pure compression $\hat{\bar{\sigma}} \leq 0$, then $r\left(\hat{\bar{\sigma}}_{ij}\right) = 0$.

In Eq. (5.14), c^- in the last term is the isotropic hardening function, which represents the material cohesion under uniaxial compression. The evolution laws for the

compressive and tensile isotropic hardening functions c^- and c^+ are assumed to be exponential and linear hardening laws, respectively:

$$c^- = f_0^- + Q^-\left[1-\exp\left(-b^-\varepsilon_{eq}^-\right)\right], \quad c^+ = f_0^+ + h^+\varepsilon_{eq}^+ \tag{5.18}$$

where f_0^- and f_0^+ are the initial yield stresses in compression and tension, respectively. The parameters Q^-, b^- and h^+ are material constants, which can be obtained from the uniaxial stress-strain diagram in effective configuration.

A non-associative plasticity flow rule is to realistically characterize the volumetric expansion of porous Ti_2AlC. In other words, the plastic flow direction should be written in terms of a plastic potential F^p that is not equal to the plastic yield function f, such that:

$$\dot{\varepsilon}_{ij}^p = \dot{\lambda}^p \frac{\partial F^p}{\partial \bar{\sigma}_{ij}} \tag{5.19}$$

where $\dot{\lambda}^p$ is the plastic multiplier, which can be obtained from standard plasticity consistency condition, $\dot{f} = 0$, such that:

$$f \le 0,\ \dot{\lambda}^p \ge 0,\ \dot{\lambda}^p f = 0,\ \dot{\lambda}^p \dot{f} = 0 \tag{5.20}$$

The Drucker-Prager function is used as plastic potential F^p, and can be expressed as:

$$F^p = \sqrt{3\bar{J}_2} + \alpha^p \bar{I}_1 \tag{5.21}$$

where α^p is the dilation material constant. Then the plastic flow direction $\partial F^p / \partial \bar{\sigma}_{ij}$ is written as

$$\frac{\partial F^{p}}{\partial \bar{\sigma}_{ij}} = \frac{3}{2}\frac{\bar{s}_{ij}}{\sqrt{3\bar{J}_{2}}} + \alpha^{p}\delta_{ij} \tag{5.22}$$

5.1.3 Tensile and compressive damage surfaces

The damage function proposed by Chow and Wang [131], and modified by Cicekli et al. [105] to incorporate both tensile and compressive damage separately is used, which has the form

$$g^{\pm} = \sqrt{\frac{1}{2}Y_{ij}^{\pm}I_{ijkl}Y_{kl}^{\pm}} - K^{\pm}\left(\varphi_{eq}^{\pm}\right) \le 0 \tag{5.23}$$

where $K^{\pm}$ is the tensile or compressive damage isotropic hardening function such that $K_0^{\pm}$ is the tensile or compressive damage threshold which is interpreted as the area under the linear portion of the stress-strain diagram; $\varphi_{eq}^{\pm}$ is the equivalent tensile or compressive damage density.

Due to the fact that Ti_2AlC behaves in a brittle manner under tensile loading, one can assume that the tensile yielding of the material is almost coincide with the damage initiation. Therefore, the value of tensile yield strength f_0^{+} is equal to that of the tensile damage threshold K_0^{+}. However, under compressive loading, the stress-strain curves of Ti_2AlC exhibit an inverted shallow V shape rather than a sharp drop as for tensile loading [104]. Therefore, the value of compressive yield strength f_0^{-} is smaller than that of the compressive damage threshold K_0^{-}.

The damage driving force $Y_{ij}^{\pm}$ is interpreted as the energy release rate according to the notion of fracture mechanics, where the following expression is proposed by Abu Al-Rub and Voyiadjis [132]:

$$Y_{rs}^{\pm} = \frac{1}{2}\bar{E}_{ijab}^{-1}\bar{\sigma}_{ab}\frac{\partial M_{ijpq}}{\partial \varphi_{rs}^{\pm}}\bar{\sigma}_{pq} \tag{5.24}$$

The evolution of $\dot{\varphi}_{ij}^{\pm}$ is given by:

$$\dot{\varphi}_{ij}^{\pm} = \dot{\lambda}_d^{\pm}\frac{\partial g^{\pm}}{\partial Y_{ij}^{\pm}} \tag{5.25}$$

where $\dot{\lambda}_d^{\pm}$ is the damage multiplier and one can easily show that $\dot{\lambda}_d^{\pm} = \dot{\varphi}^{\pm}$. This multiplier can be obtained from the following damage consistency conditions:

$$g^{\pm} \le 0,\quad \dot{\lambda}_d^{\pm} g^{\pm} = 0,\quad \text{and } \dot{g}^{\pm}\begin{Bmatrix} <0 \Rightarrow \dot{\lambda}_d^{\pm} = 0 \\ =0 \Rightarrow \dot{\lambda}_d^{\pm} = 0 \\ =0 \Rightarrow \dot{\lambda}_d^{\pm} > 0 \end{Bmatrix} \Leftrightarrow \begin{cases} \text{effective (undamaged state)} \\ \text{damage initiation} \\ \text{damage growth} \end{cases} \tag{5.26}$$

The rate of the equivalent damage density $\dot{\varphi}_{eq}^{\pm}$ is defined as:

$$\dot{\varphi}_{eq}^{\pm} = \sqrt{\dot{\varphi}_{ij}^{\pm}\dot{\varphi}_{ij}^{\pm}} \quad \text{with} \quad \varphi_{eq}^{\pm} = \int_0^t \dot{\varphi}_{eq}^{\pm} dt \tag{5.27}$$

Power tensile and compressive damage evolution laws are used to capture and predict the damage behavior of porous Ti_2AlC:

$$\varphi_{eq}^{+} = B^{+}\left(\frac{K_0^{+}}{K^{+}}\right)\left(\frac{K^{+}}{K_0^{+}} - 1\right)^{q^{+}} \tag{5.28}$$

$$\varphi_{eq}^{-} = B^{-}\left(\frac{K^{-}}{K_0^{-}} - 1\right)^{q^{-}} \tag{5.29}$$

where $B^{\pm}$ and $q^{\pm}$ are material constant. It shows that damage will be initiated when damage hardening function $K^{\pm}$ is greater than the damage threshold $K_0^{\pm}$.

Also, one can obtain the evolution of the damage isotropic hardening functions $\dot{K}^{+}$ and $\dot{K}^{-}$ by taking time derivative of Eq. (5.28) and Eq. (5.29) as follows:

$$\dot{K}^{+} = \frac{K^{+}}{B^{+}\left(q^{+}K_0^{+} - 1 + \frac{K_0^{+}}{K^{+}}\right)}\left(\frac{K^{+}}{K_0^{+}} - 1\right)^{1-q^{+}} \dot{\varphi}_{eq}^{+} \tag{5.30}$$

$$\dot{K}^{-} = \frac{K_0^{-}}{B^{-}q^{-}}\left(\frac{K^{-}}{K_0^{-}} - 1\right)^{1-q^{-}} \dot{\varphi}_{eq}^{-} \tag{5.31}$$

5.2 3D RVEs and finite element modeling

A technique developed in Chapter II to generate FE model of 3D RVE for interpenetrating phase composites (IPCs) based on representative volume element (RVE) method and finite element (FE) method is used this chapter because of the open-cell foam microstructure of porous Ti_2AlC. In other word, pores can be treated as a connected phase. Meanwhile, due to the usage pore former, various microstructures of porous Ti_2AlC with different porosity volume fractions, pore size and shape has been fabricated. The data used to create 3D RVEs in this study are from micrographs and measurements reported in [103], and the detailed microstructure features and 3D RVE generating process will be discussed.

5.2.1 Microstructure of porous Ti_2AlC

The porous Ti_2AlC was fabricated using fast consolidation techniques, i.e. spark plasma sintering (SPS) and pressureless sintering in [103]. The samples fabricated using Ti_2AlC powders by SPS have small porosity volume fraction (i.e. less than 17%) and pore size (15-30μm). To get larger porosity volume fraction and to control pore size, NaCl powder was used as pore former to be mixed with Ti_2AlC powder in cold pressing. The NaCl then can be dissolved using water before pressureless sintering process. There are three groups of pore size formed by this technique, 50-90μm, 170-250μm and 340-500μm [103]. Since the strength of NaCl is much smaller than that of Ti_2AlC, NaCl deformed extensively during cold pressing. As a result, the pore shape of the samples using NaCl pore former is ellipsoidal like while the pore shape of other samples without using pore former is approximately sphere.

Another feature of the porous Ti_2AlC is the open-cell foam structure. For the samples without using NaCl pore former, the volume fraction ratio of open porosity versus overall porosity is around 60%, and this value goes up to 80%-100% for the samples using NaCl pore former. Meanwhile, as pore size increases, the open/overall porosity ratio also increases. For examples, for the samples with porosity volume fraction around 20%, the open/overall porosity ratio is around 85% for 50-90μm pore size group, 95% for 170-250μm pore size group, and almost 100% for 340-500μm pore size group [103].

5.2.2 Simulated microstructure

In modeling of porous media, simplified geometry, such as limited number of spherical shape pores, has been used to represent the microstructure of porous media [120]. It has been found in [119] that the RVE model of composites with perfect spherical shape particles tends to show higher strength than the ones with irregular shape particles. This is attributed to the increased level of stress concentration at the regions with geometric singularity for the irregular shape particles, which is actually more close to the stress state of the real microstructure of the composites. Therefore in this study, instead of sphere and ellipsoid, truncated icosahedron and flat truncated icosahedron (soccer ball shape and flat soccer ball shape) are adopted to represent the pore shape in order to reflect the irregularity of the interconnected pore phase more realistically. Another advantage of using truncated icosahedron shape pores is that it can tremendously reduce the element number in the mesh of FE model. The reason is that when we use perfect spherical shape, there are a lot of tiny segments of curved surface existing due to the connectivity of the pores. It leads to much denser mesh comparing to the truncated icosahedron shape with only flat surfaces which is easier to mesh.

In order to achieve desired volume fraction of porosity the connectivity of neighboring pores is controlled by adjusting the range of distance among pores. Similar to the illustration showed before in Chapter III Figure 17, the relation between adjoining pores can be categorized into three states: separation, in contact, and interpenetration states. Although all these three states may exist in the real microstructure of the porous Ti_2AlC at the same time, the in contact state, see in Figure 17 (b), is not considered in

our model for simplicity. Since for this state, additional contact properties need to be defined, which is unknown. Also, numerical singularity may arise at the sharp tip of the region which is close to the contact point between pores. Hence, only separation and interpenetration states, Figure 17 (a) and (c), are considered in the modeling, which is achieved by controlling the range of the distance between centers of pores.

In general, the dimensions of the 3D RVEs are selected to include enough number of random distributed interconnected pores, and in the meanwhile be statistically homogeneous and representative of local continuum properties of the porous Ti_2AlC. As mentioned in the previous section, the pore shape of porous Ti_2AlC can be controlled by using pore former. Therefore, depending on the pore shape, two configurations of 3D RVEs are created, i.e. one with sphere-like (truncated icosahedron) pores and the other with aligned ellipsoid-like (flat truncated icosahedron) pores.

5.2.2.1 Porous Ti_2AlC with sphere-like pores

The dimensions of the 3D RVEs for porous Ti_2AlC with sphere-like pores are taken to be 100μm×100μm×100μm. These samples were fabricated with 45-90μm in diameter Ti_2AlC powders only. As observed in the micrograph in [103], the pore size is the range of 15-30μm range and the deviation of the pore size is relatively small. Therefore, three different sized pores are used in the 3D RVEs. As it is difficult to describe the size of a truncated icosahedron, the radiuses of the corresponding circumscribed spheres of the truncated icosahedron are used to represent the size of the pores. They are 15μm, 20μm, and 30μm, respectively, and the gradation of the

corresponding pores is assumed to be approximately 2:3:3. The porosity volume fraction, pore number within each 3D RVE is summarized in Table 8. The corresponding 3D RVEs with different porosity volume fractions are shown in Figure 41.

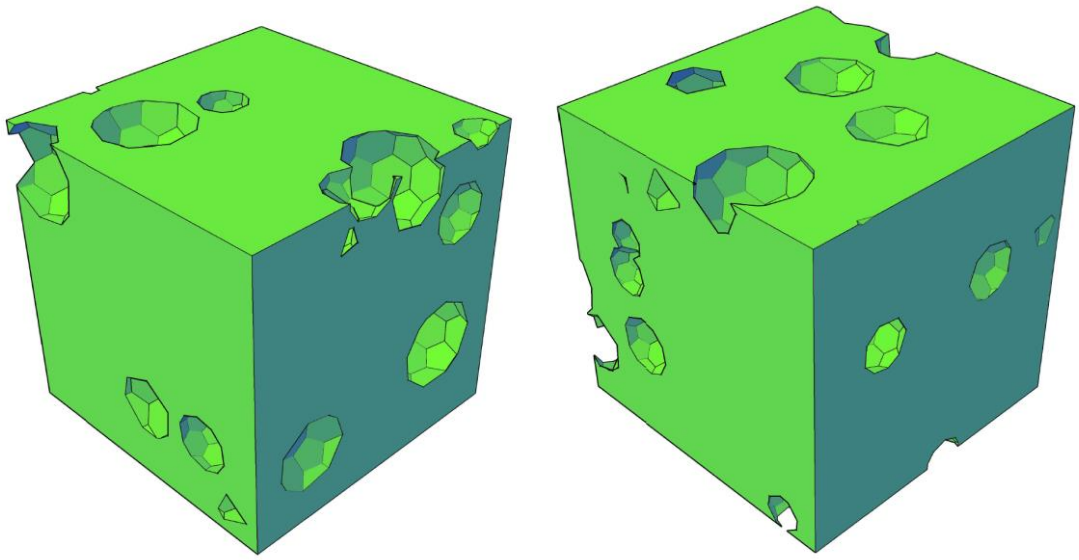

(a) (b)

Figure 41: 3D RVEs ($100 \times 100 \times 100 \mu m^3$) for pore size 15-30μm group porosity volume fractions: (a) 8.9%, (b) 16%, (c) 28.3%, (d) 35.2%, (e) 40%, and (f) 47%.

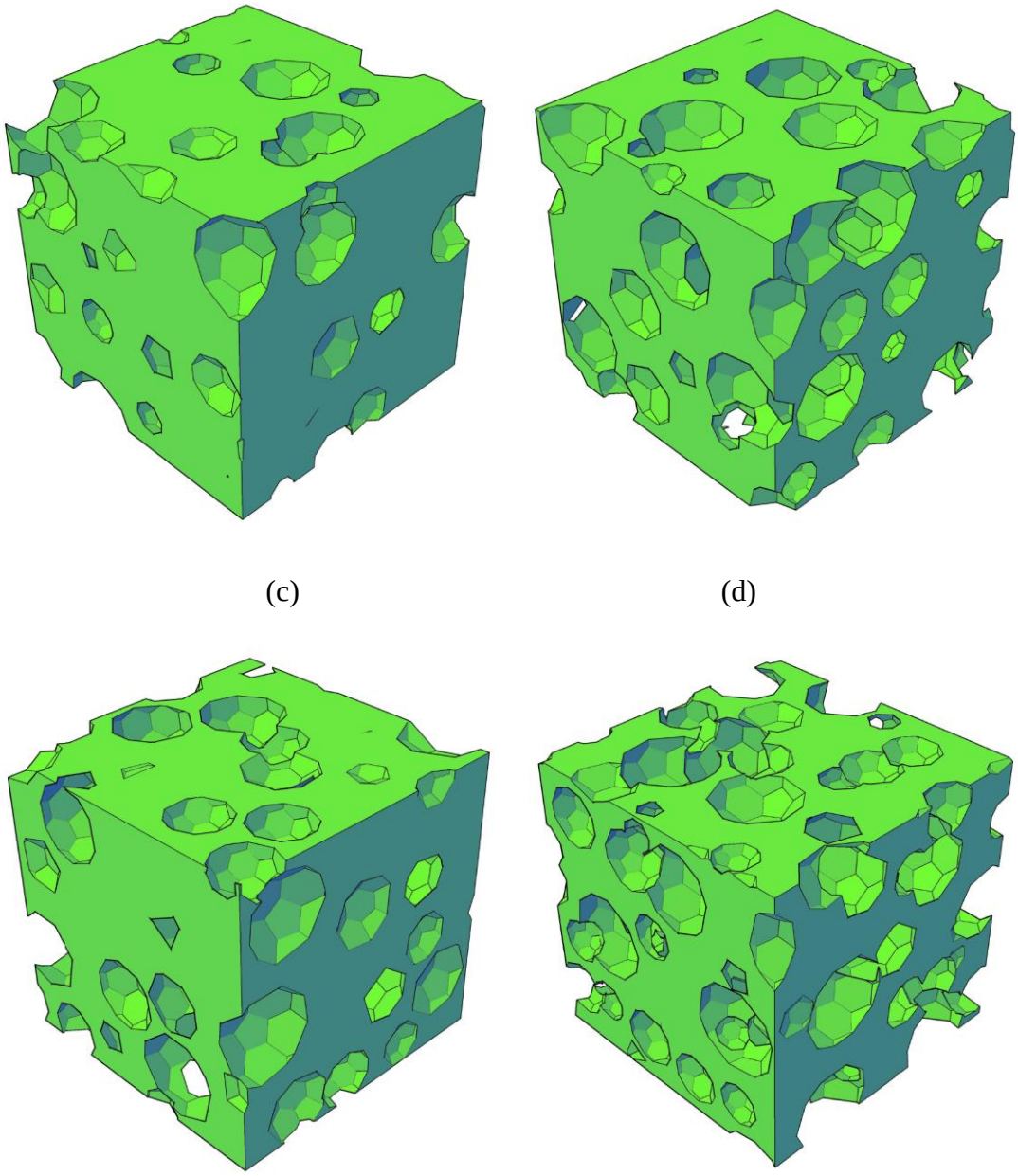

(c) (d)

(e) (f)

Figure 41: Continued.

Table 8: 3D RVEs with sphere-like pores

RVE dimensions(μm)	Pore size (μm)	Porosity (vol. %)	Pore number within RVE
100×100×100	15-30	8.9	27
		15.9	57
		28.3	76
		35.2	90
		40.0	120
		47.1	139

5.2.2.2 Porous Ti_2AlC with ellipsoid-like pores

As mentioned before, the porous Ti_2AlC fabricated by Hu et al. and reported in [103] also has various larger pore sizes (i.e. three groups of pore size: 50-90μm, 170-250μm, and 340-500μm) and ellipsoid like pore shape. This is result of using NaCl powder as pore former to mix with Ti_2AlC powder during cold pressing before pressureless sintering. Since the stiffness of NaCl powder is much smaller than Ti_2AlC powder and thus the former deformed more extensively than the latter in cold pressing, the pore shape is ellipsoid like. In this study, the dimensions of the flat truncated icosahedron representing pore shape is assumed to be the same in the two directions normal to the compressive loading direction and one half of those in the compressive loading direction, i.e. if compressive loading direction is z-direction, then we have the three axis of inscribed ellipsoid within the flat truncated icosahedron is $a_1=a_2=2a_3$ The

dimensions of the 3D RVEs for porous Ti2AlC with ellipsoid-like pores are taken to be 1000μm×1000μm×1000μm for all three pore size groups for the purpose of study on pore size effect. Furthermore, the distribution of the pore size becomes broader as pore size increases due to the broader particle size range of NaCl pore former used. Therefore, a broader pore size range should be considered in creating 3D RVEs. In this study, 9 pore sizes are used within each pore size group and follow a normal distribution to approximate the pore size distribution observed in the experiment, which is shown in Figure 42. The pore size group, porosity volume fraction, pore number within each 3D RVE is summarized in Table 9 and the corresponding 3D RVEs are shown in Figure 43.

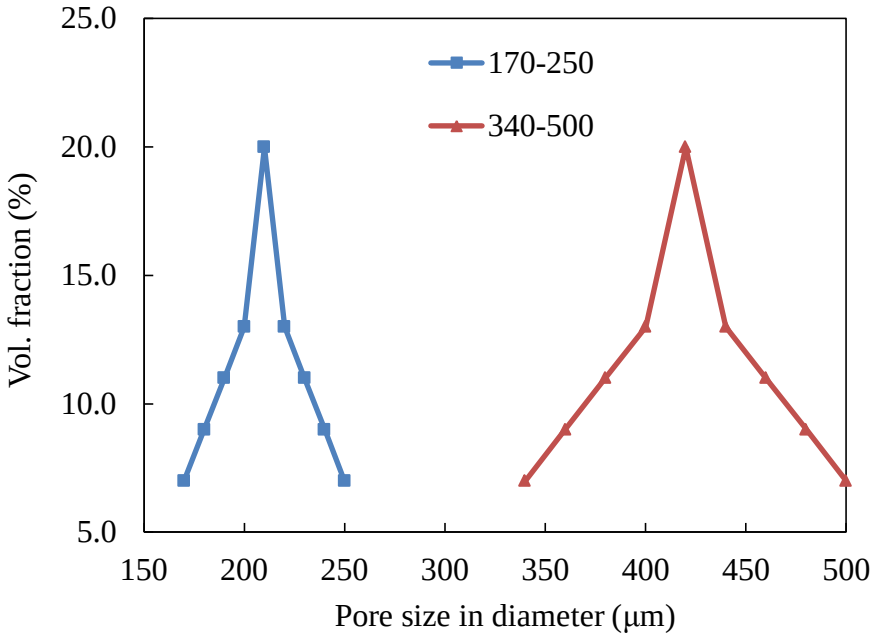

Figure 42: Pore size distribution of porous Ti_2AlC with different pore size groups: 50-90μm, 170-250μm and 340-500μm.

Table 9: RVEs with ellipsoid-like pores

RVE dimensions(μm)	Pore size (μm)	Porosity (vol. %)	Pore number within RVE
1000×1000×1000	170-250	32.8	229
	170-250	40.8	302
	340-500	33.5	43

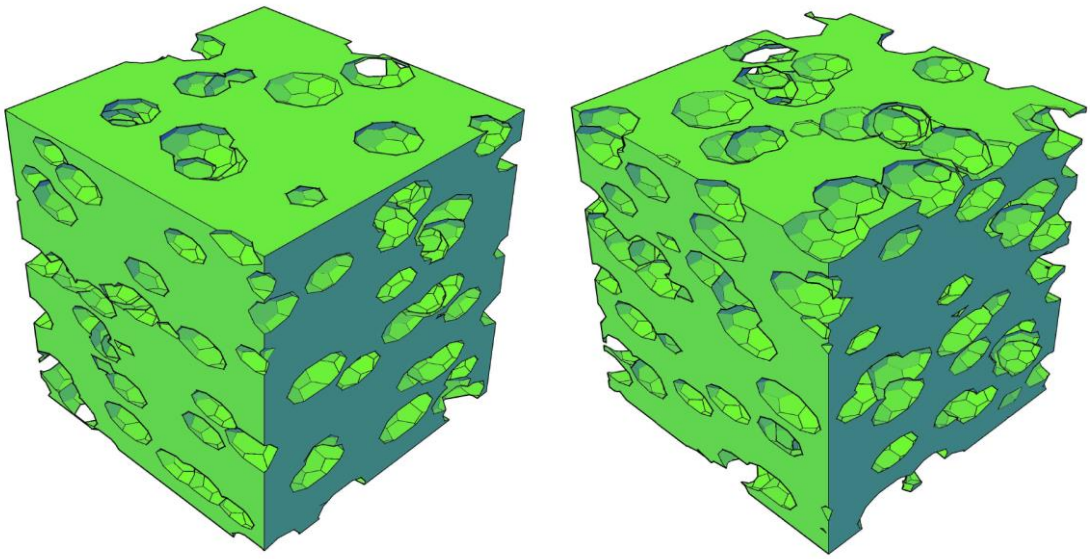

(a) (b)

Figure 43: 3D RVEs (1000×1000×1000μm^3) for (a) pore size 170-250μm, porosity volume fraction 32.8%, (b) pore size 170-250μm, porosity volume fraction 40.5%, (c) pore size 340-500μm, porosity volume fraction 33.5%.

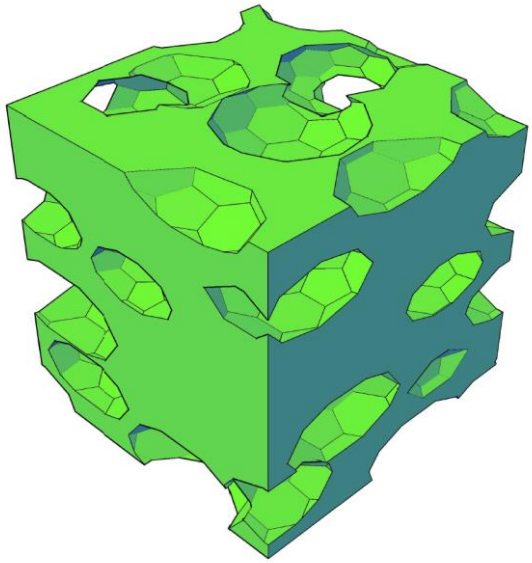

(c)

Figure 43: Continued.

5.2.3 FE mesh and boundary conditions

Due to the complex geometry of the 3D RVEs, they are meshed with C3D4 and C3D10 element (four-node linear tetrahedral element and ten-node quadratic tetrahedral element) in Abaqus which are geometrically versatile and are very convenient to mesh a complex shape. Here, for 3D RVEs of porous Ti_2AlC with sphere-like pores ($100\times100\times100\mu m^3$), the approximate edge length of elements is 4μm, and the corresponding FE models contain around 140,000 elements. For the 3D RVEs of porous Ti_2AlC with ellipsoid-like pores ($1000\times1000\times1000\mu m^3$), the approximate edge length of elements is 30μm, and the element number is 186,524 and 179,956 for Figure 43(a) and (b) in 170-250μm pore size group, and 168,354 for Figure 43(c) in 340-500μm pore size group.

The RVEs used in this chapter are also created by cutting parts of a simulated microstructure with random distributed phases based on actual microstructure of porous Ti_2AlC, and they do not exhibit geometry periodicity. Therefore, as mentioned before in Chapter III, instead of PBC, a mixed boundary condition designed for such RVEs [120] are imposed in this study: uniform displacements are imposed on the faces perpendicular to the loading direction. To simulate an interior domain compatible with the surrounding material, the faces parallel to the loading direction remain straight and parallel during deformation.

5.3 Numerical simulation and results

Linear elastic and nonlinear plasticity-damage coupled FE analysis is carried out on the FE models of 3D RVEs to predict effective elastic moduli and study the coupled plastic-damage behavior of porous Ti_2AlC, respectively. The coupled plastic-damage constitutive model developed and implemented in Abaqus via user material subroutine UMAT in [119] is used in conducting 3D numerical simulations. The effect of porosity volume fraction, pore size and shape on effective elastic moduli and compressive strength is investigated. The material properties of MAX phase T_2AlC are listed in Table 10 [104].

Table 10: Material constants of dense T_2AlC.

Young's modulus *E* (GPa)	Poisson's ratio	Shear modulus *G* (GPa)	Compressive strength(MPa)
277	0.17	118.8	540

5.3.1 Effective elastic moduli

Mori-Tanaka method is one the most well-known micromechanics methods in predicting effective elastic moduli of multi-phase composites with non-overlapping inclusion phase which is derived based on the Eshelby solution. In this method, the effects of other inclusions to one inclusion are through its surrounding matrix. At relatively low phase concentration (due to the dilute assumption used in deriving the formulation), Mori-Tanaka method gives good estimation of effective elastic moduli for isotropic and homogeneous composites. Another micromechanics based unit cell method aforementioned in Chapter II, which is particularly designed for interpenetrating phase composites, is used here to predict the effective elastic moduli of the given porous Ti_2AlC [59]. The expression of the effective Young's modulus and shear modulus of the two-phase interpenetrating phase composite are expressed as Eq. (2.1) and Eq. (2.2)

If the interconnected pores are treated as one of the constituent phases, referred as phase "1" and matrix referred as "0", then the following limiting case should be used in Mori-Tanaka methods and unit cell method.

$$\frac{E_1}{E_0} \to 0, \quad \frac{G_1}{G_0} \to 0 \tag{5.32}$$

The unit cell method reduces to

$$E=(1-a)^2 E_0,\quad G=(1-a)^2 G_0 \tag{5.33}$$

The Mori-Tanaka method gives

$$\begin{aligned} K &= K_0 - \frac{f_1 K_0 (3K_0+4\mu_0)}{3K_0+4\mu_0-3(1-f_1)K_0} \\ \mu &= \mu_0 - \frac{5 f_1 \mu_0 (3K_0+4\mu_0)}{5(3K_0+4\mu_0)-6(1-f_1)(K_0+2\mu_0)} \end{aligned} \tag{5.34}$$

The corresponding curves of predicted elastic moduli versus porosity volume fraction are shown in Figure 44 and Figure 45. The experimental data are those from [103], using two fabrication techniques, i.e. pressureless-sintering and spark plasma sintering (SPS). The corresponding data points are distinguished in the figures by using different markers.It shows that most of experimental data points with relatively large porosity volume fraction are relative lose to unit cell method, while two data points with relatively small porosity volume fraction (i.e. 8.5%, 13.6%) are predicted well by Mori-Tanaka method. Also, for two data points with nearly the same porosity volume fractions, 13.6% and 13.8%, there is around 30% difference for both the corresponding measured effective Young's moduli and shear moduli respectively. Our conjecture for the explanation of the above phenomena is because of the change of porosity percolation or interconnectivity. It has been observed in the experiment that the sharp jumps of mechanical properties of composites with increasing volume fraction of a particular phase are related to the formation of percolated or connected microstructures in composites [133, 134]. Since Mori-Tanaka method here represents the case when there is no overlapping among the pores while the unit cell method represents the case when

the pore phase is fully connected in the shape the 3D cross-truss. When the porosity volume fraction increases and reaches a critical value, a connected microstructure is first likely to form and the values of corresponding effective Young's modulus and shear modulus have a jump. In other words, due to the change of microstructure, the dependence of the elastic properties of the porous Ti_2AlC on the porosity has been changed.

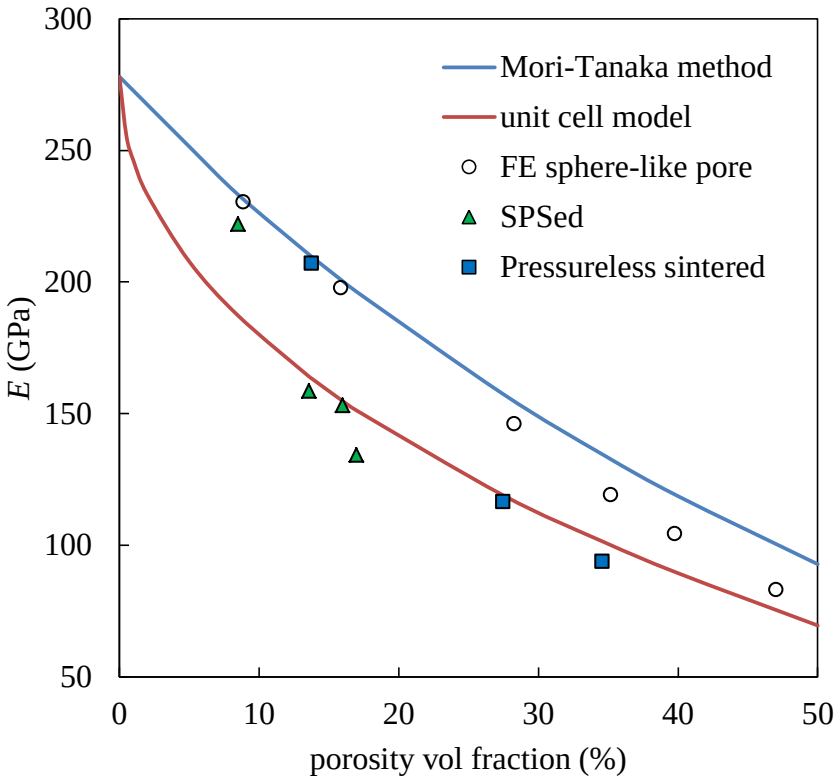

Figure 44: Comparisons of predicted effective Young's modulus obtained by Mori-Tanaka method, unit cell method and FE models with sphere-like pores with experimental results.

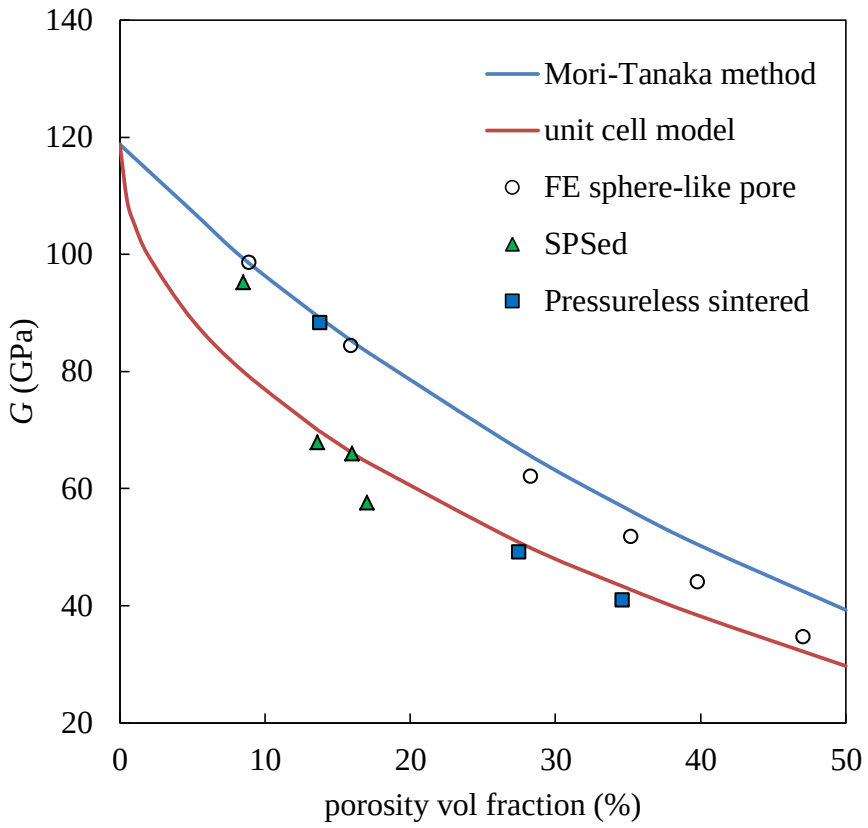

Figure 45: Comparisons of predicted effective Shear modulus obtained by Mori-Tanaka method, unit cell method and FE models with sphere-like pores with experimental results.

Next, the effective elastic moduli of porous Ti_2AlC with sphere-like and ellipsoid-like pores are obtained from FE models of 3D RVEs using linear elastic material properties. Uniaxial tension and simple shear tests are conducted on the FE models of 3D RVEs with load in the x-, y-, and z-directions.

5.3.1.1 Porous Ti_2AlC with sphere-like pores

The FE predicted effective elastic moduli are summarized in Table 11. It is found that the effective elastic moduli approximately follow the relation $G = E/2(1+\nu)$ which is valid for linear isotropic elastic material. Therefore, the corresponding porous Ti_2AlC achieve approximate isotropy, and further we can conclude that the RVEs created are statistically homogeneous and can represent the local continuum properties of the porous Ti_2AlC. Comparisons of the effective Young's modulus and shear modulus obtained from FE models of 3D RVEs with Mori-Tanaka methods, unit cell method and experimental results are also shown in Figure 44 and Figure 45, respectively.

Table 11: Effective elastic moduli of porous T_2AlC with sphere-like pores.

Pore size (μm)	Porosity (vol. %)	*E* (GPa)	*G*(GPa)	Poisson's ratio
15-30	8.9	230.26	98.57	0.171
	15.9	197.57	84.40	0.173
	28.3	145.96	62.07	0.177
	35.2	121.05	52.47	0.182
	40.0	100.67	42.97	0.182
	47.1	80.10	34.60	0.188

It is shown in Figure 44 and Figure 45 that the curve of predicted effective Young's moduli obtained from the FE models of 3D RVEs for porous Ti_2AlC with pore

size 15-30μm and various porosity volume fractions lies between the Mori-Tanaka method and unit cell method. Furthermore, at small porosity volume fraction, the FE predicted Young's modulus and shear modulus are more close to the curve of Mori-Tanaka method bound. However, as the porosity volume fraction increases the FE predictions gradually deviate from Mori-Tanaka method and get closer to the curve of unit cell method. Again, the explanation of this phenomenon is the change of porosity percolation or interconnectivity. When generating 3D RVE, high open/overall porosity can be achieved by adjusting connectivity of sphere-like pores for high porosity volume fraction. However, for low porosity volume fraction, it is hard to achieve high open/overall porosity observed in experiment by just control the connectivity of the sphere-like pores. In the real microstructure of porous Ti_2AlC, this high open/overall porosity is due to the presence of pore channels at grain edges left at the end of the sintering. Actually, as mentioned in [135], the "sintering" refers to the process of pore shape change, shrinkage and grain growth of in contact solid particles under high temperature. In details, at initial stage of sintering spherical powders are in tangential contact; at near end of initial stage, powders begin to coalesce and the neck growth among the powders can be observed; at intermediate stage, grains are forming which have shape of polyhedron and with enclosing pore channels at grain edges; at final stage, pores channels shrink and eventually disappear while pores shape become sphere like polyhedron [135]. Therefore, it can be speculated that the high open/overall porosity ratio for low porosity volume fraction is caused by the existence of pore channels at grain edges which are not complete eliminates during the sintering process. Since the

percolation models are beyond the scope of this study and it is difficult to include both interconnected tiny cylindrical-like pores and relatively large sphere-like pores in creating 3D RVE, only the cases with sphere-like and ellipsoid-like pores are investigated in this study.

5.3.1.2 Porous Ti_2AlC with ellipsoid-like pores

The micromechanics based methods and FE models of 3D RVEs mentioned before to estimate the elastic moduli of porous Ti_2AlC with sphere-like pores are for isotropic case. However, the material system of porous Ti_2AlC with aligned ellipsoid-like pores is transversely isotropic, since it is assumed that three axis lengths have the relation of $a_1=a_2=2a_3$ for inscribed ellipsoid of the flat truncated icosahedron used in corresponding 3D RVEs. Therefore, there are five independent elastic moduli due to transverse isotropy. The FE predicted effective elastic moduli in longitudinal direction (denoted by subscript "*L*") and transverse direction (denoted by subscript "*T*") are shown in Table 12.

Table 12: Effective elastic moduli of porous T_2AlC with ellipsoid-like pores.

Pore size(μm)	Porosity (vol. %)	E_T(GPa)	E_L(GPa)	G_T(GPa)	G_L(GPa)	ν_L
170-250	32.8	141.14	87.69	61.66	47.01	0.142
170-250	40.5	115.55	59.56	50.15	35.74	0.140
340-500	33.5	145.02	81.09	62.22	47.00	0.140

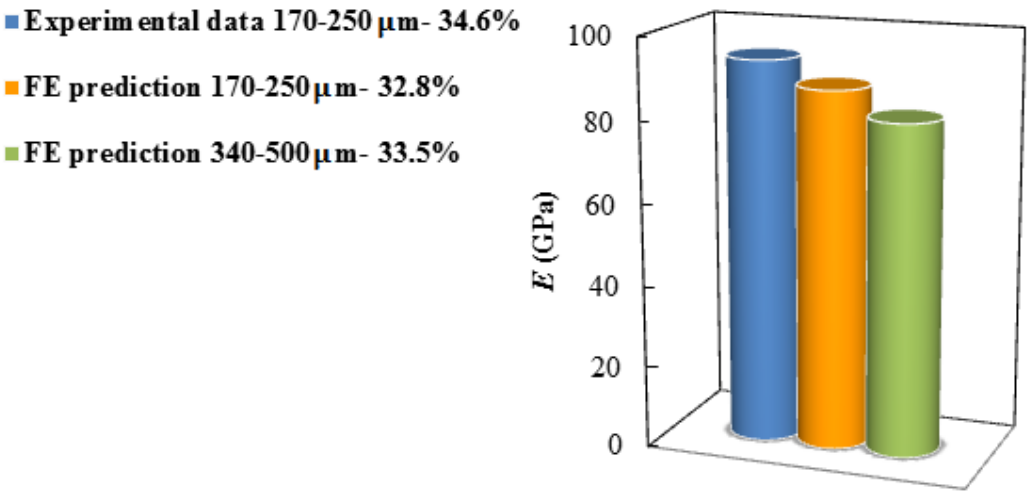

(a)

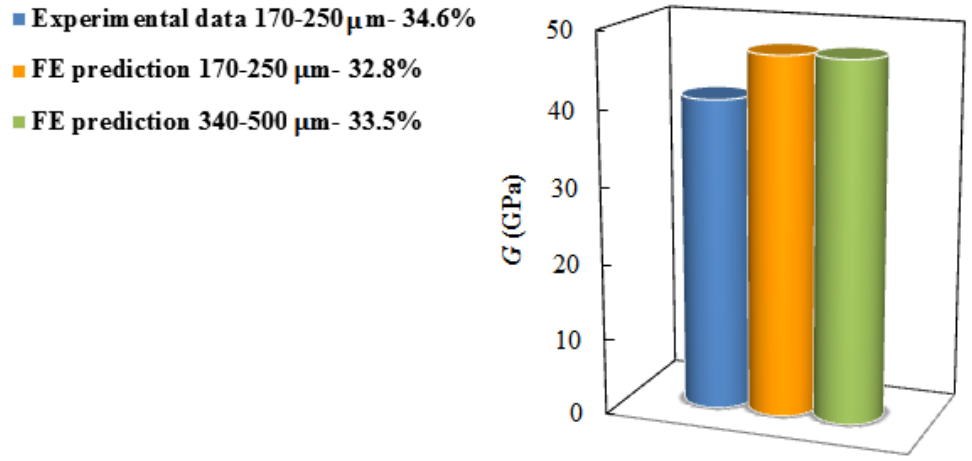

(b)

Figure 46: Comparisons of predicted effective elastic moduli obtained by FE models with ellipsoid-like pores with experimental results: (a) Young's modulus, (b) shear modulus.

The measured Young's modulus and shear modulus are only available for the porous Ti_2AlC sample with 34.6% 170-250μm ellipsoid-like pores [103]. The FE predicted Young's modulus and shear modulus for 3D RVE with 32.8% 170-250μm and 340-500μm ellipsoid-like pores are compared with experimental data and plotted in Figure 46 (a) and (b), respectively. It is shown that the FE predicted Young's moduli in longitudinal direction obtained from above mentioned 3D RVEs are around 7.0% and 15.6% smaller than the measurement, while the corresponding shear moduli are nearly the same and are 5.9% larger than the experimental result. Therefore, it can be seen that the pore size does not affect the effective elastic moduli much for the given porous Ti_2AlC.

5.3.2 Meso-scale simulations for damage behavior of porous Ti2AlC with aligned ellipsoid-like pores

As mentioned before, NaCl pore former is used in fabricating porous Ti_2AlC in the experiments to control pore size and shape which results in ellipsoid-like pore shape and three pore size groups. For the compressive strength, experimental data is mostly available for the group of samples with ellipsoid-like pores. Therefore, in this section, the 3D RVEs with aligned ellipsoid-like pores are used in plastic-damage coupled finite element analysis to investigate the effects of porosity volume fraction, pore size and loading direction on compressive behavior of porous Ti_2AlC. The coupled plasticity-damage constitutive model outlined in previous section is adopted. This model was

developed and implemented in Abaqus via user material subroutine UMAT by Kim and Abu Al-Rub in [119], and is used in conducting 3D numerical simulations in this study.

5.3.2.1 Tensile and compressive material properties of dense Ti_2AlC

For the material constants in yield criterion and plastic potential function, $\alpha = 0.12$, $\alpha^p = 0.2$ are used in this study. Other tensile and compressive material constants used in the constitutive model are listed in Table 13 and Table 14, respectively. Since, there is no experimental data available for stress-strain relation of dense Ti_2AlC under tensile load in the literature due to the difficulty in conducting tensile test, the initial tensile yield strength of Ti_2AlC is assumed to be smaller or equal to its flexure strength, i.e. f_0^+ =175, 225 and 275MPa, and other constants are selected empirically.

Table 13: Tensile material constants used in the FE analysis.

Tensile plastic material constants		Tensile damage material constants		
f_0^+ (MPa)	h^+ (MPa)	K_0^+ (MPa)	B^+	q^+
175, 225 and 275	50000	225	1.7	1.0

Table 14: Compressive material constants used in the FE analysis.

Compressive plastic material constants			Compressive damage material constants		
f_0^- (MPa)	Q^- (MPa)	b^-	K_0^- (MPa)	B^-	q^+
175, 225 and 275	5000	55	300	0.155	0.73

For simplicity, it is assumed that $f_0^- = f_0^+$ in the following study. Using the above mentioned parameters, the corresponding predicted overall compressive and tensile nonlinear behaviors of dense Ti_2AlC are shown in Figure 47 and Figure 48, respectively. As shown in Figure 47, with fixed compressive damage threshold K_0^-, the compressive calibrated stress-strain curves and damage density-strain curves for both f_0^- =175, 225 and 275MPa are very similar, and at the same time agree with the experimental data very well. In contrast, it is shown in Figure 48 that the value of initial tensile yield stress f_0^+ plays an important role in tensile failure of dense Ti_2AlC, because f_0^+ is assumed to be equal to tensile damage threshold K_0^+. In Figure 48 (a), it can be seen that the curve of f_0^+ =175MPa starts the softening stage (plastic yielding and damage initiation) earlier than that of f_0^+ =225MPa and reach a lower stress level at strain equals to 6.0E-3. Same trend can also be found for the cases of f_0^+ =225 and 275MPa. This can be observed more clearly from damage density in Figure 48 (b). For example, the tensile damage density for the case with f_0^+ =175MPa becomes non-zero at strain is about 6.0E-4 compared to about 8.0E-4 and 1.0E-3 for the case with f_0^- =225 and 275MPa. Also, the tensile damage density for f_0^+ =175MPa case achieves approximate 0.96 at strain equals to 6.0E-3 while this value for the letter two cases is around 0.84 and 0.74, respectively.

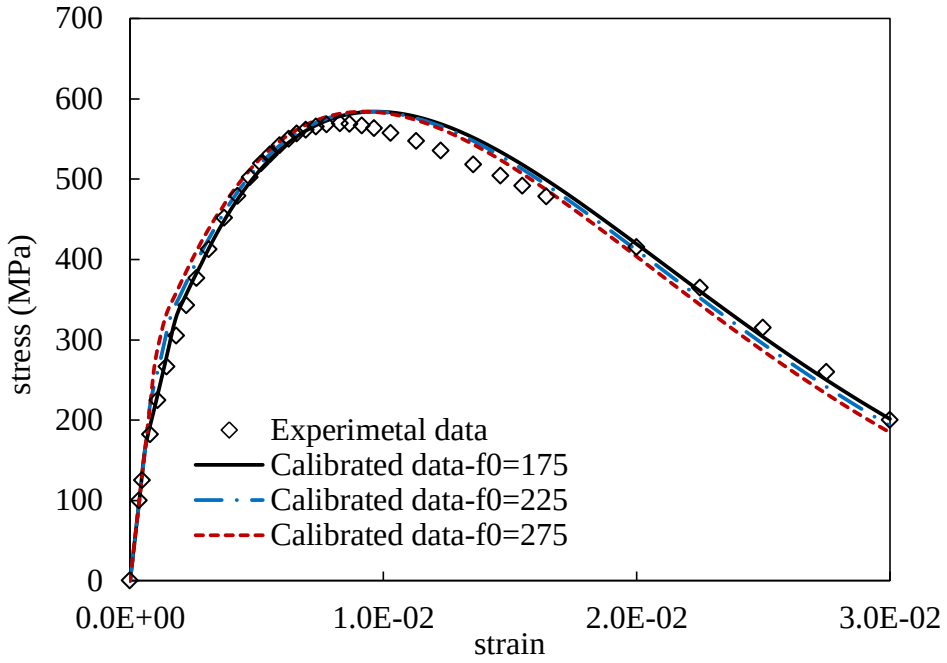

(a)

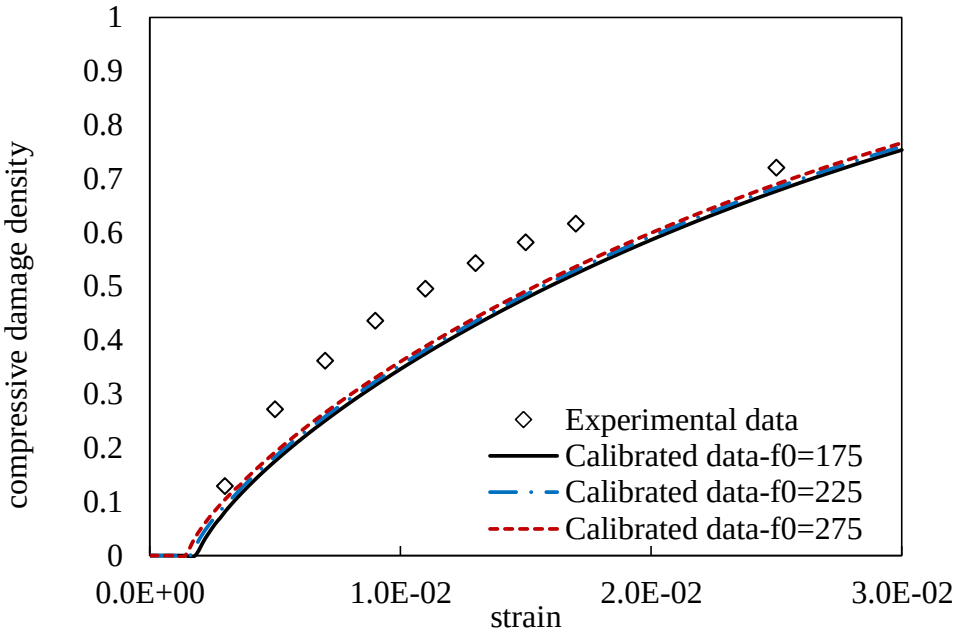

(b)

Figure 47: Compressive plastic-damage behavior of dense Ti_2AlC: (a) stress-strain curve, (b) tensile damage density-strain curve.

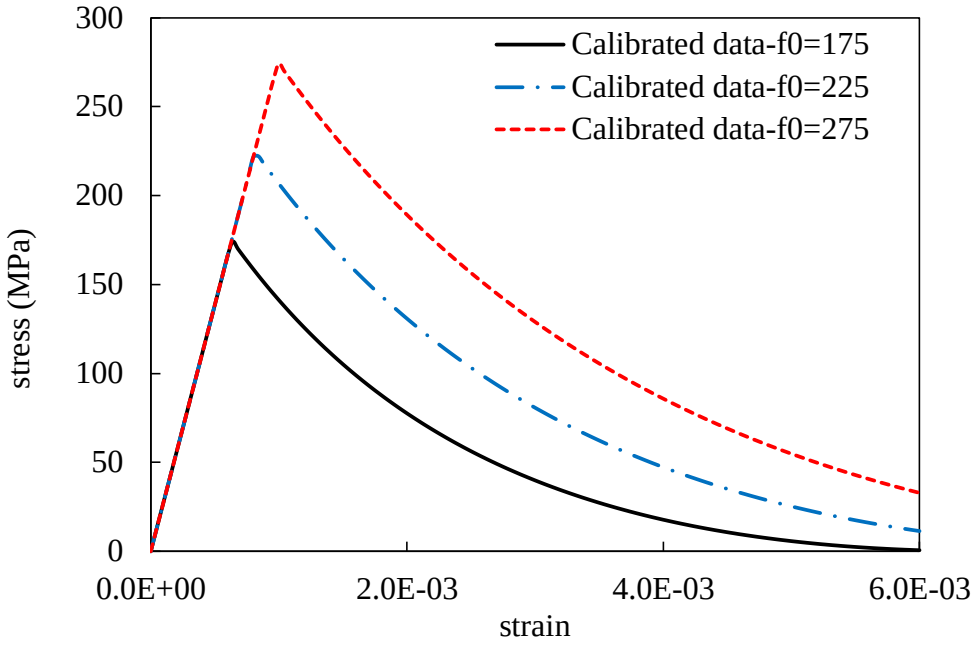

(a)

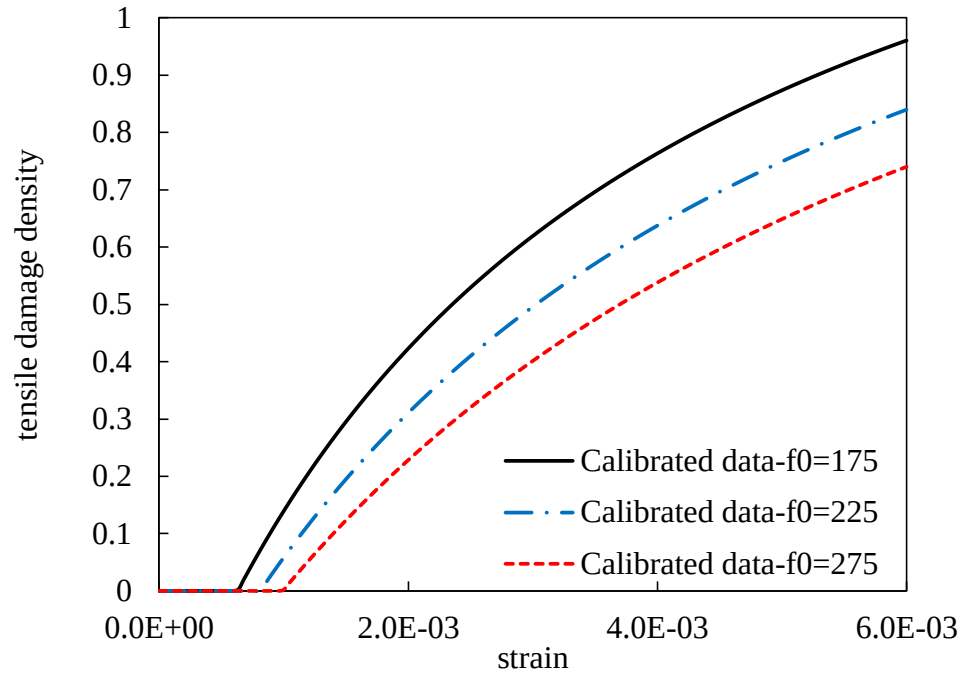

(b)

Figure 48: Tensile plastic-damage behavior of dense Ti_2AlC: (a) stress-strain curve, (b) compressive damage density-strain curve.

5.3.2.2 The effect of varying the tensile properties of dense material

Since the tensile strength of dense Ti_2AlC is relatively small compared to compressive strength and tensile failure is more of brittle style, the damage of given porous Ti_2AlC will first initiate locally where principle tensile stress reaches the initial tensile yield strength (also the tensile damage threshold). Accumulation of these tensile damages will lead to decohesion of the material locally and form small cracks within porous Ti_2AlC. The growth and coalesce of these small cracks will eventually cause final failure of the porous system. Therefore, even though under uniaxial compressive load, the failure mechanism and overall compressive strength of porous Ti_2AlC material system is strongly dependent on the tensile behavior of dense Ti_2AlC. The effect of initial tensile yield stress of dense Ti_2AlC on the overall compressive behavior of porous Ti_2AlC material system is studied.

As an example, finite element analysis is carried out on the 3D RVE for porous Ti_2AlC with 32.8% aligned 170-250μm ellipsoid-like pores, as shown in Figure 43 (a). The obtained stress-strain relations for three cases: $f_0^+ = f_0^- = 175$, 225 and 275MPa with compressive load in longitudinal direction (z-direction) are shown in Figure 49. For all three cases, stress increases linearly with strain when strain is relatively small, and the initial stiffness of the porous Ti_2AlC material system is approximately equal to the longitudinal Young's modulus E_L, i.e. 87.69GPa, as previously shown in Table 12. As the strain continuously increases, the stress increases nonlinearly and then experiences a softening stage, which forms a reverted narrow "V" shape for all three cases. It other words, unlike typical porous ceramic, the failure of the given porous Ti_2AlC is relatively

graceful which coincide with the description in the experiment [103]. The compressive strength obtained from 3D RVE for the cases $f_0^+ = f_0^- = 175$, 225 and 275MPa is around 135, 153 and 166MPa, respectively. The results of the latter two cases fell into the range of measured compressive strength, i.e. 140-195MPa [103].

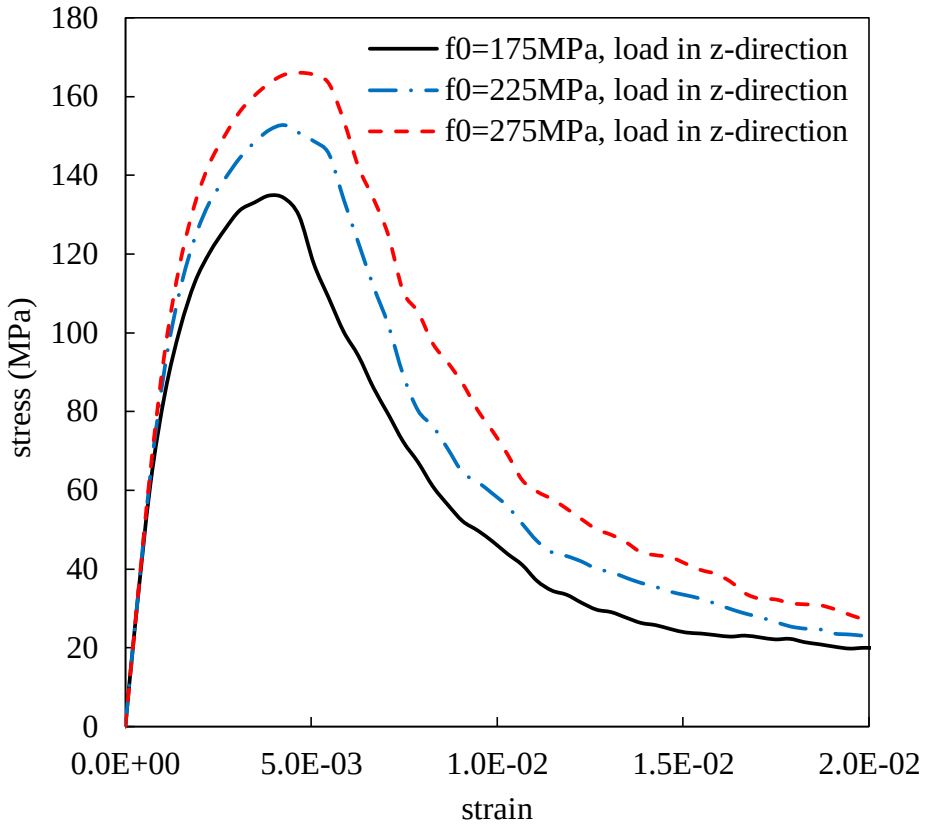

Figure 49: Stress-strain relation obtained from 3D RVE of porous Ti_2AlC with 32.8% aligned 170-250μm ellipsoid-like pores for the cases: initial yield stress $f_0^+ = f_0^- = 175$, 225, 275MPa with load in *z*-direction.

To graphically see the plastic-damage evolution process in porous Ti_2AlC, distributions of tensile equivalent plastic strain and corresponding tensile damage density, as well as compressive equivalent plastic strain and corresponding compressive damage density of porous Ti_2AlC with 32.8 vol. % aligned 170-250μm ellipsoid-like pores ($f_0^+ = f_0^- = 225\text{MPa}$ case) with compressive load in longitudinal direction (z-direction) at different strain levels are plotted in Figure 50-Figure 53.

As expected, damages usually are formed near the areas with high plastic strain level. For example, it can be observed that the pattern of tensile damage distribution in Figure 51 is very similar to that of high tensile equivalent plastic strain distribution in Figure 50. Comparing the tensile and compressive equivalent plastic strain distributions shown in Figure 50 and Figure 52, it is found that at relatively high strain level, tensile equivalent plastic strain distribution has more concentrated areas, although the maximum value of compressive equivalent plastic strain is higher than that of tensile equivalent plastic strain.

For damage evolution process, it is shown in Figure 51 that initially the tensile damage occurs randomly in the porous Ti_2AlC at low strain level. But as strain level increases, the local damage accumulates and starts to form small cracks. Further, these small cracks grow, coalesce and become larger cracks in the given porous Ti_2AlC. Also, it can be seen in Figure 51 and Figure 53 that at $\varepsilon = 1.0\text{E-}1$, considerable part of the given porous Ti_2AlC is damaged due to tensile failure (i.e. tensile damage density approaches 1.0), whereas there is only small part of the porous system is damaged due to compressive failure. Therefore, it can be concluded that the damage mechanism of given

porous Ti_2AlC is dominated by localized tensile damage (i.e., decohesion of the material).

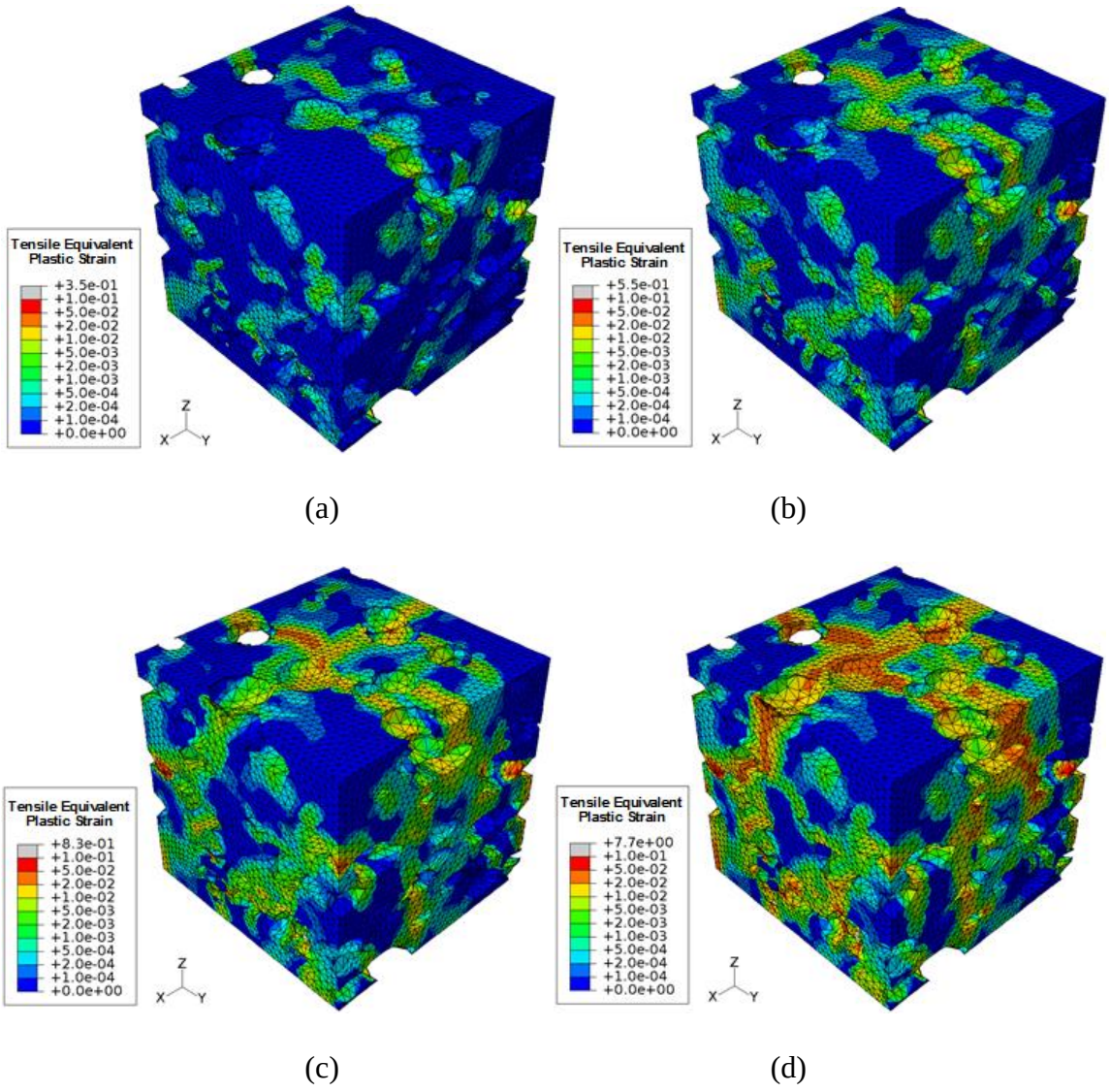

Figure 50: Tensile equivalent plastic strain for porous Ti_2AlC with 32.8 vol. % aligned 170-250μm ellipsoid-like pores ($f_0^+ = f_0^- = 225$MPa case) with compressive load in z-direction at different strain level: (a) $\varepsilon = 3.0$E-2, (b) $\varepsilon = 5.0$E-2, (c) $\varepsilon = 7.0$E-2, (d) $\varepsilon = 1.0$E-1.

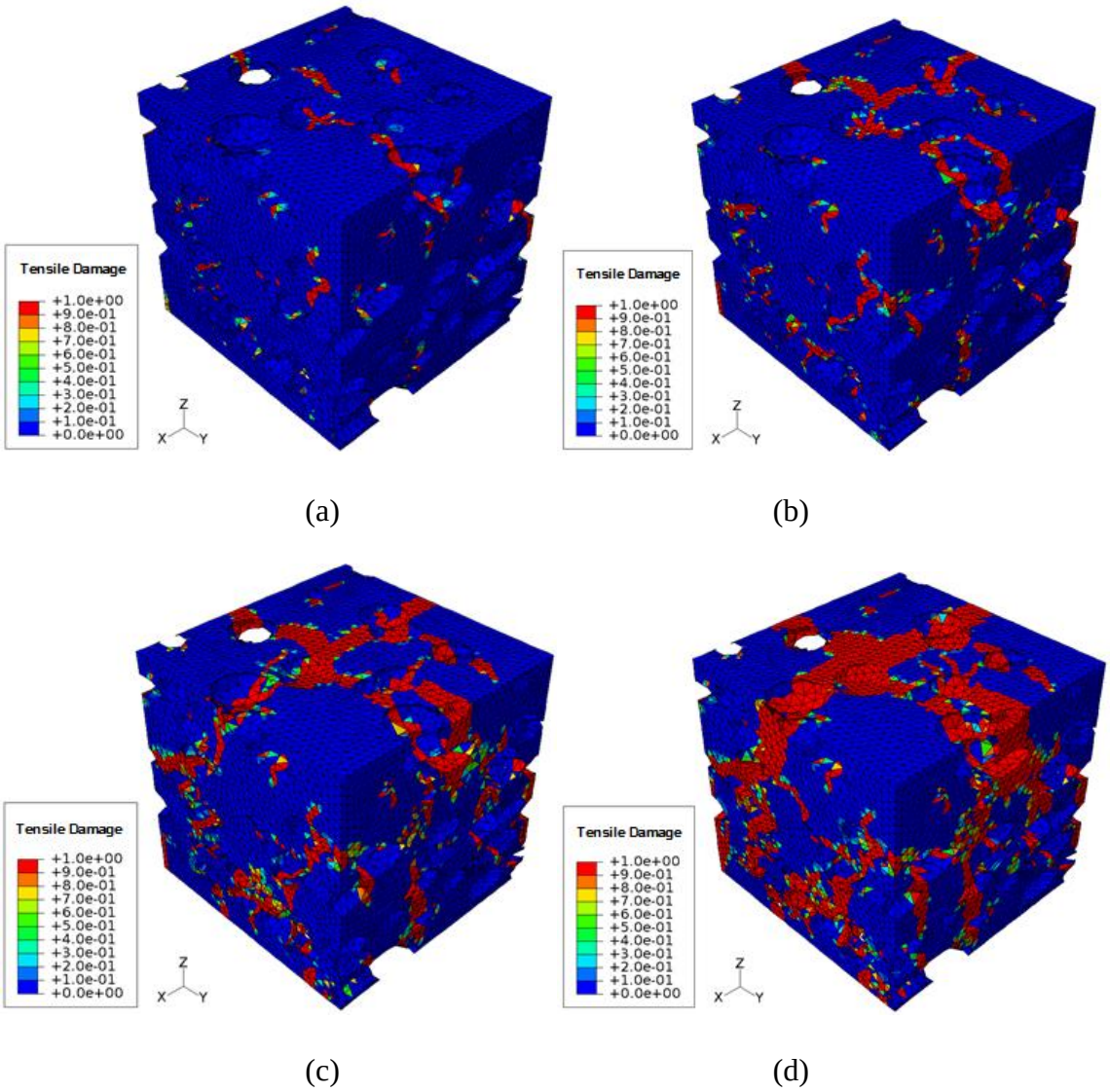

Figure 51: Tensile damage density for porous Ti_2AlC with 32.8 vol. % aligned 170-250μm ellipsoid-like pores ($f_0^+ = f_0^- = 225$MPa case) with compressive load in z-direction at different strain level: (a) $\varepsilon = 3.0$E-2, (b) $\varepsilon = 5.0$E-2, (c) $\varepsilon = 7.0$E-2, (d) $\varepsilon = 1.0$E-1.

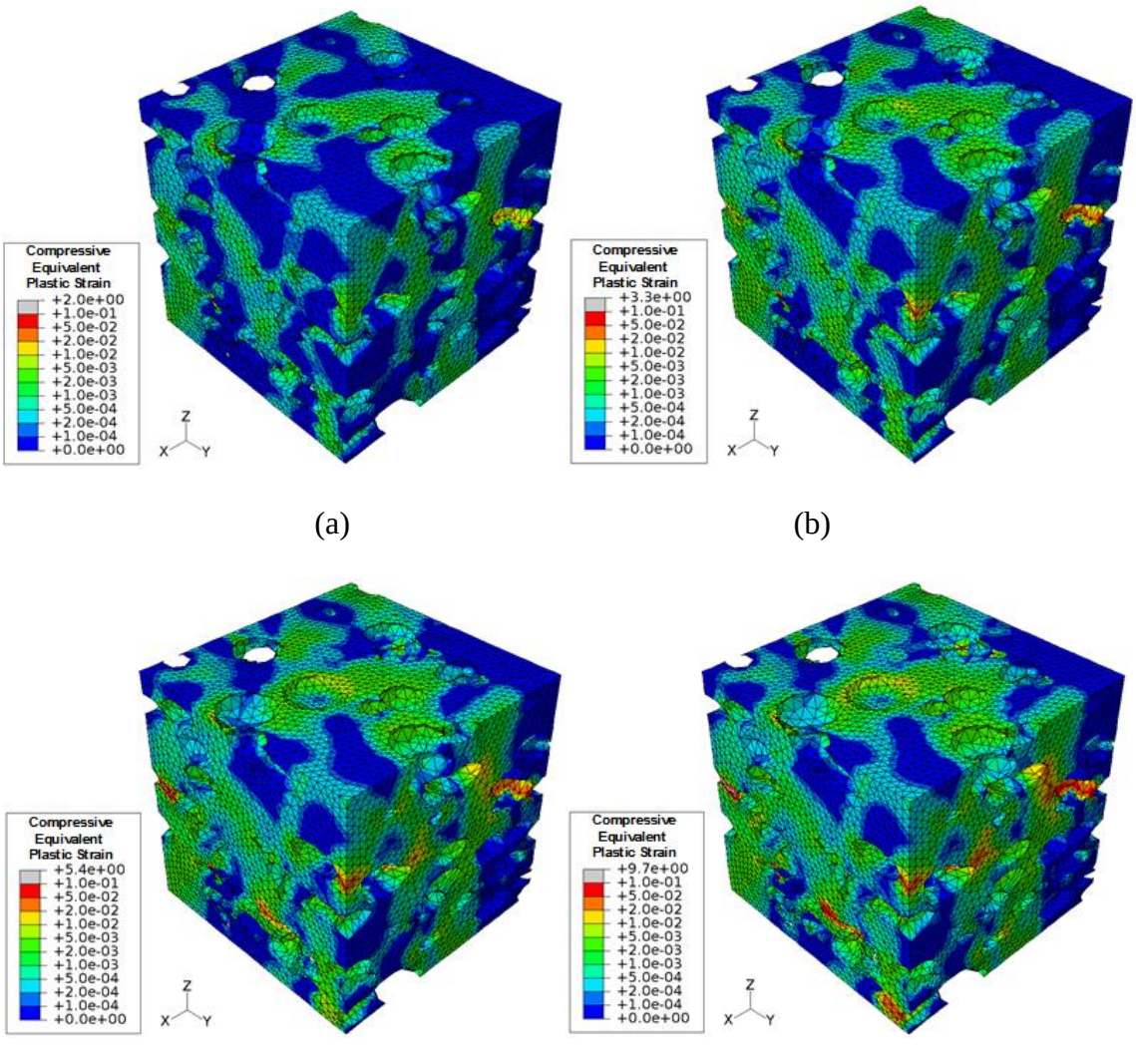

Figure 52: Compressive equivalent plastic strain for porous Ti_2AlC with 32.8 vol. % aligned 170-250μm ellipsoid-like pores ($f_0^+ = f_0^- = 225$MPa case) with compressive load in z-direction at different strain level: (a) $\varepsilon = 3.0$E-2, (b) $\varepsilon = 5.0$E-2, (c) $\varepsilon = 7.0$E-2, (d) $\varepsilon = 1.0$E-1.

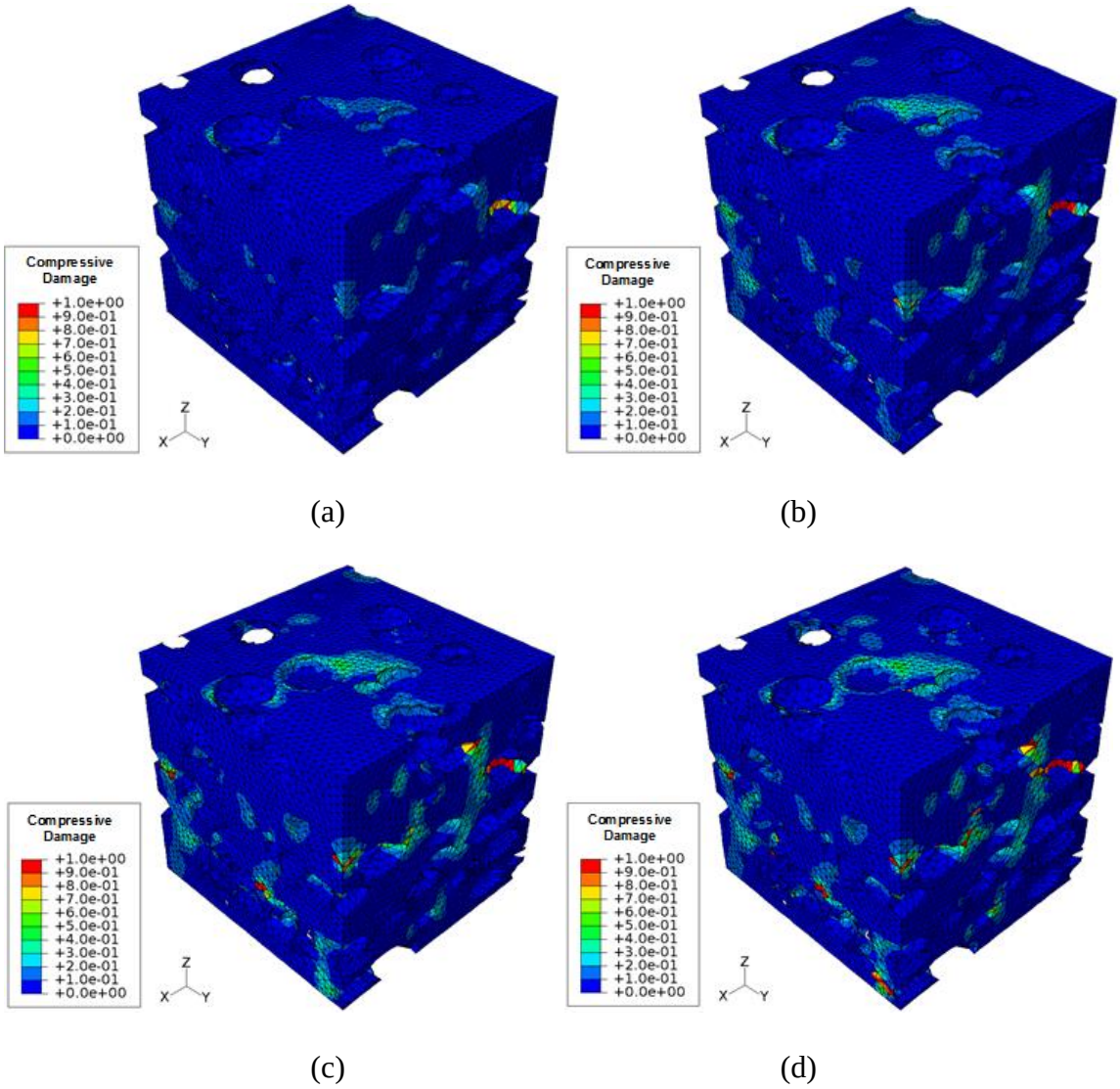

Figure 53: Compressive damage density for porous Ti_2AlC with 32.8 vol. % aligned 170-250μm ellipsoid-like pores ($f_0^+ = f_0^- = 225$MPa case) with compressive load in z-direction at different strain level: (a) $\varepsilon = 3.0$E-2, (b) $\varepsilon = 5.0$E-2, (c) $\varepsilon = 7.0$E-2, (d) $\varepsilon = 1.0$E-1.

5.3.2.3 The effect of varying loading direction

As mentioned before, the material system of porous Ti_2AlC with aligned ellipsoid-like pores is transversely isotropic. In this section, effect of loading direction on compressive behavior of this transversely isotropic porous system is investigated. As an example, plastic-damage finite element analysis is carried out on 3D RVE created for porous Ti_2AlC with 32.8 vol. % aligned 170-250μm ellipsoid-like pores. The five independent Young's moduli for the corresponding 3D RVE obtained previously are listed in Table 12. The stress-strain curves for the cases with same material properties ($f_0^+ = f_0^- = 225\text{MPa}$) and three compressive load directions, i.e., transverse direction (x-, and y-direction) and longitudinal direction (z-direction), are shown in Figure 54. It has been shown in the previous section that the initial stiffness of porous Ti_2AlC is approximately equal to the Young's moduli in the load direction. Here again, the initial stiffness of porous Ti_2AlC in different load directions are approximately equal to the Young's modulus in the corresponding load direction, e.g. the initial stiffness in longitudinal direction is equal to E_L= 87.69GPa and the initial stiffness in transverse directions is around E_T= 141.14GPa. Also, the stress-strain curves for compressive load in two transverse directions, i.e. x-, and y-direction are very similar, with corresponding compressive strength in y-direction 3% higher than the compressive strength in x-direction. This again approves the transverse isotropy of the created 3D RVE. Moreover, because of the transverse isotropy of the porous Ti_2AlC with aligned ellipsoid-like pores, the material system can sustain more loads in transverse directions (x-, and y-direction) than in longitudinal direction (z-direction). It is shown in Figure 54 that the average

compressive strength obtained from the given 3D RVE of porous Ti_2AlC in transverse directions (x-, and y-direction) is around 241.46MPa. It is about 58% larger than the compressive strength in longitudinal direction (z-direction) which is approximately 152.76MPa.

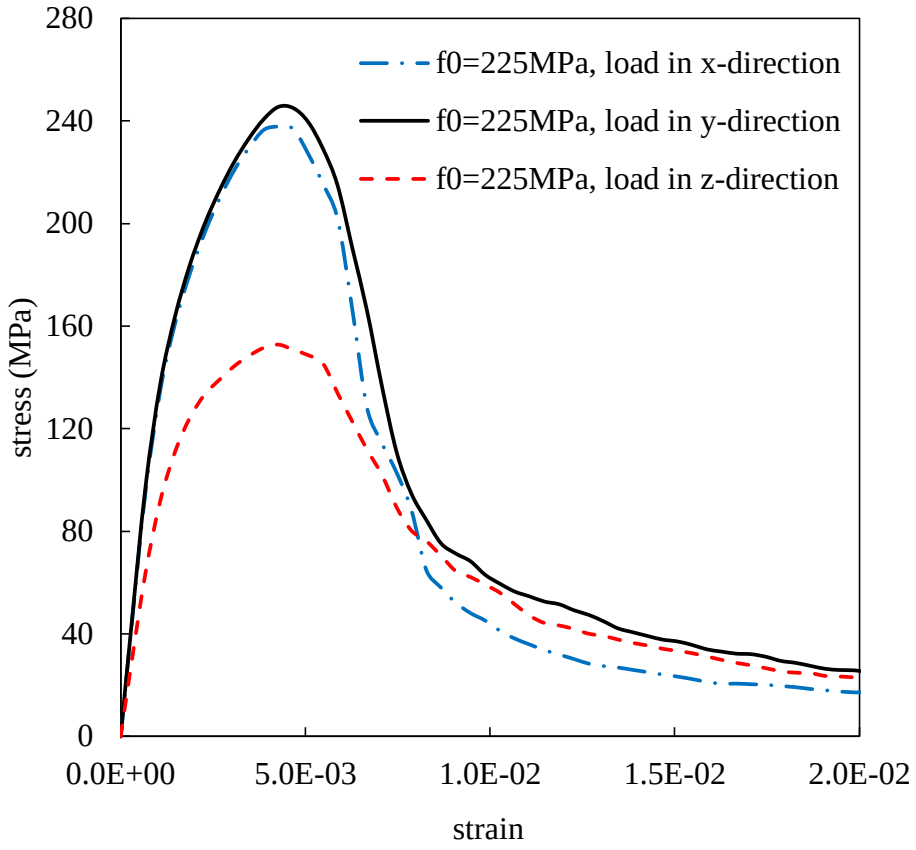

Figure 54: Stress-strain relation obtained from 3D RVE of porous Ti_2AlC with 32.8 vol. % aligned 170-250μm ellipsoid-like pores for the cases: initial yield stress $f_0^+ = f_0^- =$ 225MPa with load in x, y- and z-direction.

5.3.2.4 The effect of pore volume fraction and pore size

It has been shown in Table 12 that the elastic moduli of porous Ti_2AlC decreases as porosity increases, and it is obvious that porosity will also play an important role for inelastic compressive behavior of the porous system. Therefore, the effect of porosity volume fraction and pore size on plastic-damage behavior of porous Ti_2AlC is examined in this section. As an example, the 3D RVEs of porous Ti_2AlC with 32.8 and 40.5 vol. % aligned 170-250μm ellipsoid-like pores, as shown in Figure 43 (a) and (b) are used for comparison. Figure 55 (a) and (b) show the FE predicted stress-strain curves obtained from the corresponding 3D RVEs for the case with initial yield stress $f_0^+ = f_0^- =$ 225MPa and load in longitudinal as well as transverse direction (z, and y-direction), respectively. It is shown that with porosity decreasing from 40.5% to 32.8%, the compressive strength in longitudinal direction σ_L of porous Ti_2AlC increases approximately 51%, i.e. from 101.12MPa to 152.76MPa, while the compressive strength in transverse direction σ_T increase around 24%, i.e. from 198.43MPa to 245.47MPa.

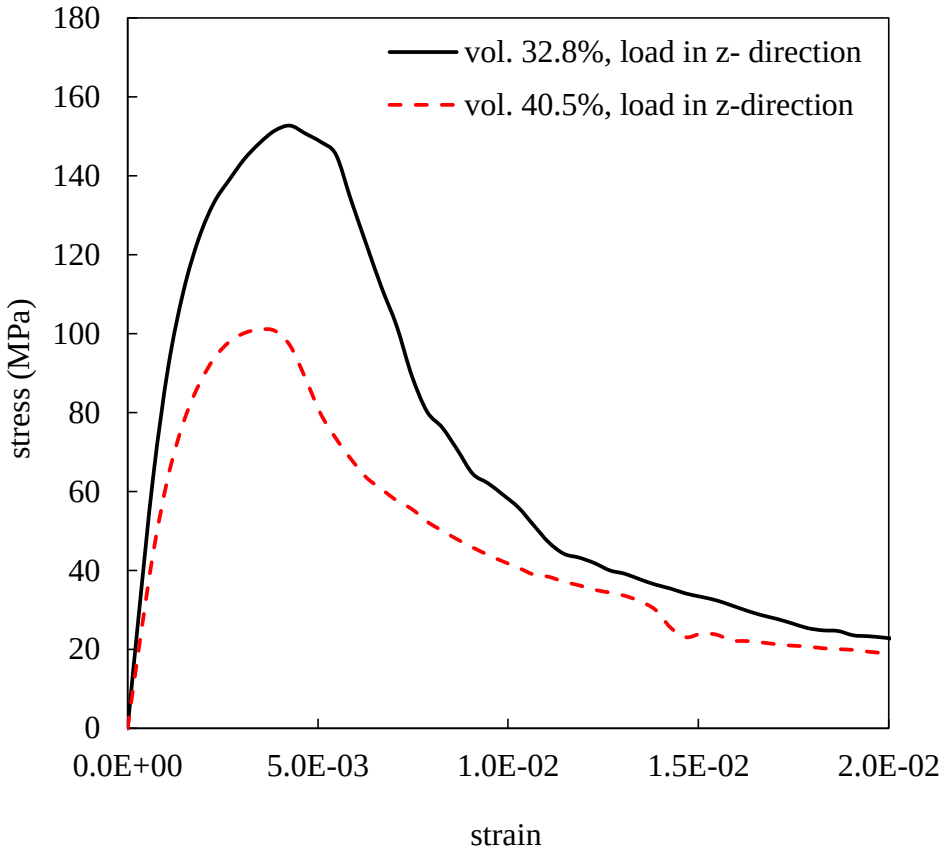

(a)

Figure 55: Stress-strain relation obtained from 3D RVE of porous Ti_2AlC with 32.8 and 40.5 vol. % aligned 170-250μm ellipsoid-like pores for the case: initial yield stress $f_0^+ = f_0^- = 225\text{MPa}$ with compressive load: (a) in longitudinal direction (z-direction), (b) in transverse direction (y-direction).

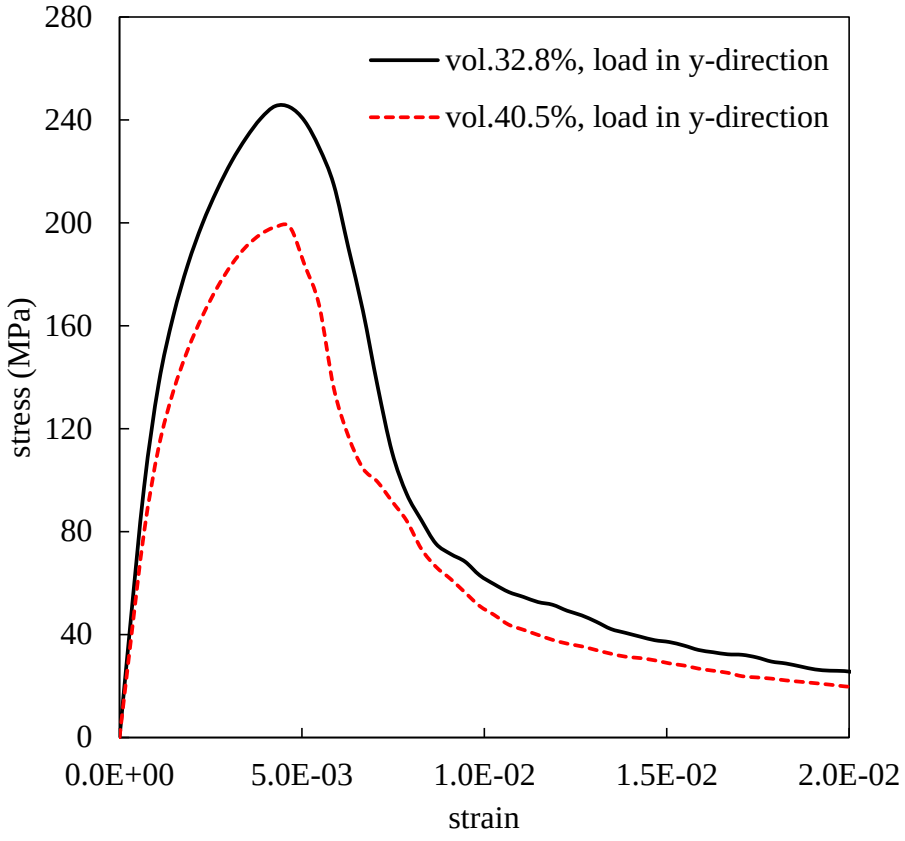

(b)

Figure 55: Continued.

For different pore sizes, as shown in Table 9, although the porosity volume fractions of two created 3D RVEs are nearly the same, i.e., 170-250μm pore size group with 32.8% in volume fraction and 340-500μm pore size group with 33.5% in volume fraction, the numbers of pores within the corresponding 3D RVEs are far more different. That is, for 170-250μm pore size group, there are 229 pores within the 3D RVE. With the same 3D RVE size, 340-500μm pore size group only have 43 pores within the

corresponding 3D RVE. The huge discrepancy in pore number affects the microstructure of the porous Ti_2AlC, such as effective cross-section area and pore interconnectivity, etc. Therefore, the effect of pore size on the plastic-damage behavior of porous T_2AlC is also investigated. The stress-strain curves obtained from finite element analysis for two porous Ti_2AlC with approximately 33% volume fraction of pores in size 170-250μm and 340-500μm, under compressive load in longitudinal and transverse direction (z-, and y-direction) are shown in Figure 56 (a) and (b), respectively.

As shown in Figure 56 (a), the compressive strength in longitudinal direction σ_L of porous Ti_2AlC with pore size 340-500μm is smaller than that of porous Ti_2AlC with pore size 170-250μm. In details, the FE predicted σ_L of porous Ti_2AlC with pore size 340-500μm is 127.42MPa for $f_0^+ = f_0^- = 225\text{MPa}$, which is about 16.6% smaller than those of porous Ti_2AlC with pore size 170-250μm. However, the compressive strengths in transverse direction σ_T for the two pore size group are nearly the same, around 245MPa, as seen in Figure 56 (b). One possible explanation is that, the discrepancy of the effective solid area in transverse plane (x-y plane) for the two 3D RVEs is larger than that of effective solid area in longitudinal planes (x-z plane and y-z plane). Another observation is that the stress-strain curves of porous Ti_2AlC with pore size 340-500μm is not as smooth as those of porous Ti_2AlC with pore size 170-250μm. This might due to the way damage accumulates in the microstructure of porous Ti_2AlC: Since the porous Ti_2AlC with pore size 340-500μm has much less pore number than the latter, its pore interconnectivity is higher than that of pore size 170-250μm. Once local damages

accumulate and coalesce, small cracks start to form and they are likely to become major cracks due to the high pore interconnectivity and therefore will greatly affect the microstructure and further lead to local material failure and hardening (zigzag shape of the stress-strain curve).

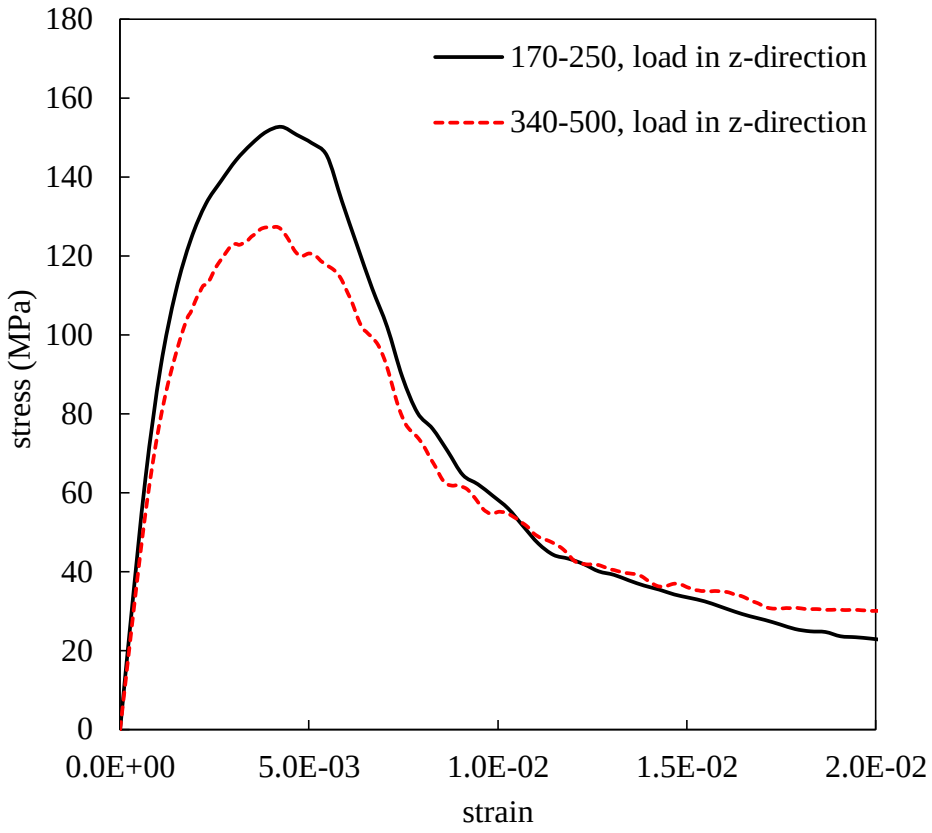

(a)

Figure 56: Stress-strain relations obtained from 3D RVE of porous Ti_2AlC with $f_0^+ = f_0^- = 225$, 275MPa and approximately 33 vol. % of pores in size 170-250μm and 340-500μm, under compressive load: (a) in longitudinal direction (z-direction), (b) in transverse direction (y-direction).

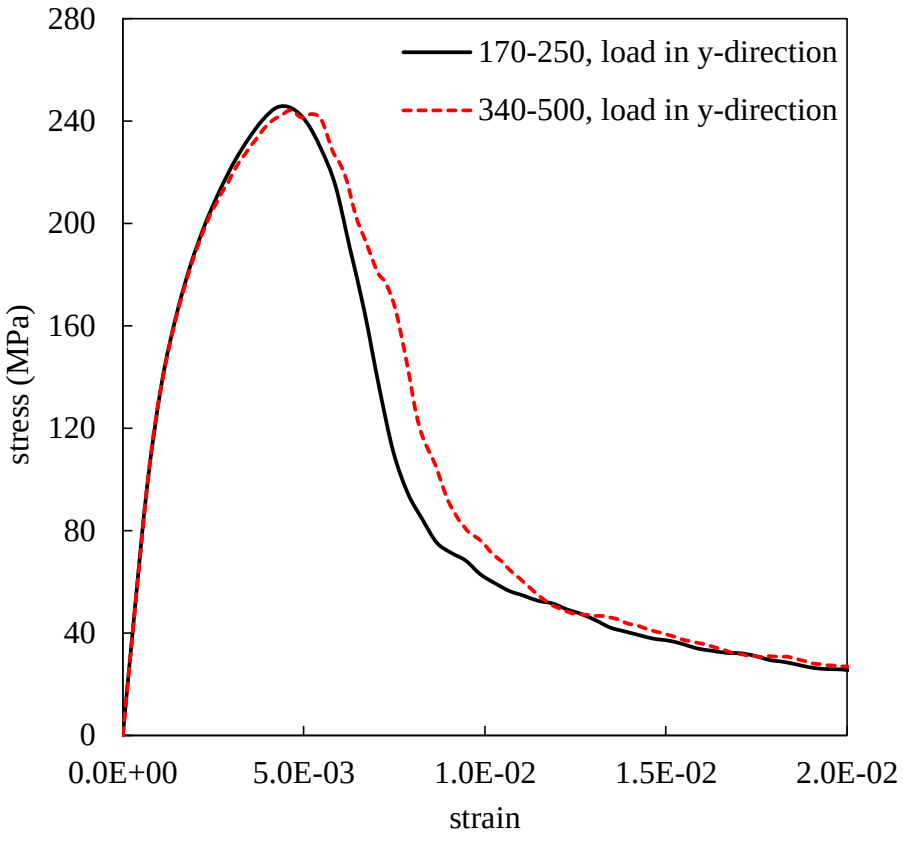

(b)

Figure 56: Continued

Finally, in summary, the trend of all stress-strain curves shown in the above four subsections is similar, that is all of them have a reverted narrow "V" shape, i.e. quasi-brittle behavior. And the compressive strengths of porous Ti_2AlC in longitudinal and

transverse direction obtained from all three 3D RVEs for $f_0^+ = f_0^- = 225\text{MPa}$ case are summarized in Table 15 and compared with the experimental data available in [103]. It is found that the FE predicted compressive strengths in longitudinal direction σ_L agree with the measured results well, and the FE predicted compressive strengths σ_T are about 20% higher the experimental results.

Table 15: Effective compressive strength of porous T_2AlC with aligned ellipsoid-like pores ($f_0^+ = f_0^- = 225\text{MPa}$).

Pore size(μm)	Porosity (vol. %)	FE predicted σ_L (MPa)	FE predicted σ_T (MPa)	Measured σ_L (MPa)	Measured σ_T (MPa)
170-250	32.8	152.76	241.62	168±27	N/A
170-250	40.5	101.12	191.88	N/A	149±10
340-500	33.5	127.42	238.05	130±10	188±12

CHAPTER VI

SUMMARY AND CONCLUSIONS

Summary of the research work in this dissertation and the conclusions can be drawn from the computational study are:

(1) In Chapter II, micromechanics based homogenization methods are used to estimate the effective elastic moduli of Ti_2AlC/Al composites with various compositions. These properties are implemented in UMAT and used in finite element analysis of graded Ti_2AlC/Al rectangular plate under uniformly distributed load on pure Ti_2AlC surface. The effects of defects to mechanical response of graded Ti_2AlC/Al rectangular plate are investigated. Due to the degradation of elastic moduli, the in-plane deflection along mid-plane and transverse shear stress through thickness altered considerably by increased void volume fraction.

(2) In Chapter III, detailed FE models of 3D RVEs created based on the microstructure of the IPCs and micromechanics-based theoretical models are used to study the mechanical and thermal expansion properties of stainless-steel/bronze IPCs. For effective elastic moduli, uniaxial tension and simple shear test are simulated using FE models of 3D RVEs to obtain effective Young's moduli, Poisson's ratio and shear moduli of 60% and 80% IPCs. The FE predicted effective Young's moduli agree well with the micromechanics based homogenization methods. Also, it is found that the predicted effective elastic moduli are loading direction independent, and the 3D RVEs

created can be seen as statistically homogeneous and isotropic. Therefore, they can represent the local continuum properties of the IPCs.

The FE predicted CTEs in general agree with the elastic Kerner-Schapery bounds well. This can be understand by the fact that the FE analyses with uniaxial tensile load, in which thermal residual stress is taken as initial stress conditions, actually unloaded the IPCs from partially yielded condition to a relatively elastic state.

The FE results show that the thermal residual stress and voids nucleation both have influence on the flow properties of the IPCs. The existence of thermal residual stress leads to plastic deformation, especially in bronze, which further results in reduction of apparent moduli of the IPCs subjected to uniaxial tension. On the other hand, voids located with bronze and along interfaces of the two phases play a very important role in damage evolution of the IPCs, especially for 80% IPC. Nucleation of the new voids, which occurs at the second-phase particles by decohesion of the particle-matrix interface, has the main contribution to the overall increase in the volume fraction of the voids. In this paper, due to the limited experimental supporting data regarding the failure the IPCs, the damage behavior study is only focused on damage evolution and its influence on the flow properties of the IPCs.

From the investigations of mechanical, thermal expansion, elastoplastic-damage properties of the IPCs, it is clear that the FE models developed in this study have very good correlation with the experimental results and provide useful insights on how thermal residual stresses and voids nucleation affect the mechanical properties of the IPCs. Therefore, it can be a very useful tool to study the behavior of IPCs, whose

properties cannot be obtained directly from the conventional micromechanics dispersed inclusions type solutions.

(3) In Chapter IV, finite element modeling on 3D RVEs is carried out to predict the thermal conductivity of the NiTi/Ti_3SiC_2 composite, and the simulation results are compared to the measured results. The major findings are:

The interfacial layer with low effective thermal conductivity lowers the overall heat flux flowing through the composite, especially the NiTi phase, due to the interfacial thermal resistance at those newly formed complex phase boundaries within interfacial layer during fabrication process. The new phase boundaries result in thermal interfacial resistance at constituent interfaces. The computational framework developed in this study offers a tool to provide insight into the effective thermal properties of the interfacial layer, which are difficult to determine experimentally.

(4) In Chapter V, detailed FE models of 3D RVEs created based on the microstructure of the porous Ti_2AlC with sphere-like and aligned ellipsoid-like pores. Micromechanics based homogenization methods are used to obtain the elastic properties of porous Ti_2AlC and compared with FE predictions. A coupled plasticity-damage constitutive model is used to consider distinct tensile and compressive behaviors of Ti_2AlC.

Uniaxial tension and simple shear test are simulated using FE models of 3D RVEs to obtain effective elastic moduli for porous Ti_2AlC with sphere-like pores as well as ellipsoid-like pores. For porous Ti_2AlC with sphere-like pores, i.e. isotropic case, the effective elastic moduli obtained from micromechanics methods and FE analysis are

compared with experimental results. One observation from the experimental data point is that there is jump in Young's modulus and shear modulus when the porosity volume fraction is around 13.6%. One possible explanation for this phenomenon is percolation or high pore interconnectivity which is caused by the small channel shape pores left at the grain edges after sintering. Also, it is found that the estimation of Young's modulus and shear modulus obtained from Mori-Tanaka method and unit cell method can cover most of the experimental data points. This can be understand by the fact that the Mori-Tanaka method represent the microstructure with non-overlapping inclusions and the unit cell method represent the microstructure with fully connected reinforcement phase, and therefore these two methods can cover the cases with relatively low and high pore interconnectivity. This also helps to explain why the FE prediction is more close to the Mori-Tanaka method when porosity volume fraction is low and gradually approaching the unit cell method as the porosity volume fraction increases. Since, channel shape pores are not considered in the 3D RVEs created in this study, it is hard to achieve high pore interconnectivity when the porosity volume fraction is low even though the overlapping of sphere-like pores is took into account. This condition can be improved when the porosity volume fraction if relatively high and the 3D RVEs can give reasonable FE predictions for elastic moduli in general. For porous Ti_2AlC with ellipsoid-like pores, i.e. transversely isotropic case, five independent elastic moduli for porous Ti_2AlC with two pore size group are obtained from FE analysis. It is found that the pore size does not have much influence on effective moduli.

For plastic-damage behavior of porous Ti_2AlC with aligned ellipsoid-like pores, it shows that principle tensile stress plays a very important role in local damage of porous Ti_2AlC due to the relatively low tensile strength and brittle-like behavior of dense Ti_2AlC under tensile load. Overall the porous Ti_2AlC fail in a quasi-brittle manner under uniaxial compressive load. That is the stress-strain curve has the inverted narrow "V" shape. It is also found that the transversely isotropic material system has higher compressive strength in transverse direction that in longitudinal direction.

From the investigations of elastic and plastic-damage behavior of porous Ti_2AlC material system, it shows that the FE models developed in this study have very good correlation with the experimental results and provide useful insight on how tensile material properties of dense Ti_2AlC, loading direction, pore volume fraction and pore size affect the plastic-damage behavior of the porous Ti_2AlC under compressive loading.

REFERENCES

[1] Barsoum MW. Prog. Solid State Chem. 2000;28:201.

[2] Sun ZM. Int. Mater. Rev. 2011;56:143.

[3] Byeon JW, Liu J, Hopkins M, Fischer W, Garimella N, Park KB, Brady MP, Radovic M, El-Raghy T, Sohn YH. Oxid. Met. 2007;68:97.

[4] Radovic M, Barsoum MW, Ganguly A, Zhen T, Finkel P, Kalidindi SR, Lara-Curzio E. Acta Materialia 2006;54:2757.

[5] Barsoum MW, Zhen T, Kalidindi SR, Radovic M, Murugaiah A. Nature Materials 2003;2:107.

[6] Aboudi J, Pindera MJ, Arnold SM. Composites Part B: Engineering 1999;30:777.

[7] Kouzeli M, Dunand DC. Acta Materialia 2003;51:6105.

[8] Peng HX, Fan Z, Evans JRG. Materials Science and Engineering A 2001;303:37.

[9] Wegner LD, Gibson LJ. International Journal of Mechanical Sciences 2000;42:925.

[10] Newkirk MS, Urquhart AW, Zwicker HR, Breval E. Journal of Materials Research 1986;1:81.

[11] Claussen N, Urquhart AW. Encyclopedia of Materials Science and Engineering, Supplementary 1990;2:1111.

[12] Toy C, Scott WD. Journal of the American Ceramic Society 1990;73:97.

[13] Aghajanian MK, Burke JT, White DR, Nagelberg AS. S.A.M.P.E. quarterly 1989;20:43.

[14] Pyzik AJ, Aksay IA. Processing of Ceramic and Metal Matrix Composites 1989:269.

[15] Schoen S, Prielipp H, Janssen R, Roedel J, Claussen N. Journal of the American Ceramic Society 1994;77:701.

[16] Prielipp H, Knechtel M, Claussen N, Streiffer SK, Müllejans H, Rühle M, Rödel J. Materials Science and Engineering A 1995;197:19.

[17] Knechtel M, Prielipp H, Müllejans H, Claussen N, Rödel J. Scripta Metallurgica et Materiala 1994;31:1085.

[18] Fitzgerald TJ, Michaud VJ, Mortensen A. Journal of Materials Science 1995;30:1037.

[19] Feng HJ, Moore JJ. Metallurgical and Materials Transactions B 1995;26:265.

[20] Sachs E, Guo H, Wylonis E, Serdy J, Brancazio D, Rynerson M, Cima M, Allen S. Rapid Prototyping 1996;2:1.

[21] Wegner LD, Gibson LJ. International Journal of Mechanical Sciences 2000;42:943.

[22] Cheng F, Hu L, Reddy JN, Karaman I, Hoffman E, Radovic2 M. Submitted to Acta Materialia 2013.

[23] Amini S, Ni C, Barsoum MW. Composites Science and Technology 2009;69:414.

[24] Yin HM, Paulino GH, Buttlar WG, Sun LZ. Journal of the Mechanics and Physics of Solids 2007;55:132.

[25] Hashin Z, Shtrikman S. Journal of the Mechanics and Physics of Solids 1963;11:127.

[26] Torquato S, Yeong CLY, Rintoul MD, Milius DL, Aksay IA. Journal of the American Ceramic Society 1999;82:1263.

[27] Munro RG. Journal of the American Ceramic Society 2001;84:1190.

[28] Tilbrook MT, Moon RJ, Hoffman M. Materials Science and Engineering A 2005;393:170.

[29] Fan Z, Tsakiropoulos P, Miodownik AP. Materials Science and Technology 1992;8:922.

[30] Suresh S, Mortensen A. Int. Mater. Rev. 1997;42:85.

[31] Ravichandran KS. Journal of the American Ceramic Society 1994;77:1178.

[32] Paul B. Trans. Metall. Soc. AIME 1960;218:36.

[33] Tuchinskii LI. Soviet Powder Metallurgy and Metal Ceramics 1983;22:588.

[34] Kerner EH. Proceedings of the Physical Society. Section B 1956;69:808.

[35] Schapery RA. J. Compos. Mater. 1968;2:380.

[36] Rosen BW, Hashin Z. International Journal of Engineering Science 1970;8:157.

[37] Bruck HA, Rabin BH. Journal of the American Ceramic Society 1999;82:2927.

[38] Aboudi J, Pindera MJ, Arnold SM. International Journal of Solids and Structures 1996;33:931.

[39] Pindera MJ, Aboudi J, Arnold SM. Engineering Fracture Mechanics 2002;69:1587.

[40] Reiter T, Dvorak GJ, Tvergaard V. Journal of the Mechanics and Physics of Solids 1997;45:1281.

[41] Reddy JN, Cheng ZQ. European Journal of Mechanics, A/Solids 2001;20:841.

[42] Vel SS, Batra RC. International Journal of Solids and Structures 2003;40:7181.

[43] Gasik MM. Computational Materials Science 1998;13:42.

[44] Ueda S, Gasik M. Journal of Thermal Stresses 2000;23:395.

[45] Ueda S. JSME International Journal, Series A: Solid Mechanics and Material Engineering 2002;45:138.

[46] Yin HM, Sun LZ, Paulino GH. Acta Materialia 2004;52:3535.

[47] Hale DK. Journal of Materials Science 1976;11:2105.

[48] Benveniste Y, Miloh T. International Journal of Engineering Science 1986;24:1537.

[49] Böhm HJ, Nogales S. Composites Science and Technology 2008;68:1181.

[50] Dunn ML, Taya M. Journal of Applied Physics 1993;73:1711.

[51] Poniznik Z, Salit V, Basista M, Gross D. Computational Materials Science 2008;44:813.

[52] Zahl DB, Schmauder S, McMeeking RM. Zeitschrift fuer Metallkunde/Materials Research and Advanced Techniques 1993;84:802.

[53] Ravichandran KS. Acta Metallurgica Et Materialia 1994;42:1113.

[54] Ravichandran KS. Composites Science and Technology 1994;52:541.

[55] Feng XQ, Mai YW, Qin QH. Computational Materials Science 2003;28:486.

[56] Schmauder S, Weber, U., Hofinger, I., Neubrand, A. Technische Mechanik 1999;19:313.

[57] Torquato S. International Journal of Solids and Structures 2000;37:411.

[58] Mishnaevsky Jr LL. Materials Science and Engineering A 2005;407:11.

[59] Feng XQ, Tian Z, Liu YH, Yu SW. Applied Composite Materials 2004;11:33.

[60] Gurson AL. Journal of Engineering Materials and Technology, Transactions of the ASME 1977;99 Ser H:2.

[61] Tvergaard V. International Journal of Fracture 1981;17:389.

[62] Needleman A, Tvergaard V. Journal of the Mechanics and Physics of Solids 1984;32:461.

[63] Nahshon K, Hutchinson JW. European Journal of Mechanics, A/Solids 2008;27:1.

[64] Benzerga AA, Besson J, Pineau A. Acta Materialia 2004;52:4639.

[65] Fabrègue D, Pardoen T. Journal of the Mechanics and Physics of Solids 2008;56:719.

[66] Leblond JB, Mottet G. Comptes Rendus - Mecanique 2008;336:176.

[67] Pardoen T, Hutchinson JW. Journal of the Mechanics and Physics of Solids 2000;48:2467.

[68] Zhang ZL, Niemi E. International Journal of Fracture 1995;70:321.

[69] Scheyvaerts F, Pardoen T, Onck PR. International Journal of Damage Mechanics 2010;19:95.

[70] Besson J, Guillemer-Neel C. Mechanics of Materials 2003;35:1.

[71] Mear ME, Hutchinson JW. Mechanics of Materials 1985;4:395.

[72] Leblond JB, Perrin G, Devaux J. Eur. J. Mech. A/Solids 1995;14:499.

[73] Besson J. International Journal of Plasticity 2009;25:2204.

[74] Klöcker H, Tvergaard V. International Journal of Mechanical Sciences 2003;45:1283.

[75] Lassance D, Fabrègue D, Delannay F, Pardoen T. Progress in Materials Science 2007;52:62.

[76] Paquet D, Ghosh S. Engineering Fracture Mechanics 2011;78:205.

[77] Gologanu M, Leblond JB, Devaux J. Journal of the Mechanics and Physics of Solids 1993;41:1723.

[78] Gologanu M, Leblond J-B, Devaux J. Journal of Engineering Materials and Technology, Transactions of the ASME 1994;116:290.

[79] Gologanu M, Leblond JB, Perrin G, Devaux J. Continuum Micromechanics 1997:61.

[80] Benzerga AA, Besson J. European Journal of Mechanics, A/Solids 2001;20:397.

[81] Keralavarma SM, Benzerga AA. Comptes Rendus - Mecanique 2008;336:685.

[82] Monchiet V, Gruescu C, Charkaluk E, Kondo D. Comptes Rendus - Mecanique 2006;334:431.

[83] Monchiet V, Cazacu O, Charkaluk E, Kondo D. International Journal of Plasticity 2008;24:1158.

[84] Scheyvaerts F, Onck PR, Tekoğlu C, Pardoen T. Journal of the Mechanics and Physics of Solids 2011;59:373.

[85] Wen J, Huang Y, Hwang KC, Liu C, Li M. International Journal of Plasticity 2005;21:381.

[86] Monchiet V, Bonnet G. International Journal of Solids and Structures 2013;50:320.

[87] Basirat M, Shrestha T, Potirniche GP, Charit I, Rink K. International Journal of Plasticity 2012;37:95.

[88] Gao X, Zhang T, Zhou J, Graham SM, Hayden M, Roe C. International Journal of Plasticity 2011;27:217.

[89] Lecarme L, Tekoğlu C, Pardoen T. International Journal of Plasticity 2011;27:1203.

[90] Li H, Fu MW, Lu J, Yang H. International Journal of Plasticity 2011;27:147.

[91] Tekoğlu C, Pardoen T. International Journal of Plasticity 2010;26:549.

[92] Ohata M, Suzuki M, Ui A, Minami F. Engineering Fracture Mechanics 2010;77:277.

[93] Morgeneyer TF, Besson J. Scripta Materialia 2011;65:1002.

[94] Wang Y, Liang S, Ren J. Materials Science and Engineering A 2012;534:542.

[95] Cayzac HA, Sa ïK, Laiarinandrasana L. International Journal of Plasticity 2013.

[96] Boisot G, Laiarinandrasana L, Besson J, Fond C, Hochstetter G. International Journal of Solids and Structures 2011;48:2642.

[97] Canal LP, Segurado J, Llorca J. International Journal of Solids and Structures 2009;46:2265.

[98] Geni M, Kikuchi M. Acta Materialia 1998;46:3125.

[99] Ishikawa N, Parks DM, Kurihara M. ISIJ International 2001;41:76.

[100] Fraczkiewicz M, Zhou AG, Barsoum MW. Acta Materialia 2006;54:5261.

[101] Zhou AG, Barsoum MW, Basu S, Kalidindi SR, El-Raghy T. Acta Materialia 2006;54:1631.

[102] Sun ZM, Murugaiah A, Zhen T, Zhou A, Barsoum MW. Acta Materialia 2005;53:4359.

[103] Hu L, Benitez R, Basu S, Karaman I, Radovic M. Acta Materialia 2012;60:6266.

[104] Barsoum MW, Radovic M. In: Clarke DR, Fratzl P, editors. Annual Review of Materials Research, Palo Alto: Annual Reviews 2011;41:195.

[105] Cicekli U, Voyiadjis GZ, Abu Al-Rub RK. International Journal of Plasticity 2007;23:1874.

[106] Gatuingt F, Pijaudier-Cabot G. International Journal for Numerical and Analytical Methods in Geomechanics 2002;26:1.

[107] Lee J, Fenves GL. Journal of Engineering Mechanics 1998;124:892.

[108] Wu JY, Li J, Faria R. International Journal of Solids and Structures 2006;43:583.

[109] Yazdani S, Schreyer HL. Journal of Engineering Mechanics 1990;116:1435.

[110] Bazant ZP, Kim S-S. ASCE J Eng Mech Div 1979;105:407.

[111] Brünig M, Ricci S. International Journal of Plasticity 2005;21:1346.

[112] Imran I, Pantazopoulou SJ. Journal of Engineering Mechanics 2001;127:281.

[113] Krätzig WB, Pölling R. Computers and Structures 2004;82:1201.

[114] Lubliner J, Oliver J, Oller S, Oñate E. International Journal of Solids and Structures 1989;25:299.

[115] Menzel A, Ekh M, Runesson K, Steinmann P. International Journal of Plasticity 2005;21:397.

[116] Abu Al-Rub RK, Kim SM. Engineering Fracture Mechanics 2010;77:1577.

[117] Mori T, Tanaka K. Acta Metallurgica 1973;21:571.

[118] Tvergaard V. International Journal of Solids and Structures 1982;18:659.

[119] Kim SM, Abu Al-Rub RK. Cement and Concrete Research 2011;41:339.

[120] Shen H, Brinson LC. J. Mechanics of Materials and Structures 2006;1:1179.

[121] Muliana AH. International Journal of Solids and Structures 2009;46:1911.

[122] Turner PS. J. Res. Natl. Bureau Stand. 1946;37.

[123] Corigliano A, Mariani S, Orsatti B. International Journal of Fracture 2000;104:349.

[124] Hu L, Kothalkar A, Karaman I, Proust G, Radovic M. In preparation 2013.

[125] Kapitza PL. Zh. Eksp. Teor. Fiz, J. Phys. USSR 1941;4:181.

[126] Kachanov LM. Izv. Akad. Nauk. SSR 1958;8:26.

[127] Zhu QZ, Kondo D, Shao JF. International Journal for Numerical and Analytical Methods in Geomechanics 2009;33:749.

[128] Krajcinovic D. Damage Mechanics 1996.

[129] Simo JC, Hughes TJR. Computational Inelasticity, Interdisciplinary Applied Mathematics 1998.

[130] Simo JC, Ju JW. International Journal of Solids and Structures 1987;23:821.

[131] Chow CL, Wang J. International Journal of Fracture 1987;33:3.

[132] Abu Al-Rub RK, Voyiadjis GZ. International Journal of Solids and Structures 2003;40:2611.

[133] Celzard A, McRae E, Deleuze C, Dufort M, Furdin G, Marêché JF. Physical Review B - Condensed Matter and Materials Physics 1996;53:6209.

[134] Wu J, McLachlan DS. Physical Review B - Condensed Matter and Materials Physics 1997;56:1236.

[135] Coble RL. Journal of Applied Physics 1961;32:787.